

REPORT DOCUMENTATION PAGE				<i>Form Approved</i> OMB No. 0704-0188	
<small>Public reporting burden for this collection of information is estimated to average 1 hour per response, including the time for reviewing instructions, searching existing data sources, gathering and maintaining the data needed, and completing and reviewing this collection of information. Send comments regarding this burden estimate or any other aspect of this collection of information, including suggestions for reducing this burden to Department of Defense, Washington Headquarters Services, Directorate for Information Operations and Reports (0704-0188), 1215 Jefferson Davis Highway, Suite 1204, Arlington, VA 22202-4302. Respondents should be aware that notwithstanding any other provision of law, no person shall be subject to any penalty for failing to comply with a collection of information if it does not display a currently valid OMB control number. PLEASE DO NOT RETURN YOUR FORM TO THE ABOVE ADDRESS.</small>					
1. REPORT DATE (DD-MM-YYYY)		2. REPORT TYPE		3. DATES COVERED (From - To)	
4. TITLE AND SUBTITLE				5a. CONTRACT NUMBER	
				5b. GRANT NUMBER	
				5c. PROGRAM ELEMENT NUMBER	
6. AUTHOR(S)				5d. PROJECT NUMBER	
				5e. TASK NUMBER	
				5f. WORK UNIT NUMBER	
7. PERFORMING ORGANIZATION NAME(S) AND ADDRESS(ES)				8. PERFORMING ORGANIZATION REPORT NUMBER	
9. SPONSORING / MONITORING AGENCY NAME(S) AND ADDRESS(ES)				10. SPONSOR/MONITOR'S ACRONYM(S)	
				11. SPONSOR/MONITOR'S REPORT NUMBER(S)	
12. DISTRIBUTION / AVAILABILITY STATEMENT					
13. SUPPLEMENTARY NOTES					
14. ABSTRACT					
15. SUBJECT TERMS					
16. SECURITY CLASSIFICATION OF:			17. LIMITATION OF ABSTRACT	18. NUMBER OF PAGES	19a. NAME OF RESPONSIBLE PERSON
a. REPORT	b. ABSTRACT	c. THIS PAGE			19b. TELEPHONE NUMBER (include area code)

Advanced Plasma Propulsion

Final Technical Report

for AFOSR contract FA9550-09-1-0127

November 2011

Prepared by

Professor Edgar Choueiri
Princeton University

Professor Mark A. Cappelli
Stanford University

Professor Manuel Martinez-Sanchez (PI)
MIT

with contributions from

Ashley Hallock (GS at Princeton University)
Stephen Gildea and Taylor Matlock (MIT)

Contract Manager at AFOSR: Dr. Mitat Birkan

General Introduction

This final technical report documents an extensive experimental and theoretical effort, sponsored by AFOSR under Dr. Mitat Birkan and coordinated between research groups at three universities (MIT, Princeton, Stanford) dealing with two main branches of plasma propulsion:

Branch I) Ion production and acceleration from non-annular, magnetically insulated thrusters.

Branch II) Electrodeless inductive plasma propulsion, specifically the Faraday Accelerator with RF-Assisted Discharge and Conical Theta Pinch (FARAD+CTP).

The object of the research in Branch I was the study of a number of interrelated plasma accelerator concepts having as a common theme the use of innovative magnetic configurations, and the fact that magnetic effects played a controlling role in each case.

The MIT and Stanford tasks, focused on the so-called Divergent Cusped Field Thruster (DCF, or DCFT). This is a concept belonging to the general family of Hall devices, but being clearly distinguished by the use of a cylindrical set of magnetic cusps for electron confinement, in replacement of the simple radial field of common Hall thrusters. This has, among others, the effect of avoiding the use of a central pole piece, which reduces exposed surface area and facilitates miniaturization as well as diagnostic access. In addition, the confining effect on the plasma (magnetic in the case of the electrons, electrostatic in that of the ions) is very strong here, and only very small portions of the insulating casing are at all accessible to the plasma, with possibly beneficial effect on life. The divergent geometry was adopted in an attempt to further reduce ion impingement near the exit plane, although evidence gathered during the subsequent investigations cast some doubt as to that strategy.

Prior to this work, the preliminary results of MIT on a first implementation of the DCF thruster (Refs [1,2]) were highly encouraging, with efficiencies in the 40% range obtained on a non-optimized thruster at the 150-400 W range. It was realized at the outset, however, that the dominant physical effects in these devices are different enough from those more familiar from Hall thrusters to merit detailed experimental and theoretic study that could pave the way to rational improvement and development of the concept. Stanford (Prof. Cappelli's group) and MIT (Prof. Martinez-Sanchez' group), with support from the AFRL group (Dr. W. Hargus), undertook to perform these studies in as coordinated a fashion as allowed by the scope and nature of the project. In the event, the coordination proved to be highly effective, with each group contributing in its area of particular expertise, and with the AFRL facilities playing an essential role in the investigation.

Branch II was the purview of the Electric Propulsion Group at Princeton University under the direction of Professor Edgar Choueiri. There the work focused on some of the critical basic phenomena that control the acceleration process in a new type of inductive plasma accelerator, called the conical theta pinch FARAD (C θ P-FARAD), namely the inductive

formation of current sheets in that device and the effects of inductive coil geometry on thruster performance, specifically current sheet velocity. The goal was to obtain prescriptions that allow optimizing the inductive coil geometry for maximum performance.

The Stanford portion of the project consisted of four Tasks:

- ST1: Research Objective and Thruster Definitions
- ST2: Laser-Induced Fluorescence Mapping of Ion Transport
- ST3: Electrostatic Probe Characterization of Wave Dispersion and Turbulence
- ST4: Measurements of Plasma Potential and Plasma Temperature

The MIT portion of the original two-year project comprised four Tasks:

- MT1: Design and fabrication of DCF test thrusters
- MT2: Erosion studies
- MT3: Plume and magnetic detachment studies
- MT4: Fully kinetic thruster modeling

The Princeton portion of the project consisted of two Tasks:

- PT1: Fundamentals of inductive formation of current sheets
- PT2: Studies of the effects of inductive coil geometry on current sheet velocity

In the following section we present a task-by-task synopsis of the work and findings.

Synopsis

ST1: Research Objective and Thruster Definitions Over the course of this grant period, the Stanford team has studied and characterized the behavior of the three cusped-field thruster variants, namely the MIT Divergent Cusped Field Thruster (DCF-T), the Stanford (straight channel) Cusped Field Thruster (SCFT), and the Princeton Cylindrical Hall Thruster (CHT). All three of these variants were operated by Stanford researchers during this grant period. Stanford received possession of a copy of a DCF-T from MIT in the end of the first year of the grant, and is currently testing at Stanford, both the DCF-T and the SCF-T. Research on all three of these cusped thrusters was also carried out by Stanford researchers on assignment at the Air Force Research Laboratories at Edwards AFB. This included Laser-Induced Fluorescence (LIF) velocimetry mapping of the ion velocity field. (described in more detail later in the report).

ST2: Laser-Induced Fluorescence Mapping of Ion Transport

The Stanford component included mapping out ion transport (velocity, mean and distribution), inside the channel of the DCF, SCF and CHT thrusters described in Task S1. For this task, we employed laser-induced fluorescence (LIF), which is a diagnostic studied extensively within our laboratory. For the probing of the channel and near-field ion transport, we interrogated xenon ions (Xe II) through excitation of the $5d [4]^{7/2} - 6p [3]^{5/2}$ electronic transition at 834.7 nm. The hyperfine structure produced a total of 19 components, the constants of which are known for only the upper level of the transition, making the extraction of accurate velocity distributions tenuous. However, mean velocities were inferred with reasonable accuracy, and variations in the velocity distributions were elucidated. Ion velocity (within classes) is the result of the Doppler shift of the absorbing ions. These ions within the velocity class subsequently decay, through a transition originating from the same upper state ($6p [3]^{5/2}$) and terminating on the $6s [2]^{3/2}$ state, resulting in strong fluorescence at 541.9 nm. This non-resonant fluorescence allows for fairly good signal to background collection, and has led to extremely high fidelity mapping of the velocity fields (and velocity distributions), as described later in this report. These LIF studies are the primary results of the two-year study carried out by the Stanford team.

Measurements employed a tunable diode laser that is capable of scanning over the range of the probed transition. Phase-sensitive detection was used to discriminate against background plasma emission. A main feature and novelty of Stanford experiments was to study the ion velocity evolution *inside the channel*. This was carried out without making holes or slots through the discharge as was performed in previous annular Hall thruster experiments. Instead, we measured the fluorescence in partial backscatter configuration, with the probe laser entering the channel axially.

ST3: Electrostatic Probe Characterization of Wave Dispersion and Turbulence In addition to time-average ion transport properties obtained by LIF, we had also proposed studying the dynamical plasma behavior (fluctuations) within the channel and in the near-field of these thrusters. The goal was to use passively-biased Langmuir probes (triple probe for in-plane wave propagation determination) in ion collection mode impedance-matched and

amplified for high bandwidth sensitivity and gain. These measurements were motivated by the desire to understand the possible role (if any) played by low and high frequency instabilities on electron transport.

Because the SCFT does not appear to have significant plasma fluctuations in comparison to the DCF-T, and because we did not have access to a DCFT in the first year of the grant, these measurements were carried out on an existing laboratory Hall thruster. In this Hall thruster, we expected MHz-level azimuthally propagating waves associated with the two-stream ion-electron instabilities, which have been postulated to account for cross-field electron transport at modest levels, i.e., 1eV in potential fluctuations. A question arose as to the existence and possible significance of such fluctuations in the cusped-field thrusters, since the strong magnetic fields will also likely trap electrons and prevent electron migration towards the anode. During the second year of the grant, the student involved in these measurements graduated and was not replaced. While measurements were obtained on the Hall thruster, they were not yet implemented in the MIT DCF-T, and so this portion of the task is incomplete. However, for completion, we do summarize the results of these measurements on the Hall thruster later in this report.

ST4: Measurements of Plasma Potential and Plasma Temperature The potential distribution in the SCFT was extensively characterized using a floating emissive probe. The procedure for acquiring the potential measurements involves first mapping an unheated (floating) potential, with care taken to rapidly move the probe in and out of regions of strong heating so that it does not become self-emitting. Generally, this involves moving in and out along the axis, for varying radial positions. A 2D translation stage on which the thruster was mounted allowed for translational speeds of approximately 5 cm/s. After the floating potential measurements were completed, the probe was heated causing it to become self-emitting and the measurements were repeated to obtain the plasma potential, using usual theories, considering effects on ion collection associated with magnetic fields. The facility at Stanford is capable of time-resolving the probe signals, allowing the recreation of dominant temporal features in phase with low-frequency breathing oscillations, although this particular thruster did not exhibit strong oscillations. Time did not permit similar measurements on the DCF. The measurements obtained on the SCF-T are summarized later in this report.

ST5 Kinetic Simulations Understanding the electron dynamics in these cusped-field thrusters is a primary component of the Stanford research. The Stanford team carried out preliminary simulations using electron kinetic (particle) tracking with the prescribed magnetic and (measured) electric fields. This provided us with a window into the particle dynamics, including electron-scattering (from walls and heavy particles) and B-field mirroring, which we expected to see in regions very near the anode, and in the wall cusped regions, where the B-fields converged. For a prescribed static magnetic and electric field distribution (provided by experiments, e.g., see Task Stanford-4), high-fidelity time-integrating methods were utilized to track electrons launched from a simulated cathode. Electron collisions were not included in the simulations carried out so far, although the effect of secondary ionization on transport through the birth of electrons at locations other than the cathode was studied. Including momentum scattering and ionization collisions in the DCF/CHT configuration is the subject of continuing research.

MT1: Design and fabrication of DCF test thrusters. This task was fully completed. The original design of Ref. [1] was improved in several small ways, and four units were manufactured. Two of them remained at MIT, one was sent to Stanford and one was sent to the Air Force Research Lab (Edwards AFB). Plans for sending one thruster to the Princeton group were delayed, but the thruster is still available for any continuation of the research there.

MT2: Erosion studies. This task was fully completed. One of the DCF thrusters was tested at AFRL for 200 hours under high current operating mode, and detailed profilometry was carried out. Results indicate that erosion is limited to the cusp areas and the exit lip, where it is of the same order (but lower) as that observed in Hall thrusters. There were indications that the strong oscillations associated with the high-current mode played a role in the distribution and intensity of the erosion, but no long-term data could be collected in the low-current mode; this remains a priority for future research. Internal surface probing on an instrumented thruster was carried out in support of these studies; these tests confirmed the strong ion current concentration near the cusps, as well as the existence of potential depressions (“canyons”) in these same areas. A detailed and rigorous kinetic theory model was derived that confirms and explains most of these findings. Because of the implications of the current oscillations for erosion and life, these oscillations were studied via fast photography, coupled with current traces and some limited time-dependent probe data.

MT3: Plume and magnetic detachment studies. The previously available partial data on the structure of the DCF plume (Ref [2]) were extended and upgraded, including ion energy spectra as functions of angle. Emissive probe potential explorations were also conducted in the near-plume. These confirmed Stanford’s results for the modified cylindrical DCF, particularly in showing a highly localized acceleration layer located near the exit plane, and shaped roughly to mimic the outer portion of the last magnetic separatrix surface. These general features were confirmed and partially explained by PIC simulations (see Task 4), and were instrumental in crystallizing a conceptual framework that explains most of the geometrical organization of the plasma inside the thruster and into the plume. In this framework, the separatrix is seen as the natural locus of strong ionization, due to the repeated visits by cathode electrons; since ionization and acceleration are intrinsically coupled processes, strong potential gradients are formed perpendicular to the separatrix, and so the shape of this surface mainly determines the direction of the ion stream and hence the plume divergence and its hollow structure. With guidance from these principles, we carried out some magnetic re-designs in which external magnets were used to flatten or further bow out the separatrix; the results confirmed expectations, and the flattened configuration did result in a noticeable plume divergence reduction. The separatrix framework is by itself insufficient to explain the existence and features of the oscillatory high-current mode. Combining insights from it and from the experimental erosion and oscillation data, we have also formulated an unsteady framework that goes at least part of the way towards rationalizing all observations, but this work is still in need of further numerical and observational support. Plume detachment studies that were anticipated under this Task were deferred, in part due to the pressure of the many other unknowns to be explored, and in part due to the rapid theoretical advances made by Prof. Ahedo and his team in Madrid, in loose association with our studies (Refs [3,4]).

MT4: Fully kinetic thruster modeling. Our full PIC model, developed previously for Hall thrusters, has been modified for the geometry and features of the DCF, and has been used to support our experimental data as well as our conceptual exploration of the complex physics involved in these devices. In the process, many difficulties have been faced, and some remain to be fully resolved. The problems relate mostly to the extreme concentration of effects dictated by the cusped magnetic configuration, which makes it very challenging to obtain a complete resolution of the local potential profiles, and in turn, ion trajectories. The difficulty is heightened by the fact that, as uncovered in our theoretical research, ion confinement near the cusps is electrostatic rather than magnetic, and is in fact nearly independent of the relative size of ion gyro radius vs. region size. However, enough progress has been made to make clear the outlines of the various profiles, including the strong role of the last separatrix, the formation of the hollow plume structure, and the appearance of ion-confining potential canyons in front of the cusps. More recently, and not yet fully confirmed, we have obtained exciting numerical information on the dynamic of one of the repeated current pulses occurring in the high-current mode.

PT1: Fundamentals of inductive formation of current sheets The inductive formation of current sheets in a conical theta pinch FARAD thruster (C θ P-FARAD) was investigated experimentally with time-integrated photography. The goal is to help in understanding the mechanisms and conditions controlling the strength and extent of the current sheet in a conical pinch configuration, which are two indices important for C θ P-FARAD as a propulsion concept. The profiles of these two indices along the inside walls of the conical acceleration coil are assumed to be related to the profiles of the strength and extent of the luminosity pattern derived from photographs of the discharge. The variations of these profiles as a function of uniform back-fill neutral pressure (with no background magnetic field and all parameters held constant) provided the first clues on the nature and qualitative dependencies of current sheet formation. It was found that there is an optimal pressure for which both indices reach a maximum and that the rate of change in these indices with pressure differs on either side of this optimal pressure. This allowed the inference that current sheet formation follows a Townsend-like breakdown mechanism modified by the existence of a finite pressure-dependent radio-frequency-generated electron density background. The observation that the effective location of the luminosity pattern favors the exit-half of the conical coil is explained as the result of the tendency of the inductive discharge circuit to operate near its minimal self-inductance. Movement of the peak in the luminosity pattern towards the upstream side of the cone with increasing pressure was explained to result from the need of the circuit to compensate for the increase in background plasma resistivity due to increasing pressure.

PT2: Studies of the effects of inductive coil geometry on current sheet velocity

In this Task we explored the effects of inductive coil geometry on current sheet velocity in a conical theta pinch acceleration stage through experiments and calculations in order to obtain insight into optimizing the coil geometry for C θ P-FARAD. The experiment consisted of carrying out static measurements of the mutual inductance between a set of conical inductive coils of varying lengths and half-cone angles and their associated current sheet analogs made out of metallic foil. The measured dependences of mutual inductance on the

axial distance between the coil and the sheet were used as input to an analytical circuit model of inductive current sheet acceleration. This allowed the inference of some of the effects of coil geometry on the performance of the accelerator (the final sheet velocity). It was found that shorter driving coils, and to a lesser extent larger half-cone angles (whose effects are less pronounced for longer coils), are more favorable for vigorous current sheet acceleration. The trends were explained by considering that the uniformity of the magnetic field within the volume of a coil increases for longer, more solenoidal coils, and therefore would present a reduced magnetic field gradient to a current sheet translating away from the coil, thus reducing the rate of the change of inductance with distance and consequently decreasing the final sheet velocity.

Detailed Report on Tasks ST1 to ST4

Task Stanford-1. Research Objective and Thruster Definitions (Completed)

Over the course of this grant period, the Stanford team has studied and characterized the behavior of the three cusped-field thruster variants, namely the MIT Divergent Cusped Field Thruster (DCFT), the Stanford (straight channel) Cylindrical Cusped Field Thruster (CCFT), and the Princeton Cylindrical Hall Thruster (CHT). All three of these variants were operated by Stanford researchers during this grant period. Stanford received possession of a copy of a DCFT from MIT in the end of the first year of the grant, and is currently testing at Stanford, both the DCFT and the CCFT. Research on all three of these cusped thrusters was also carried out by Stanford researchers on assignment at the Air Force Research Laboratories at Edwards AFB. This included Laser-Induced Fluorescence (LIF) velocimetry mapping of the ion velocity field. (described in more detail later in the report).

S1.1 Background

The growing interest in the miniaturization of spacecraft is fueling increased development of low power electric propulsion. Yet, there are only relatively few plasma propulsion technologies that can currently service this regime. One such device is the Hall thruster; however, as operating powers decrease these thrusters appear to suffer a severe degradation of performance. Hall thrusters that operate nominally at 200 W have demonstrated anode efficiencies in the 40% range, although the efficiencies drop dramatically below 100 W. One reason for this diminished performance is heat loading of the center pole piece, which seems to experience significant electron bombardment. Another is the poorly understood scaling of cross-field transport, which meters the flow of electrons to the anode. Clearly, future advances in efficient, sub-100W Hall thrusters depend upon successfully addressing these issues.

One method of avoiding the vulnerabilities of the central pole piece is to remove it altogether, as done in the three thruster variants studied as part of Stanford's portion of this grant. The three thruster variants includes the Cylindrical Hall Thruster (CHT) [S1] which is a thruster designed and developed by the Princeton team. The CHT preserves the cross-field structure for metering electron flow to the anode, and thus retains the essential character of a Hall thruster. In addition, the cylindrical design, coupled with the introduction of magnetic cusps for partial electron mirroring from the walls, increases the electron residence time in regions downstream of the anode trap. These magnetic structures create efficient ionization regions, helping to maintain performance at lower power. The CHT has demonstrated anode efficiencies ranging from about 20-28% between 100 and 200W. Details on the work carried out by the Princeton team is described in their separate final report on this larger effort. Below, we describe briefly, our measurements of Laser-Induced Fluorescence studies of ion transport.

Another thruster variant is the Divergent Cusped-field Thruster (DCFT), designed and developed by the Massachusetts Institute of Technology (MIT)[S2]. MIT revisited the idea of using a series of cusps to magnetostatically trap electrons in a cylindrical discharge cavity. This design departs from traditional Hall thrusters, as the characteristic cross-field region upstream of the anode is eliminated entirely. Rather, the anode is placed in regions of magnetic field convergence along the thruster axis, at the base of the discharge channel. In

utilizing permanent magnets, the design sacrifices the ability to meter electron flow to the anode via in-situ tuning of the magnetic field. This is accomplished instead by manipulating the magnetic mirror ratio through a combination of design parameters: the anode position relative to the magnetic field, the shape of the outer magnetic cusps, and the interior region within these cusps where electrons collide with the ceramic insulator lining the channel. In the MIT design, the overall magnetic field strength diminishes along the centerline, with the series of three magnetic cusps following the diverging conical channel downstream of the anode. The geometry of the channel, coupled with its unique magnetic field structure, has led to its description as the Diverging Cusped Field (DCF) Thruster. Preliminary performance testing suggests that this thruster operates with an anode thrust efficiency in excess of 40% in the 200 W range – an exciting result, especially given its largely un-optimized operation and notable lack of the inherent vulnerabilities plaguing Hall thrusters operating in the low power regime.

The Stanford contribution described in this task was to also study a smaller DCF variant with straight, rather than diverging, channel walls. The magnetic field structure is qualitatively similar to the MIT DCFT, with stronger cusps located closer to the anode and a diminishing field downstream along the axis. However, the discharge channel is cylindrical, and does not follow the contours of the magnetic field lines extending out into the plume. In this way, we attempt to separate the role played by the diverging channel from that of the diverging field lines within the channel. As described below, we find that the resulting thruster behavior, including the ion plume current, is qualitatively similar to that of the MIT design. We also find that the straight channel and reduction in size do not significantly compromise performance, and consistent anode efficiencies near 23% are obtained when operating with krypton as a propellant at power levels as low as 40 W. The thruster described here is operated over a range of anode powers extending to 240 W, and its performance is found to strongly depend on the location and orientation of the cathode. This DCF thruster (referred to as the Stanford Cylindrical Cusped Field Thruster CCFT) also exhibits certain irreproducible modes of operation that drastically affect its performance both beneficially and detrimentally.

S1.2 Stanford CCFT Thruster

Details of the construction of the DCFT can be found in the MIT portions of the final report. Stanford did not play a role in their design. Here, we describe primarily the design of the CCFT. The design of the CHT is described in Ref. S1.

The Stanford CCFT is housed in a 6.10 cm outer diameter, 4.78 cm inner diameter aluminum cylinder that is 7.04 cm in length with the base plate attached (see schematic in Fig. S1). The partially threaded, 0.64 cm diameter graphite anode is kept electrically insulated from the floating aluminum body and plasma discharge with various boron nitride insulators and an alumina sleeve, with only a circular area of 1.29 cm² left exposed to the main channel. The magnetic cusped profile (indicated with gray lines on Fig. S1) is created by three samarium cobalt permanent magnets of decreasing height placed same pole-to-pole, and shaped by various 1018 steel components. Boron nitride risers of 0.32 cm height allow the magnetic mirror ratio to be controlled through the anode position relative to these magnetic field lines. The current position is chosen such that the field lines from the lower magnetic cusp are orthogonal to the surface of the anode, yielding a typical mirror ratio (B_{max}/B_{min}) of 1.6. Krypton propellant is injected through a 0.32 cm diameter stainless steel gas line into the propellant channel, where it is distributed evenly into the main discharge

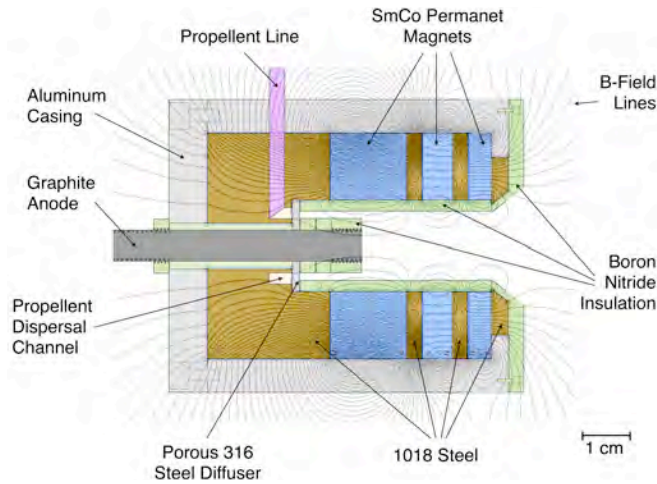


Figure S1. SCFT schematic, with magnetic field lines superimposed from Finite Element Method Magnetics (FEMM) simulations.

An electron-emitting cathode (or neutralizer) is positioned outside of the exit plane of the thruster. Some electrons emitted by the external cathode migrate along magnetic field lines down into the thruster channel to service the discharge, while the remainder are expelled to neutralize the ion plume. The series of magnetic cusps within the thruster trap incoming electrons between them through magnetic mirroring, unlike the azimuthal trapping of electrons seen in conventional Hall thrusters. These cusps, as well as the convergence of the field lines at the anode surface, meter the electron flow to the anode and create regions of efficient ionization of the propellant gas. Fuel is injected below the exposed anode tip at the base of the main channel. The distribution of cathode electrons throughout the discharge channel creates an electric field that accelerates singly- or multiply-ionized gas particles out of the thruster; the ions will be neutralized again by the cathode after imparting a reactive propulsive force to the thruster in the opposite direction. The SCFT operating on krypton at Stanford's vacuum facility is shown in the photograph in Fig. S2a), while a close-up of a peculiar feature of the discharge – a toroid, or plasma “donut” located near the thruster exit plane – is shown in Fig. S2b). The existence of this phenomenon is suspected to indicate a region of strong ionization.

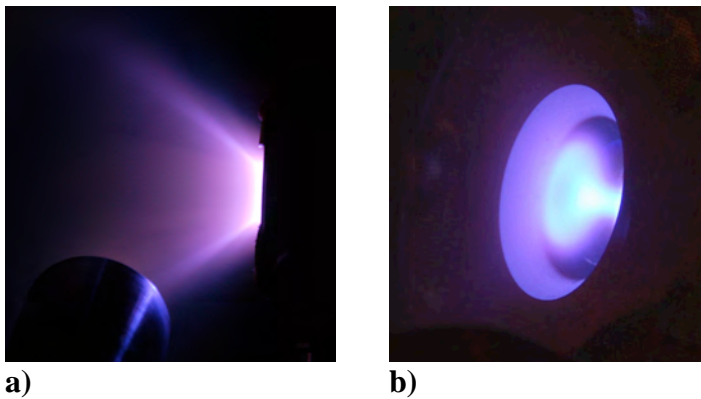


Figure S2.a) DCF Thruster in operation on krypton at the Stanford Plasma Physics Laboratory. b) The plasma “donut” surmised to indicate a region of strong propellant ionization.

channel through a 316 steel diffuser ring with 10 μm pores. The cylindrical discharge channel is 3.97 cm in length and 1.43 cm in diameter, an 88% reduction in enclosed channel volume from the MIT DCF thruster. The slightly diverging geometry at the exit plane of the thruster ensures that field lines from the cathode area (and therefore electron trajectories) point into the main channel, rather than impacting only against the exterior front plane of the thruster.

The governing principles of the CCFT thruster operation are similar in some ways to those utilized by traditional Hall thrusters and the CHT.

Performance Testing

In order to obtain benchmark operating conditions for this new thruster, current-voltage (IV) profiles for several different flow rates of krypton were taken (see Fig. S3). The anode power supply was maintained in voltage-limited mode throughout the tests, with the electrical data read directly off the power supply (introducing the ~1% overestimation of the discharge current mentioned

earlier). Voltage was scaled up and down to test for hysteresis in the thruster response, which is shown to be mostly negligible. However, in later testing care was taken to allow the thruster to come to equilibrium after making any changes to the operating conditions. The CCFT operates under a wide range of anode powers, varying from 27 W to over 230 W, with glow modes exhibited at values as low as 8 W.

A point exists where the slope of the IV curve begins to approach zero: here, the thruster draws no additional current with increasing voltage to complete ionization of the propellant. In this case, we assume that there is no further gain in efficiency with the increase in power (other than perhaps, a reduction in divergence losses). Thus, it is advantageous to choose operating points at the onset of IV “plateaus,” where the thruster draws just enough current to have efficiently ionized the propellant. Based on these criteria, we chose to use 8.2 sccm of flow with the anode potential set at 300 V (at which point the anode current was near 0.37 A) for the majority of our diagnostics, noting that this point falls near the middle of available flow rates and operating powers.

A variety of thrust performance experiments were carried out on the CCFT. First, the cathode was fixed to the thruster at an axial distance z of 2.8 cm (± 1 mm) away from the exit plane and a radial distance r of 3.85 cm (± 1 mm) away from the central thruster axis. In all performance tests, the cathode was pointed orthogonal to the thruster’s central axis, parallel to the exit plane with the central axis of the cathode passing through the central axis of the thruster. Thrust data was taken at three different voltages for each of three flow rates: 10.5, 8.2, and 5.9 sccm of krypton propellant, giving nine distinct operating points. A variety of factors (nonlinearity in the thrust stand response and uncertainty in the precise orientation of the thruster, for example) contribute to uncertainty in the thrust measurement. We estimate the magnitude of this uncertainty to be within 20% of the measured value, and for the results that follow, only the measured value is reported (error bars are omitted for the sake of clarity).

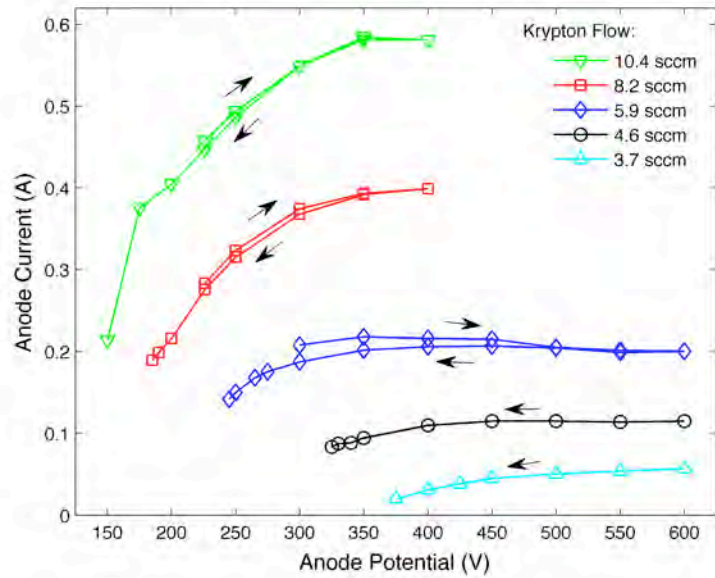


Figure S3. Current-voltage curves demonstrating CCFT thruster operation over a variety of krypton flow rates and anode powers. The thruster was operated in voltage-limited mode.

The resulting thrusts (in mN), calculated anode efficiencies η_a , and observed IV curves for the nine points are shown in Fig. S4. The IV curves from this test show excellent agreement with those obtained previously, indicating repeatability in thruster operation. Our chosen point of 8.2 sccm, 300 V, and 0.36 A (in this case) is shown to yield a mid-range thrust of 4.9 mN with one of the highest efficiencies of 21.7%. Interestingly, the lowest flow rate of 5.9 sccm demonstrated some of the highest efficiency values measured, along with the expected lowest measured values of thrust. We also note one of the DCFT’s most impressive operating

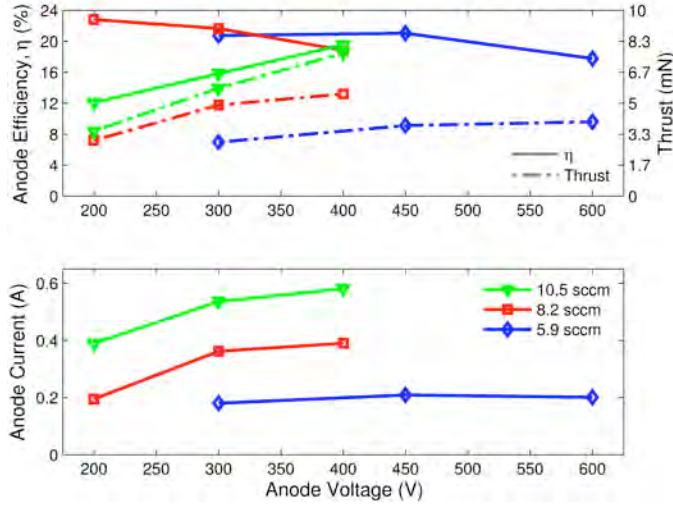


Figure S4.DCF thruster performance and operating points on krypton. The cathode was placed at $z = 2.85$ cm (± 1 mm) and $r = 3.85$ cm (± 1 mm).

covered a greater spatial range, while the other included more tightly-spaced measurements) to discern the dependency of anode efficiency on cathode location. The operating point during both tests was 8.2 sccm of krypton flow at an anode potential of 300 V; the anode current varied between 0.35 A and 0.40 A as r was varied. The results are superimposed over a map of the near-field region of the DCF thruster along with simulated magnetic field lines calculated from Finite Element Method Magnetics (FEMM) software in Fig. S5. Measurements in both tests were taken at $z = 3$ cm (± 1 mm), which is indicated with an arrow to the scale of the drawing. Thruster performance data at the common spatial points of measurement between the two tests (3.0, 4.0, 5.0, and 6.0 cm) was, on average, within 2.2% of each other for the measured thrust, and within 5.6% of each other for the calculated efficiency, demonstrating the repeatability in operation of the DCF thruster. As indicated by the finely spaced data, thruster performance is highly dependent upon radial cathode position, with shifts in measured thrust of 14% and in calculated efficiency of almost 30% (relative) occurring in the span of a 0.25 cm change in cathode location. There is a general decrease in performance between 2.0 and 6.0 cm (with a few exceptions), which may be due to cathode electrons approaching the critical pitch angle (angle between an electron's velocity and the

points: 22.8% efficiency at an anode power of only 39 W. Anode efficiencies over 20% are recorded up to 110 W, but above this threshold performance diminishes.

The cathode was then moved to an external mount to allow for the radial distance r to the central thruster axis to be varied at fixed axial distance z . The thruster remained on the thrust stand and translation stages, so we expect to slightly overestimate the thrust since thrust reductions associated with momentum transfer collisions between ions and the cathode body are not accounted for in this configuration. Two such studies were conducted over a range of radial positions (one test

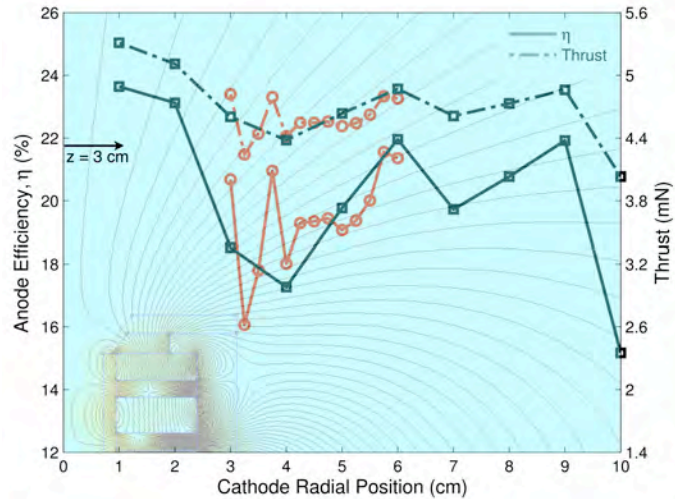


Figure S5.DCF thruster performance with varied cathode location, superimposed over the simulated magnetic field profile (FEMM). The cathode was scanned over r at fixed $z = 3.0$ cm (± 1 mm).

tangent to the magnetic field line that the electron is tracking) required for magnetic mirroring, the mechanism by which electron flow to the anode is metered. The highest region of efficiency is observed closest to the central axis, where one might expect to suffer the greatest losses from ion bombardment of the cathode in terms of both net thrust and cathode lifetime considerations.

Finally, the krypton performance characteristics of two different operating points (i.e. two different combinations of mass flow rate, discharge voltage, and discharge current) at a variety of cathode radial positions ranging from 3.0 cm and 6.0 cm were examined and compared to the existing data at 8.2 sccm and 300 V. The cathode axial position was set at 3 cm (± 1 mm) and oriented orthogonal to the thruster axis as discussed before, and suitable points were chosen from the better performing conditions from the data in Fig. S4. The results are summarized in Table S1.

The DCF thruster is shown to once again be repeatable in terms of required discharge power, with a deviation of around 4% compared with previous operation (Fig. S3) in both 5.9 sccm cases. The thrust measured, however, was generally lower than that seen previously at these points. The new measurements at the first and second operating points (denoted “OP 1”

Table S1: Performance comparison between thruster operating points at varied radial cathode location.

Point r (cm)	OP 1: 5.9 sccm, 300 V			OP 2: 5.9 sccm, 450 V			OP 3: 8.2 sccm, 300V		
	P_a (W)	T (mN)	η_a (%)	P_a (W)	T (mN)	η_a (%)	P_a (W)	T (mN)	η_a (%)
3.0	57	2.4	13.81	95	3.3	15.28	113	4.6	18.52
4.0	56	1.0	2.36	90	3.1	14.96	110	4.4	17.27
5.0	52	2.2	12.49	89	3.0	13.65	107	4.6	19.77
6.0	51	2.2	13.20	89	3.1	14.82	107	4.9	21.96

and “OP 2” in Table 1) did indicate a performance dip with the cathode located near $r = 4.0$ cm – an effect also observed with the original operating point at 8.2 sccm of flow (see Fig. S5). We expect that further investigation of this region with a finer spatial sampling would demonstrate the strong dependency of thrust efficiency on cathode location as seen before. Understanding the sensitivity of the thruster to cathode position is imperative to optimize the DCF thruster for near 50 W and 100 W operation.

Task Stanford-2. Laser-Induced Fluorescence Mapping of Ion Transport (Completed)

The Stanford component included mapping out ion transport (velocity, mean and distribution), inside the channel of the DCFT, CHT, and also the CCFT thruster described in Task S1. For this task, we employed laser-induced fluorescence (LIF), which is a diagnostic studied extensively within our laboratory. For the probing of the channel and near-field ion transport, we interrogated xenon ions (Xe II) through excitation of the $5d [4]^{7/2}$ - $6p [3]^{5/2}$ electronic transition at 834.7 nm. The hyperfine structure produced a total of 19 components, the constants of which are known for only the upper level of the transition, making the extraction of accurate velocity distributions tenuous. However, mean velocities were inferred with reasonable accuracy, and variations in the velocity distributions were elucidated. Ion velocity (within classes) is the result of the Doppler shift of the absorbing ions. These ions within the velocity class subsequently decay, through a transition originating from the same

upper state ($6p [3]^{5/2}$) and terminating on the $6s [2]^{3/2}$ state, resulting in strong fluorescence at 541.9 nm. This non-resonant fluorescence allows for fairly good signal to background collection, and has led to extremely high fidelity mapping of the velocity fields (and velocity distributions), as described later in this report. These LIF studies are the primary results of the two-year study carried out by the Stanford team.

Measurements employed a tunable diode laser that is capable of scanning over the range of the probed transition. Phase-sensitive detection was used to discriminate against background plasma emission. A main feature and novelty of Stanford experiments was to study the ion velocity evolution *inside the channel*. This was carried out without making holes or slots through the discharge as was performed in previous annular Hall thruster experiments. Instead, we measured the fluorescence in partial backscatter configuration, with the probe laser entering the channel axially.

S2.1 LIF Studies of Ion Transport in the MIT DCFT

To further understand the operation of cusped field thrusters, this task seeks to characterize the MIT DCFT variant using laser-induced fluorescence (LIF) velocimetry. A survey of the axial velocities within the acceleration channel and axial and radial velocities in the near-field of the plume of the DCFT is presented. As described in the MIT portion of this report, The DCFT incorporates permanent magnets of alternating polarity to create the cusped magnetic field profile while reducing thruster weight and power consumption by eliminating the magnetic circuit. Unlike the CCFT, it has a diverging, cone shaped channel to further minimize ion bombardment near the exit plane. It also has a hollow, cone-shaped plume where the highest current densities and highest ion velocities appear in a “jet” at an angle of 30 to 40 from the centerline of the thruster.

As described below, time-averaged xenon ion velocities for the thruster are derived from LIF measurements of the $5d [4]_{7/2} - 6p [3]_{5/2}$ xenon ion excited state transition at 834.72 nm. The measured spectral feature, which is a convolution of the ion velocity distribution function (VDF), and the transition lineshape, is used to determine the most probable velocities at various positions throughout the thruster channel and in the plume. These velocities are used to determine the ion kinetic energies and to estimate electric field strength along the centerline of the thruster.

The details of the DCFT are described elsewhere in this technical report. Briefly, the acceleration channel in the DCFT has a diverging, cone shape that is 49.5 mm in depth, 28

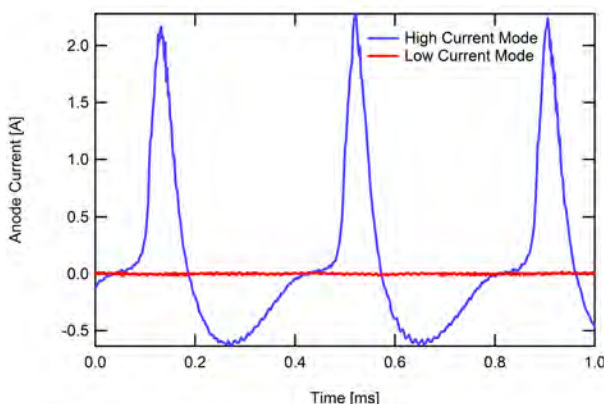


Figure S6. Anode current traces for high and low current operating conditions. Note: the current probe was AC coupled.

mm in radius at the exit plane, with a cone half angle of 22.5. Permanent magnets of alternating polarity are placed along the channel with decreasing strength as they approach the exit plane. This results in a magnetic field profile that is largely in the axial direction, with radial components at the magnet interfaces (i.e. cusps). The cusped magnetic fields produce a magnetic bottle effect for incoming electrons, trapping them between cusps where they mirror back and forth, allowing for a high ionization percentage and preventing

electrons from the external cathode from traveling directly to the anode. This design is intended to reduce erosion and wall losses by preventing the plasma from hitting the channel walls.

The MIT DCFT tends to operate in either a high current or low current mode. The high current mode is characterized by periodic oscillations in the discharge current, while the low current mode is quiescent, as shown by the anode current traces in Figure S6. The specifications for the high and low current operating conditions examined in this study are given in Tables S2 and S3. The high current mode, achieved by running the thruster with an $830 \mu\text{g/s}$ flow rate and 300 V anode potential, was chosen to match a highly efficient operating condition demonstrated in previous work at MIT [S3] while maintaining a power of less than 200 W. The 200 W restriction was imposed to prevent heat loading on the magnets from degrading the magnetic field significantly during long tests.

The second operating condition was chosen to demonstrate the low power mode of operation. Transitioning from high to low current mode can be achieved by either raising the applied anode voltage or by lowering the propellant flow rate to the anode. The first attempt at operating the thruster in the low current mode by raising the voltage to 400 V while maintaining $830 \mu\text{g/s}$ of flow rate proved unsuccessful, as the thruster reverted back to the high current mode within about 30 minutes. To maintain operation in the low current mode while keeping the operating power less than 200 W, it was necessary to both raise the voltage and lower the anode flow rate. The resulting low current operating condition used in this study had an anode potential of 400 V and flow rate of $590 \mu\text{g/s}$. Both conditions were run with a background chamber pressure of 5×10^{-6} Torr during thruster operation (corrected for xenon).

In this experiment, LIF is used to measure the most probable velocities of ions in the thruster channel and plume. LIF is a particularly useful diagnostic for electric propulsion

Table S2: High current operating conditions.

Anode Flow	$830 \mu\text{g/s Xe}$
Cathode Flow	$150 \mu\text{g/s Xe}$
Anode Potential	300 V
Anode Current	0.53 A
Keeper Current	0.50 A
Heater Current	3.0 A

Table S3: Low current operating conditions.

Anode Flow	$590 \mu\text{g/sXe}$
Cathode Flow	$150 \mu\text{g/s Xe}$
Anode Potential	400 V
Anode Current	0.17 A
Keeper Current	0.50 A
Heater Current	3.0 A

devices such as the DCFT where plasmas create harsh, non-uniform environments. It is a spatially resolved measurement and is non-intrusive by nature, as compared to electrostatic probes which physically perturb the operation of the plasma they are trying to measure.

Ion velocity measurements are accomplished by probing the $5d [4]7/2 - 6p [3]5/2$ electronic transition of Xe II at 834.72 nm. The upper state of this transition is shared by the relatively strong $6s [2]3/2 - 6p [3]5/2$ transition at 541.92 nm [S4], allowing for non-resonant fluorescence collection. Ion velocities are determined by measuring the Doppler shift of the absorbing ions. Benefits of the $5d [4]7/2 - 6p[3]5/2$ transition include the ease of accessibility using a cw diode laser, and the option of non-resonant fluorescence collection using the $6s[2]3/2-6p[3]5/2$ transition which mitigates noise induced by surface reflections of the probe beam. One drawback to this transition is that for the 19 isotopic and spin split components contributing to

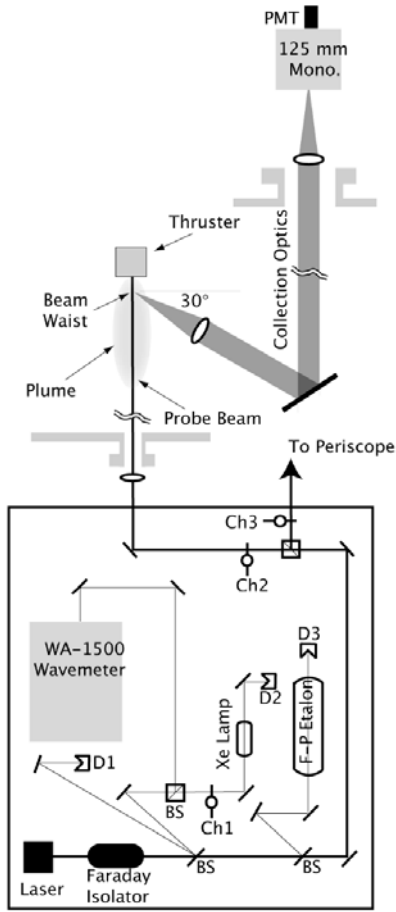


Figure S7. Top view diagram of the laser optical train and collection optics. Note that the radial probe beam periscope and focusing optics are not shown.

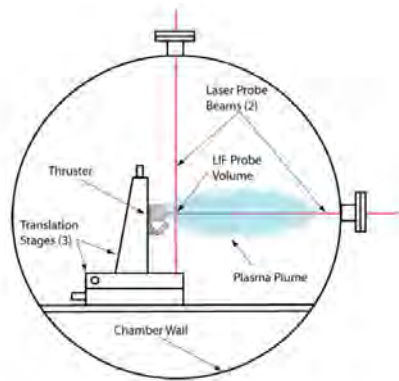


Figure S8. Side view diagram of thruster within AFRL chamber 6. Also shown are the translation stages and the laser probe beams. Note that the fluorescence collection and external optics are not shown.

the hyperfine structure of the $5d[4]7/2-6p[3]5/2$ xenon ion transition, only the $6p[3]5/2$ upper state has confirmed nuclear spin splitting constants [S5-S8]. The hyperfine splitting constants characterize the small variations in state energies associated with the odd-numbered isotopes, which contribute to broadening in the measured spectral feature. This transition was first used by Manzella [S9] to make velocity measurements in a Hall thruster plume. In that study, splitting constants for the similar $5d4D7/2-6p4P5/2$ transition at 605.1 nm were used in modeling the transition lineshape, and it was shown that Doppler broadening generally dominates the broadening mechanisms in these type of plasmas. The $5d[4]7/2-6p[3]5/2$ has since been used throughout the electric propulsion community to characterize a variety of thrusters operating on xenon [S10, S11].

LIF measurements for this study were performed at the Air Force Research Laboratory (AFRL) Electric Propulsion Laboratory at Edwards AFB, CA. Figure S7 shows a top view of the experimental set-up, including the thruster, one branch of the probe optics and the collection optics. The thruster is mounted on a system of orthogonal translation stages that allows for three axes of motion. The anode and cathode potentials are floating with respect to ground. The cathode is located to the side of the thruster opposite to the collection optics with the tip at a radial distance of 40 mm from the centerline and axial distance of 28 mm from the exit plane with its axis oriented at an angle of 70° degrees with respect to the outward normal to the exit plane. The laser is a New Focus Vortex TLB-6017 tunable diode laser, capable of tuning approximately ± 50 GHz about a center wavelength of 834.72 nm. The 10 mW beam is passed through several beam pick-offs followed by a 50-50 cube beam splitter where it is split into two beams of equal power, approximately 5 mW each. The axial probe beam, shown in both Figures S7 and S8, is focused by a lens and enters the vacuum chamber through a window. The radial beam, shown in Figure S8 only, is

periscoped from the optical bench to the top of the chamber such that it enters the chamber from above the thruster and probes the velocity perpendicular to the axial beam. Each probe beam is chopped at a unique frequency by choppers Ch2 (2kHz) and Ch3 (2.8 kHz) for phase sensitive detection of the fluorescence signals.

The two wedge beam splitters (BS) shown in Figure S7 provide portions of the beam for wavelength and velocity calibration. These include use of a commercial wavelength meter and a 300 MHz free spectral range Fabry-Perot etalon (F-P) to discharge lamp to provide a stationary absorption reference for the determination of the unshifted spectral line position (zero velocity reference). The xenon lamp has no detectable population of the ionic xenon $5d[4]7/2$ state, therefore the nearby (estimated to be 18.1 GHz distant) neutral xenon $6s0[1/2]1-6p0[3/2]2$ transition at 834.68 nm is used for the reference. The fluorescence collection optics are also shown in Figure S8. The fluorescence is collected by a 75 mm diameter, 300 mm focal length lens within the chamber and oriented 60° from the probe beam axis. The plume divergence half angle of DCFT has previously been measured as 70° for 90% of the integrated beam current. However, the peak ion flux lies between 30° and 40° and drops off by more than 75% by the 70° point. By placing the LIF collection optics at 60° off this axis it is possible to interrogate points along the centerline up to 20 mm inside the thruster acceleration channel, while keeping the lenses and mirrors away from much of the plume ion flux. In this way, it is possible to probe internal ion acceleration of the DCFT with minimal intrusion into the plume and without destroying the collection optics through sputtering. The collimated fluorescence signal is directed through a window in the chamber side wall to a similar lens that focuses the collected fluorescence onto the entrance slit of the 125 mm focal length monochromator with a photomultiplier tube (PMT) at its exit. Due to the 1:1 magnification of the collection optics, the spatial resolution of the measurements is determined by the geometry of the entrance slit (0.7 mm width and 1.5 mm height) as well as the sub-mm diameter of the probe beam.

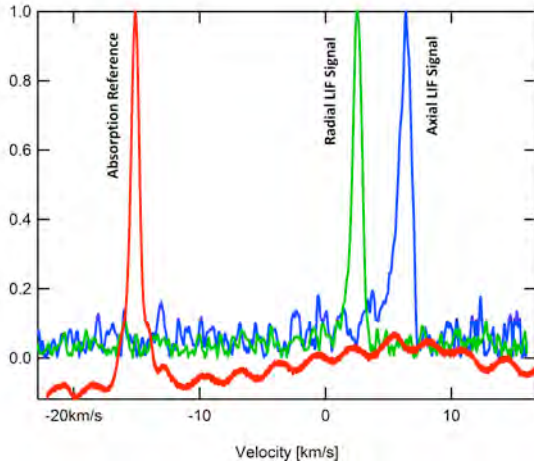


Figure S9. Example of LIF and absorption traces taken at $r = 4$ mm and $z = 4$ mm.

The combination of thruster geometry and collection optics allows for a large region of the DCFT channel and plume to be interrogated; however, lower S/N closer to the anode and along the centerline of the plume limit the measurements that are meaningful. The current density along the centerline of the thruster is far less than that seen in the jet between 30° and 40° . For the high current mode, the centerline current density is a factor of two less than that in the jet, while for the low current mode, it is a full order of magnitude less creating a hollow plume. In this region, the S/N is much lower than in the jet, since the fluorescence signal strength is strongly

dependent on the number density of excited ions. The uncertainty of the velocity measurements is estimated to be within ± 500 m/s for the most probable values. The repeatability of the peak locations appears to be a fraction of the quoted uncertainty. However, the fluorescence line shapes are often significantly broadened, presumably due to

wide velocity distributions caused by plasma fluctuations. The quoted uncertainty should therefore be viewed as the uncertainty in the determination of the peak of the fluorescence line shape. Measurements confirm that this combination of apparatus and laser power are well within the linear fluorescence regime.

As described above, two operating conditions are presented in this LIF study of the DCFT: a high current mode, for which the anode discharge current is oscillatory; and a low current mode for which the anode discharge is quiescent. The ion velocities presented in this study represent most probable (or peak) values calculated using the shift relative to the stationary reference in the LIF excitation profile, as shown in Figure S9. At this point, velocity distribution functions are not extracted from the measured unsaturated lineshapes because we cannot say with certainty that the spectral lines are not significantly affected by Zeeman splitting. The most probable ion velocities are therefore used to show trends in the data, and in some cases to estimate the electric field from corresponding changes in kinetic energy.

The most probable ion velocities for both the high and low current conditions are presented as contour plots in Figures S10 to S15. In each case, the magnetic field profile and location of the LIF measurements are overlaid. The magnetic field lines shown are for visualization of the field direction, and their spacing should not be taken as indicative of the varying magnetic field strengths. The contour plot was achieved by forming a rectangular grid with 4 mm spacing in the axial and radial directions and using a weighted average dependent on the distance between points to interpolate the data. Therefore, the contours directly surrounding the data points can be considered to be most accurate, while those not surrounding data points (i.e. in the hollow center of the plume) are meant only to continue the trends seen in the measurements.

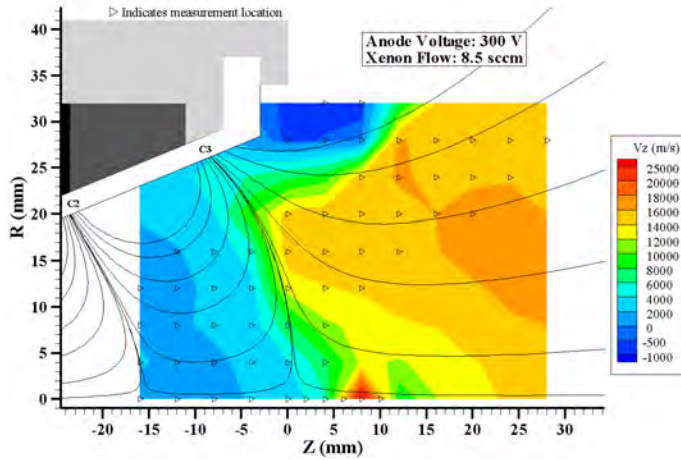


Figure S10. Contour plot of most probable axial ion velocities for the high current operating condition, including magnetic field line overlay.

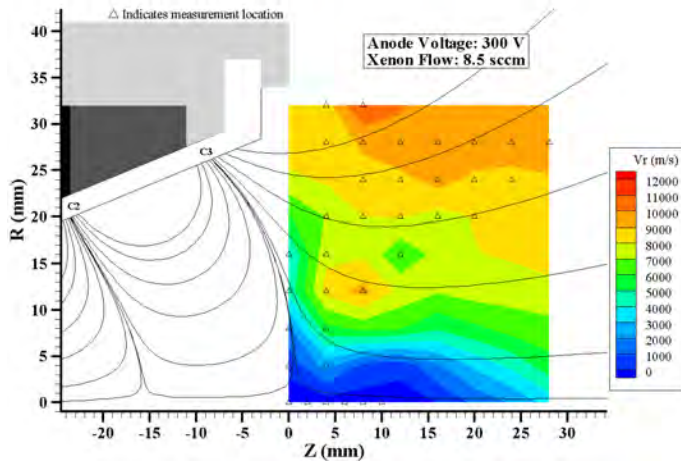


Figure S11. Contour plot of most probable radial ion velocities for the high current operating condition, including magnetic field line overlay.

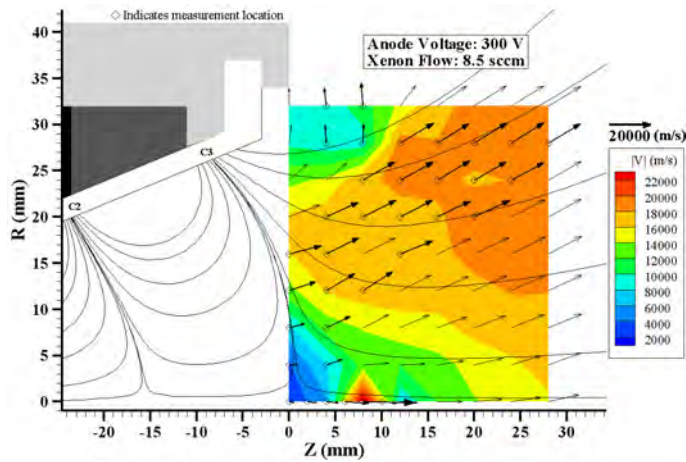


Figure S12. Contour plot of the magnitude of the total most probable ion velocities for the high current operating condition, including magnetic field line overlay. Arrows indicate the direction of the velocities.

S2.1.1 High Current Mode

Figures S10 through S12 show contour plots of the most probable xenon ion velocities measured for the high current mode of operation. We see from Figure S10 that the majority of the high speed ions ($v > 15$ km/s) reside in the plume outside of the thruster, just beyond the third magnetic cusp. Rapid axial acceleration appears to occur perpendicular to the magnetic separatrix of this most downstream cusp. It is interesting to note that some acceleration occurs upstream of this point, most probably in the vicinity of the second cusp, although measurements were not able to be taken far enough upstream to resolve this region of the flow. It is also apparent that at any axial location, the ions are generally slowest near the centerline and faster at approximately 2/3 of the exit radius, with lines of constant velocity following along the separatrices of the last two cusps. The contour plot of the radial velocities indicates that the highest radial velocities occur in the jet region of the plume at a radius of 25 mm or more off-axis. In this jet region, the radial velocities are of comparable magnitude to the axial velocities (e.g. around 16,000 m/s axial, 10,000 m/s radial), which is indicative of the highly divergent nature of cusped field thrusters. Along the centerline of the thruster, there is little to no radial velocity. This is in contrast to the CHT-30 thruster in which there appears to be a convergence of the velocity field towards the axis [S12]. This also differs from the ion velocity

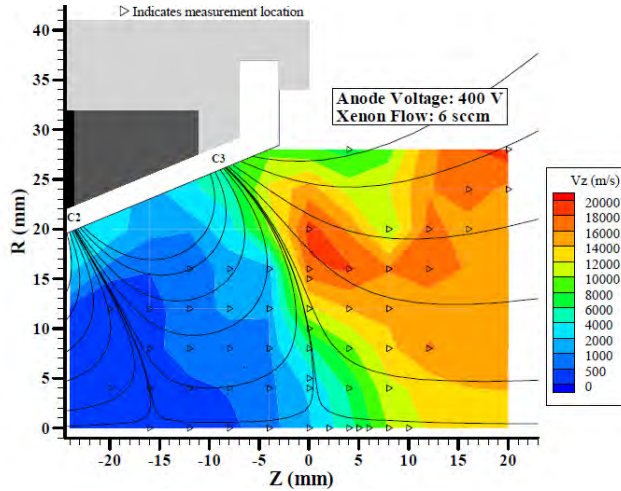


Figure S13. Contour plot of most probable axial ion velocities for the low current operating condition, including magnetic field line overlay.

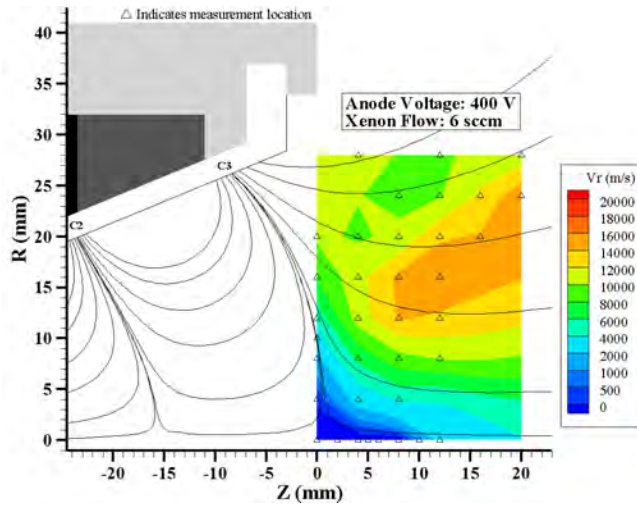


Figure S14. Contour plot of most probable radial ion velocities for the low current operating condition, including magnetic field line overlay.

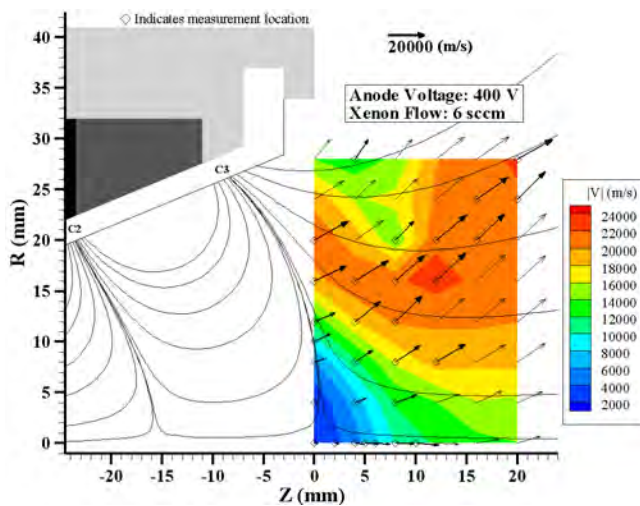


Figure S15. Contour plot of the magnitude of the total most probable ion velocities for the low current operating condition, including magnetic field line overlay.

fields seen in many traditional Hall thrusters where there is a mixing region in front of the nosecone where ions from opposite sides of the annular thruster channel cross paths due to their inward-directed radial velocities originating along the channel centerline. Figure S12 provides a contour plot of the overall magnitude of the ion velocity. Superimposed in this figure are vectors pointing along the local ion flow direction, the lengths of which are equal to the local ion speed. We see that close to the separatrix of the third cusp, the ion acceleration appears to be normal to the field line, suggesting that the field lines near the cusps represent lines of low parallel resistivity. This correlation between the direction of ion velocity and the direction normal to the field lines breaks down further downstream of the cusp, and by approximately 15 mm into the plume it appears that the ions begin to follow the divergent magnetic field. While it is tempting to believe that ions may be tied to the magnetic field by the nature of their trajectories, the relatively large ion Larmor radius (> 0.1 m) in this region of the flow suggests that the ion trajectories are initially defined by the accelerations experienced further upstream, while still experiencing small corrections by the electrostatic influence of strongly magnetized electrons that are tied to the field lines further downstream of the cusps.

Measurements taken along the z -axis indicate that for the high current mode, there is a strong acceleration and subsequent deceleration seen between axial locations of 5, 11, and

15 mm. In the present experiments, this is a region of very low signal to noise, and so these data should be interpreted with caution. The ion transport in this region should be re-examined in future studies, with longer scan durations.

The low current mode of operation is achieved by lowering the anode flow rate as well as raising the applied anode potential. As mentioned above, the low current mode operated without strong oscillations in the discharge current. The lower flow rate made the discharge visibly less bright than that of the high current mode of operation, indicating that there are fewer xenon atoms occupying excited electronic states. This resulted in fewer positions from which data can be obtained with sufficiently high S/N to make meaningful measurements of velocity.

S2.1.2 High Current Mode

Figures S13 and S14 depict contour plots (with measurement locations and magnetic field lines superimposed) of the most probable axial and radial xenon ion velocities measured for the low current mode of operation, respectively. Figure S15 gives the magnitude of the total ion velocity, with vectors indicating the direction of the flow. In general, the contour plots of the low current mode of operation show some similar trends to those seen in the high current mode. However, there are several ion velocity field characteristics that distinguish this low current mode from its oscillatory, more diffuse counterpart. For example, an examination of Figure S13 reveals that there is a more abrupt axial acceleration taking place along the separatrix of the third cusp. Upstream of this separatrix, the ion velocities seem to be very low, suggesting that in the low current mode, less acceleration (if any) takes place near the second cusp. Also, the rapid acceleration and high ion velocities seen along the centerline in Figure S9 is not apparent in the low current case. An examination of Figure S14 reveals that there are strong radial components to the ion velocity as close as 10 mm from the centerline. The development of a strong radial component so close to the axis, results in a much stronger divergence of the ion beam when compared to the flow field for the low current mode depicted in Figure S12. Visually comparing the thruster plumes, it appears that they have similar divergence half angles (between 30° and 40°), however the low current mode shows a distinct, more luminous jet at this angle, whereas the high current mode is luminous throughout the center of the cone, not appearing as hollow. The differences in velocity fields presented here must be interpreted with caution, as the LIF measurements are averaged over

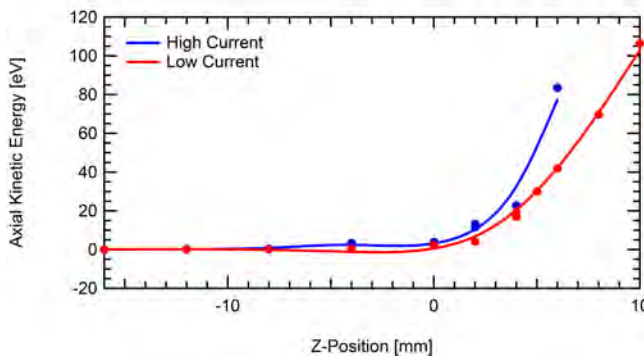


Figure S16. Axial kinetic energies derived from the most probable axial ion velocities along centerline of thruster plume.

time. While the low current mode has a quiescent discharge current, the high current mode exhibits strong low frequency (3 kHz) [S2] discharge current oscillations indicative perhaps of a fluctuation in the position of the ionization zone. Such a fluctuation can partially explain the deeper extension of the acceleration (closer to the second cusp) that is seen in this high current mode, and the lower concentration of ion flux in the conical jet [S2]. This behavior would be best resolved with

a velocity diagnostic capable of being synchronized to the discharge current oscillations.

S2.1.3. Centerline Kinetic Energy and Electric Fields

Figure S16 depicts the variation in the most probable axial ion kinetic energy along the centerline of the thruster, which we can assume is a probable streamline for ions born along the centerline. Along the centerline, acceleration to a given kinetic energy occurs sooner for the case of the high current mode, but in both cases, acceleration tends to increase rapidly beyond the thruster exit plane. This centerline energy can be used to estimate the electric field, assuming that the ionization takes place upstream of the axial location where the acceleration is seen. Figure S17 shows the implied axial electric fields corresponding to the data of Fig S16. These data suggest that the vast majority of the potential drop along the centerline of the thruster takes place well beyond the exit plane. It is noteworthy that preliminary emissive probe data taken along the centerline indicates that the region of strong

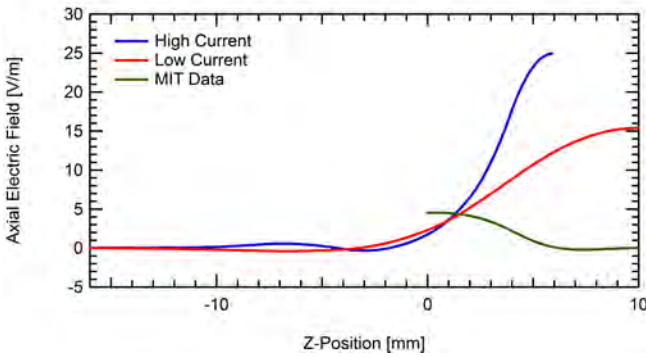


Figure S17. Axial electric fields derived from most probable kinetic energies along the centerline of the plume. The LIF derived electric fields are compared to the axial electric field derived from emissive probe plasma potential data.

electric field peaks very near the exit plane [S13]. While probe measurements must be interpreted with caution as they are inherently intrusive, the discrepancy can also be attributed, at least partially, to the possibility that ionization is more distributed along the axis than what is assumed in generating the data in Figure S17. However, the sudden acceleration that is defined by the increase in ion velocity at a location of approximately $z = 0$ mm (exit plane), as depicted by Figures S10, S13, and S15 is consistent with the location of where the separatrix from the third cusp intersects the thruster

centerline, suggesting perhaps that this strong magnetic flux surface forms a barrier to electron transport, defining a resistance to electron flow and a potential barrier for ion acceleration.

S2.2 LIF Studies of Ion Transport in the Stanford CCFT

This section focuses on LIF studies of the CCFT operating on xenon. As mentioned earlier, like the DCFT, the CCFT generates its cusped magnetic field profile by employing a series of permanent magnets of alternating polarity. The permanent magnets have varying strengths, weakening further downstream of the anode, to reproduce a similar magnetic field structure to that seen in the divergent design. However, unlike the DCFT, it has a straight cylindrical channel. As discussed above, our studies have shown that when operating on krypton, the CCFT demonstrated anode efficiencies of around 23% at power levels ranging from 40 to 240 W. The discharge did not exhibit the strongly oscillating mode seen in the DCFT in high current mode. While it is not yet clear how the straight configuration of the CCFT affects the discharge dynamics, we suspect that the quiescent nature to the discharge current may be attributable to the higher propellant density because of the non-divergent

channel. The work presented here seeks to characterize the CCFT operating with the more commonly-used xenon propellant and employs laser-induced fluorescence (LIF) from xenon ions to study the ion transport in the very near field of the discharge. This measured ion velocity, established as a result of the kinetic acceleration of ions in the imposed electric field, is interpreted in conjunction with plasma potential measurements acquired using an emissive probe.

Time-averaged xenon ion velocities for the thruster are derived from LIF measurements of the $5d\ [4]7/2 - 6p\ [3]5/2$ xenon ion excited state transition at 834.72 nm, as carried out on the DCFT described above. Details of the LIF diagnostics are similar to those studies and the description of the LIF facility and basic spectra will not be repeated. We have also carried out plasma potential measurements using a floating emissive probe and have compared the findings to the LIF data. These plasma potential measurements are described later in this report.

The thruster is pictured operating on xenon in Fig. S18. The photograph in this figure is a side view, with the exit of the cathode facing the direction of observation. Apparent in this figure is a bright, luminous conical region, similar to that seen in the DCFT, indicating that the shape of this luminous plasma is not the divergence of the channel, but rather, the magnetic field topology. Two operating conditions were examined in this study. The first was chosen to reproduce conditions seen in a previous study [S13] where extensive probe measurements were taken on the CCFT running on krypton propellant at 111 W anode power (these are described below). In these LIF studies the thruster was run using xenon as the propellant, with an applied anode potential of 300 V and propellant flow rate of $147\ \mu\text{g/s Xe}$

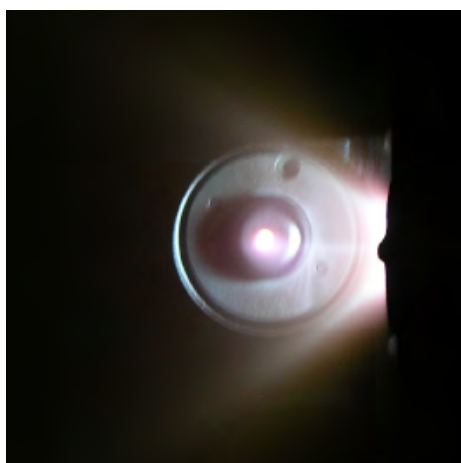


Figure S18. Photo of CCFT developed by Stanford operating on xenon propellant under power matched conditions.

to achieve the 111 W anode power. This condition is summarized in Table S4. The second operating condition, summarized in Table S5, was chosen to highlight the low power capabilities of this thruster, with an operating power of 43.5 W. Both operating conditions were very quiescent, showing no oscillations in anode discharge current.

As in the case of the LIF DCFT studies, laser-induced fluorescence measurements were performed by Stanford researchers at the Air Force Research Laboratory at Edwards AFB, CA. A Busek cathode was used as the electron source, with specifications described in Table S4. Plasma potential measurements (described later) at identical xenon operating conditions were performed at Stanford. During the tests at Stanford, an Iontech cathode was used, as a Busek cathode was unavailable. The slight differences in cathode operation appeared to have

little to no effect on the overall thruster behavior (as determined by the thruster operating characteristics); the thruster proved to be invariant to changes in supplied cathode current between 0.25 to 1.3 A. Cathode position has been shown to be more critical to thruster operation, and so the cathode was placed in the same position relative to the cylindrical channel for both sets of tests. The difference in background chamber pressures has been shown in previous work to affect ion acceleration, with higher pressures pushing the peaks in

Table S4. Power matched operating conditions.

Anode Flow	690 $\mu\text{g/s}$ Xe
Anode Potential	300 V
Anode Current	0.37 A

Table S5. Low power operating conditions.

Anode Flow	690 $\mu\text{g/s}$ Xe
Anode Potential	150 V
Anode Current	0.29 A

Table S6. Cathode operating conditions

Cathode	Cathode Flow	Heater Current	Keeper Current
Busek	150 $\mu\text{g/s}$ Xe	0.5 A	3.0 A
Iontech	140 $\mu\text{g/s}$ Ar	0.25 A	6.0 A

acceleration upstream towards the anode. The background chamber effects, and the inherently intrusive nature of emissive probes (as compared to the non-intrusive nature of laser diagnostics), should factor into the comparison of the LIF and plasma potential measurements made later.

The ion velocities presented here represent most probable (or peak) values in an axial ion velocity distribution calculated from the Doppler shift in laser fluorescence excitation spectrum relative to the absorption peak recorded in a stationary xenon discharge reference. Contour plots of the most probable axial ion velocities are shown in Figure S19, where (a) shows the power matched condition, and (b) shows the low power

condition. The symbols indicate measurement locations. Interpolation around these points is accomplished using an inverse-distance method. This interpolation scheme is representative of the analysis throughout these results. The white regions in the lower right hand corner of the plots represents the chamfered edge of the thruster channel, with the exit plane located at $z = 0$ mm.

For the power matched condition, the ions inside the thruster channel retain a relatively low axial velocity ($\sim 2,000$ m/s) along the thruster centerline. Off axis, at radial locations greater than $R = 6$ mm, the axial ion velocities increase significantly, especially near the chamfered edge of the thruster, which contains the outermost (third) magnetic cusp. As seen in Figure S19 (a), this third magnetic cusp intersects the center of the chamfered edge,

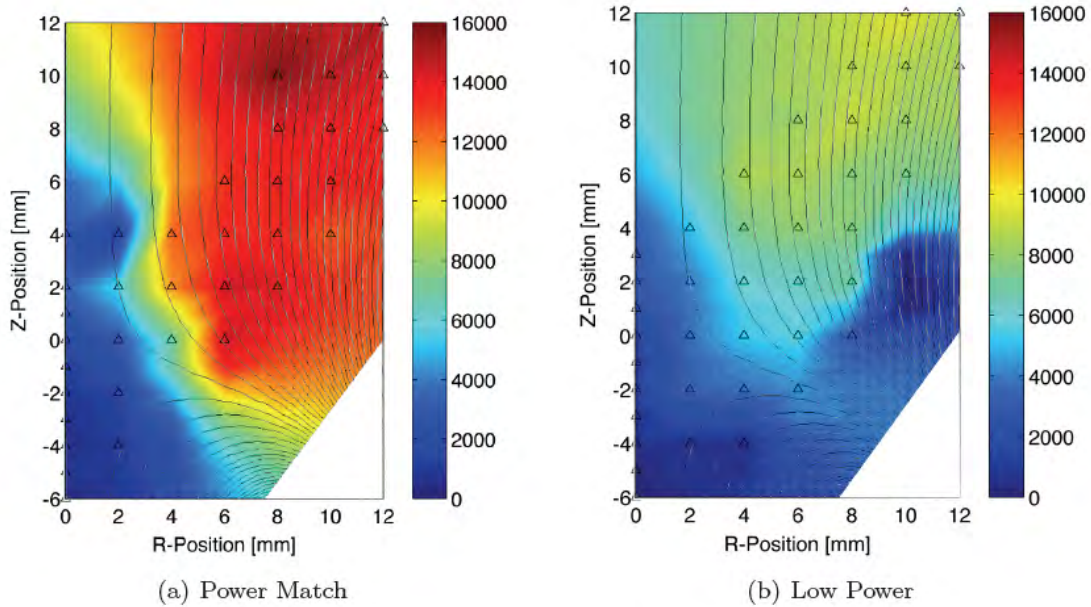


Figure S19. Most probable axial ion velocities for DCF operating under (a) power matched, and (b) low power operating conditions. Symbols indicate measurement locations.

defining a separatrix which appears to form a boundary between an ionization region characterized by low ion velocity, and a region of strong axial ion acceleration. It appears therefore, that there is a close relation between the separatrix and the plasma potential. Downstream of the separatrix, the ions reach a maximum axial velocity in this region of 15,600 m/s at $z = 10$ mm, $R = 8$ mm. In general, the ions with higher axial velocity appear away from the centerline, in the region corresponding to the visibly luminous, cone-shaped plume in Figure S19 (b). The low power operating condition shows similar trends in the contour plot of axial ion velocity, with the overall magnitudes being expectedly lower due to the lower applied anode potential (150 V vs. 300 V for the power matched condition). The lower velocity ions reside closer to the centerline inside the thruster, while higher velocity ions (reaching 9,600 m/s axial velocity) appear farther into the plume at radii > 8 mm. That the axial component of velocity peaks off-axis is even more apparent at this low power conditions, where at an axial location of $z = 2$ mm, the axial ion velocity peaks at a radial location of $r = 4$ mm. The boundary of the acceleration region does not appear to be as directly related to the separatrix near the exit plane of the thruster, indicating that the shaping of the plasma potential field by the magnetic topology depends on discharge operating conditions. We also find that the region of low axial ion velocity along the centerline does not extend as far into the plume. Rather, acceleration appears to occur at all radii across the exit plane between $z = 2$ mm and $z = 6$ mm. For example, the power matched condition has a peak axial ion velocity of 15,600 m/s and a maximum axial velocity of 9,400 m/s along the centerline, whereas the centerline axial velocity for the low power condition peaked at 6,500 m/s, which is more comparable in magnitude to the 9,600 m/s seen away from the centerline. When operating in the low power mode, the luminous region was distributed throughout the center of the plume instead of just the outer cone shaped region, and it was visibly less bright the power matched condition. This could be attributed, in part, to the more even distribution of ions moving throughout the cone shaped plume with lower average velocity.

S2.2 LIF Studies of Ion Transport in the Princeton CHT

The thruster undergoing LIF studies was the CHT-30 cylindrical Hall thruster developed by Princeton University. The CHT-30 has a 30 mm diameter channel that is composed of a short annular region near the anode followed by a 13 mm long cylindrical region as shown in Figure S20. This figure also indicates the magnetic field topology seen during the operation of the thruster. CHTs have been of interest in the electric propulsion community in recent years due to their low power operation and potential for long life. The low surface-to-volume ratio of their acceleration channel and cusped magnetic field configuration result in low erosion rates of their ceramic wall materials, which is especially desirable when scaling down in power. CHTs have also demonstrated performance levels approaching those of state-of-the-art annular Hall thrusters.

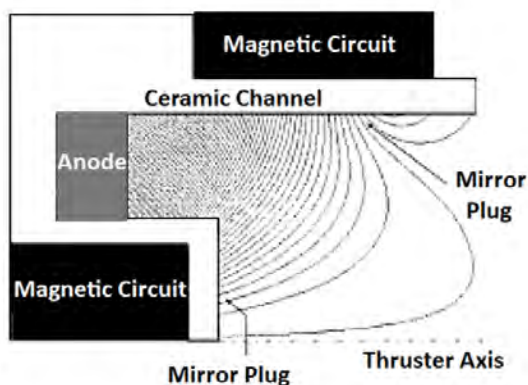


Figure S20. Schematic of the Princeton CHT with superimposed magnetic field lines.

differences appear to indicate that the electron transport mechanism within cusp thrusters also differ significantly. The azimuthal drift seen in conventional Hall thrusters is either lacking or occurs very near the anode of the cusp thruster. This suggests that the $E \times B$ shear that appears critical in annular Hall thruster electron transport does not exist, or assumes a very different form in cusp thrusters.

The operating conditions considered in this study were a nominal operating condition provided in Table S7, as well as reduced magnetic field condition provided in Table S8. The reduced magnetic field operating condition was chosen due to the quiescent operating mode

of the thruster and the improved fluorescence signal quality throughout the majority of the plume. It also gave insight into the influence of the magnetic field strength on the ion velocity profiles.

Although the CHT (and several other magnetic cusp electrostatic thrusters) have elements that superficially resemble Hall thrusters, this thruster type has several features that make it considerably different. First, the high magnetic field strengths within cusp thrusters suggest that the ions may be magnetized. Ion magnetization is understood not to exist in annular Hall thrusters. Furthermore, the geometry and magnetic field structure of cusp thrusters are notably different, with the cusped magnetic field shape seeing no analog in traditional Hall thrusters.

Table S7. Nominal CHT operating conditions

Anode Flow	390 $\mu\text{g/s Xe}$
Cathode Flow	98 $\mu\text{g/s Xe}$
Anode Potential	300 V
Anode Current	0.53 A
Keeper Current	OFF
Heater Current	5.0 A
Magnet 1 Current	3.00 A
Magnet 2 Current	2.00 A

Table S8. Reduced magnetic field CHT operating conditions

Anode Flow	390 $\mu\text{g/s Xe}$
Cathode Flow	150 $\mu\text{g/s Xe}$
Anode Potential	300 V
Anode Current	0.61 A
Keeper Current	0.30 A
Heater Current	5.0 A
Magnet 1 Current	2.00 A
Magnet 2 Current	2.00 A

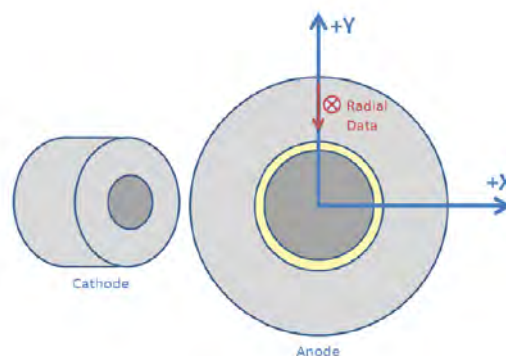


Figure S21. Coordinate system depiction used in these LIF studies.

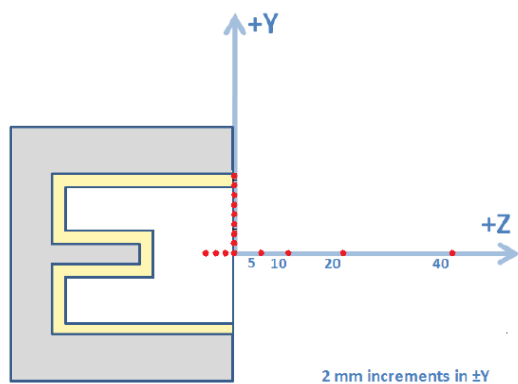


Figure S22. Location of data points for the axial and radial measurements in these LIF studies.

Figure S21 depicts the coordinate system used in these LIF measurements. Figure S22 shows a side view of the thruster channel and plume including the positions of the LIF data points examined in this paper. The thruster is mounted on a three axes orthogonal computer controlled translation system which allows for precise motion in the X-, Y- and Z-axes. Measurements at various Y-positions provided radial and axial data. In this study, ion velocity and subsequently derived kinetic energy distributions are presented along the centerline of the thruster axis at positions from $Z = -6$ mm to $+40$ mm into the plume.

The depth at which the data points could be collected inside the thruster channel was limited by the angle inside the thruster visible to the collection optics (60° from the leading edge of the channel). Additionally, distributions are presented along the exit plane of the thruster at $z = 0$ mm with a 2 mm spatial resolution in the Y-direction from $Y = 0$ mm to $+14$ mm.

Two operating conditions are presented in this study of the ion velocity and energy distributions of the CHT-30: a nominal operating condition and a condition with reduced magnetic field strength. The reduced magnetic field condition has approximately 70% of the magnetic field strength, and provides a quiescent operating mode of the thruster. Comparisons are made between these two conditions for positions along the centerline and across the exit plane of the thruster.

S2.3.1 Lineshape Analysis

Analysis of the fluorescence measurements made on the CHT-30 provides a great deal of information about the motion of the ions both in the channel and in the plume of the thruster. A raw LIF signal is a convolution of the ion velocity distribution function (VDF), and the transition lineshape (including broadening effects due to instruments, the finite linewidth of the laser, etc.). The transition lineshape is typically much narrower than the VDF and therefore the velocity distribution can often be represented directly by the raw LIF trace. It has previously been shown that the divergence between a deconvolved VDF and the raw LIF signal is small. Therefore, the ion velocity distributions presented in this paper are given by the raw fluorescence traces. Figures S23 and S24 show the analysis process for a fluorescence measurement taken at $Y = 0$ mm and $Z = 20$ mm. Figure S23 shows the raw absorption and LIF traces in relative frequency units. The Doppler shift relationship is used between the stationary absorption reference and the LIF traces to transform the frequency separation into velocity units, as shown in Figure S24. In this figure, the blue curve represents the axial VDF, while the black curve is the axial kinetic energy distribution. When normalized such that the total area under the curve is equal to unity, these traces represent the probability of an ion having a given velocity or kinetic energy at that spatial point.

In Figure S24, both the velocity and kinetic energy curves are normalized such that the peak is at a value of 1 (rather than area normalized). This is useful in determining the median values of velocity and kinetic energy. The green and red curves represent the integral of the

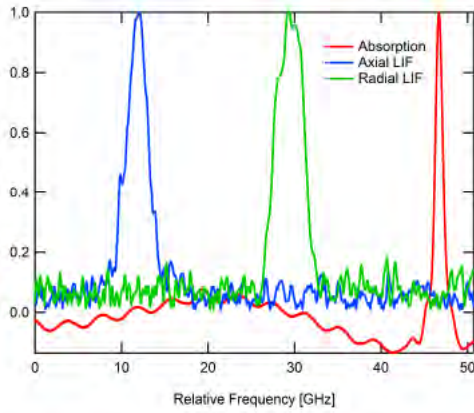


Figure S23. Example of LIF and absorption traces taken at $Y = 0$ mm and $Z = 20$ mm.

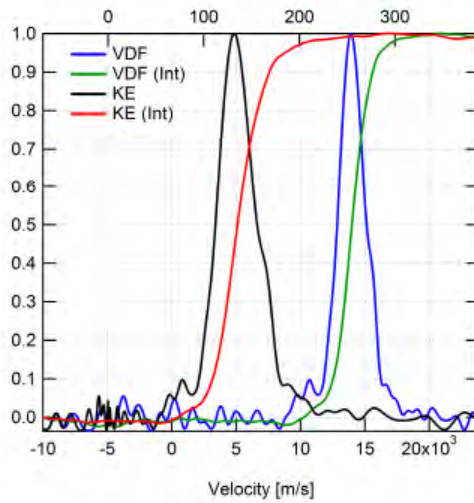


Figure S24. Lineshape analysis for axial ion velocity and kinetic energy distributions at $Y = 0$ mm, $Z = 20$ mm. VDF represents the velocity distribution function, KE represents the kinetic energy distribution function, and Int represents the integral of each function.

of the median value due to the integration of the noise. Therefore, while finding the most probable values of velocity have only an uncertainty of ± 500 m/s, the median values are closer to $\pm 1,000$ m/s to $1,500$ m/s. This method for analyzing the raw fluorescence traces is representative of the data analysis throughout this work. The median values of velocity and kinetic energy are reported, along with ranges for their distributions. Also, most probable values are used to show

velocity and kinetic energy curves, respectively. The point where these integrated lines crosses 0.5 indicates the median value on their corresponding velocity or kinetic energy distribution. At $Y = 0$ mm and $Z = 20$ mm, the median velocity is $14,000$ m/s, and the median kinetic energy is 138 eV.

To capture the range of velocities or energies over which the majority of ions are moving, it is possible to see where the integral curves meet a certain percentage above and below the 50% mark. For one standard deviation above and below the median value, approximately 68% of the ions have axial velocities between $12,700$ m/s and $15,200$ m/s (115 eV to 161 eV). Similarly, for two standard deviations, approximately 95% of the ions have an axial velocity between $10,600$ m/s and $17,200$ m/s (84.3 eV to 210 eV). In most cases the median values are very close to the mean values, due to the symmetry of the distributions (i.e. at $Y = 0$ mm and $Z = 20$ mm, the mean velocity is $13,900$ m/s and mean kinetic energy is 138 eV, the most probable velocity is $14,500$ m/s and most probable kinetic energy is 143 eV). For a pure Gaussian distribution, the mean, median and most probable (or peak) values are by definition identical. However, the oscillatory nature of these thrusters along with low fluorescence signal strength cause the fluorescence traces to have low SNR, mostly due to the baseline noise. The baseline noise introduces a larger uncertainty in the calculation

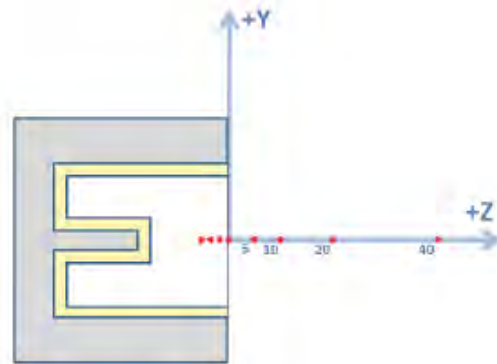


Figure S25. Location of data points for axial and radial LIF measurements along the centerline of the thruster.

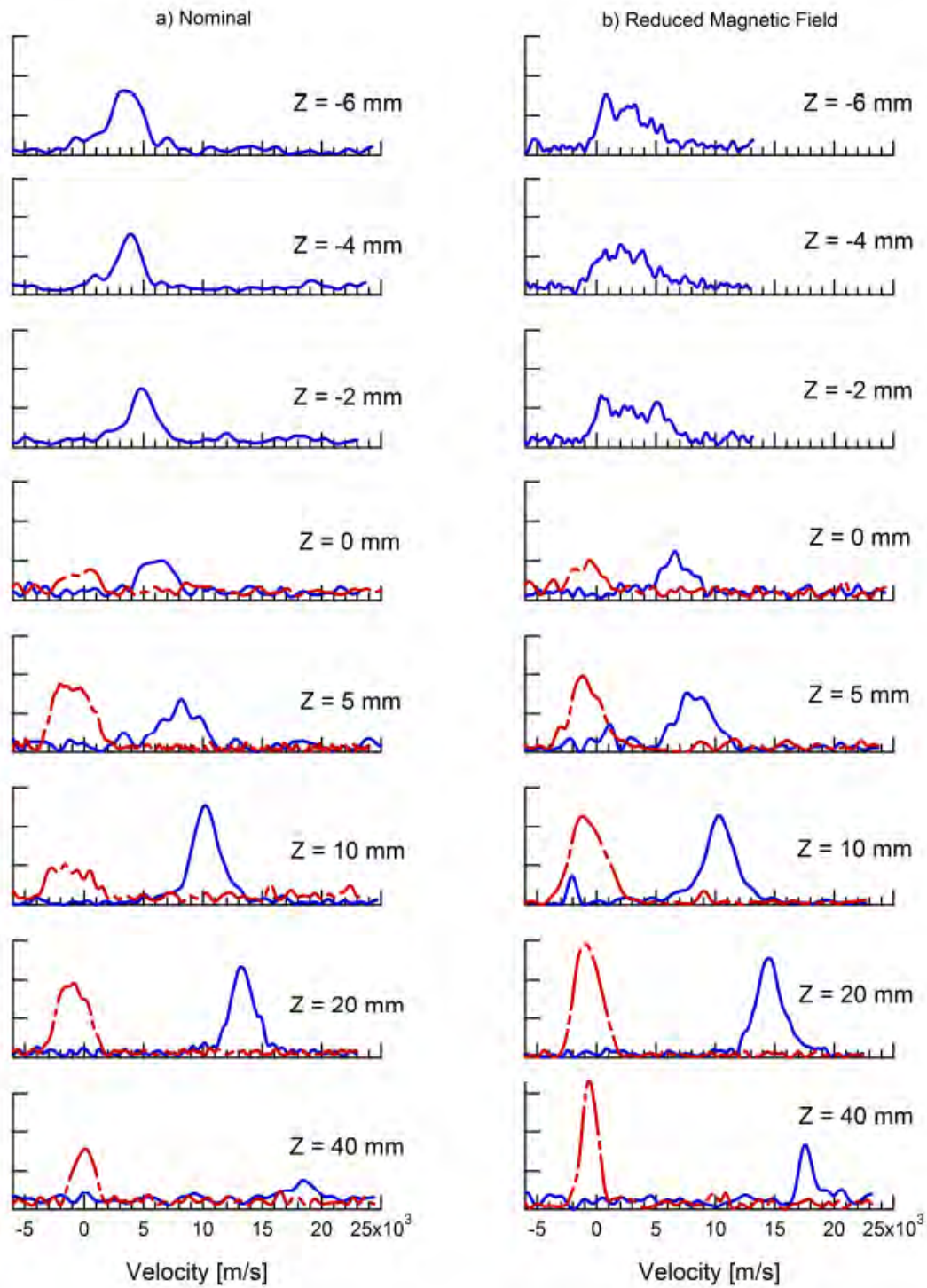


Figure S26. Centerline ion velocity distributions for the nominal and reduced magnetic field operating conditions. Red is the radial distribution, blue is the axial distribution. The distributions are area normalized.

trends in the data, and to calculate the electric field.

S2.3.2 Centerline Measurements

Centerline measurements are presented for positions of $Z = -6$ mm inside the thruster channel to $Z = 40$ mm into the plume, as shown in Figure S25. For the positions inside the channel, only axial measurements are shown, while both axial and radial measurements are shown for positions in the plume.

Figure S26 shows the evolution of the ion velocity distributions for the CHT-30 at a) nominal and b) reduced magnetic field conditions. The red, dashed lines represent the radial distributions, while the blue solid lines represent the axial distributions. In the axial direction, ion velocity distributions are shown both in the plume and at positions from $Z = -6$ mm to the exit plane within the thruster channel. For the nominal case, the distributions are relatively smooth and narrow, with 68% of the ions contained within less than a 4,000 m/s range (e.g. 2,900 m/s to 6,800 m/s for one standard deviation on each side of the median velocity at $Z = -2$ mm). For the reduced magnetic field condition, the axial ion velocity distributions are much broader inside the thruster, with less defined peaks giving ranges of approximately 5,000 m/s (e.g. 470 m/s to 5,500 m/s for one standard deviation from the median at $z = -2$ mm). Comparing the two, slight acceleration between $Z = -6$ mm and the exit plane can be seen in the nominal case, whereas it is less noticeable in the lower magnetic field case due to the broad distributions.

Referring back to Figure S20 which illustrates the cusped magnetic field profile inside a CHT, the magnetic field lines are believed to form equipotential surfaces, creating an electric field that has a significant axial component. This causes a convergent ion to keep ions away from the channel walls and accelerates the ions along the centerline. Therefore, it is intuitive that the nominal, higher magnetic field case would have more noticeable acceleration and concentrated velocity distribution inside the channel due to better ion confinement along the centerline. Overall, however, the most probable axial velocities achieved by the nominal and reduced magnetic field cases are the same within the uncertainty of the measurements, at 6,500 m/s. Outside the thruster channel, a significant portion of the axial ion acceleration is seen in the plume. For the nominal case, the ions achieve axial velocities between 16,000 m/s and 22,000 m/s at $Z = 40$ mm, with a relatively consistent acceleration from the exit plane through to the far field of the plume. For the reduced magnetic field case, the axial ion velocity distributions narrow and have a more pronounced peak as the ions progress further into the plume.

Figure S27 depicts the most probable axial ion velocities along the centerline of the thruster from $Z = -6$ mm inside the thruster channel to $Z = 40$ mm into the plume. This figure

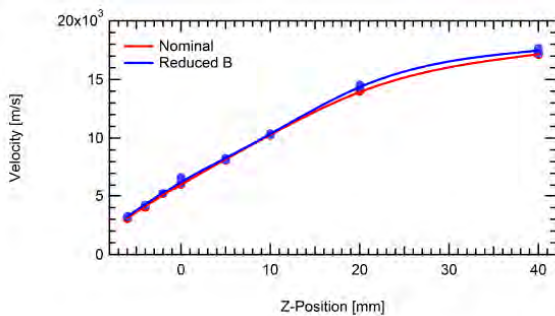


Figure S27. Most probable axial velocities along centerline of thruster plume for nominal and reduced magnetic field conditions.

shows that the reduced magnetic field case has a slightly higher most probable axial ion velocity from $Z = 10$ mm to $Z = 40$ mm, with the nominal case reaching 17,200 m/s and the reduced magnetic field case reaching 17,700 m/s at $Z = 40$ mm. For both conditions, the radial velocity distribution remains relatively constant along the centerline of the thruster, centered near 0 m/s. Previous calculations show that the most probable radial velocities vary from zero by no more than 1,200 m/s. For both

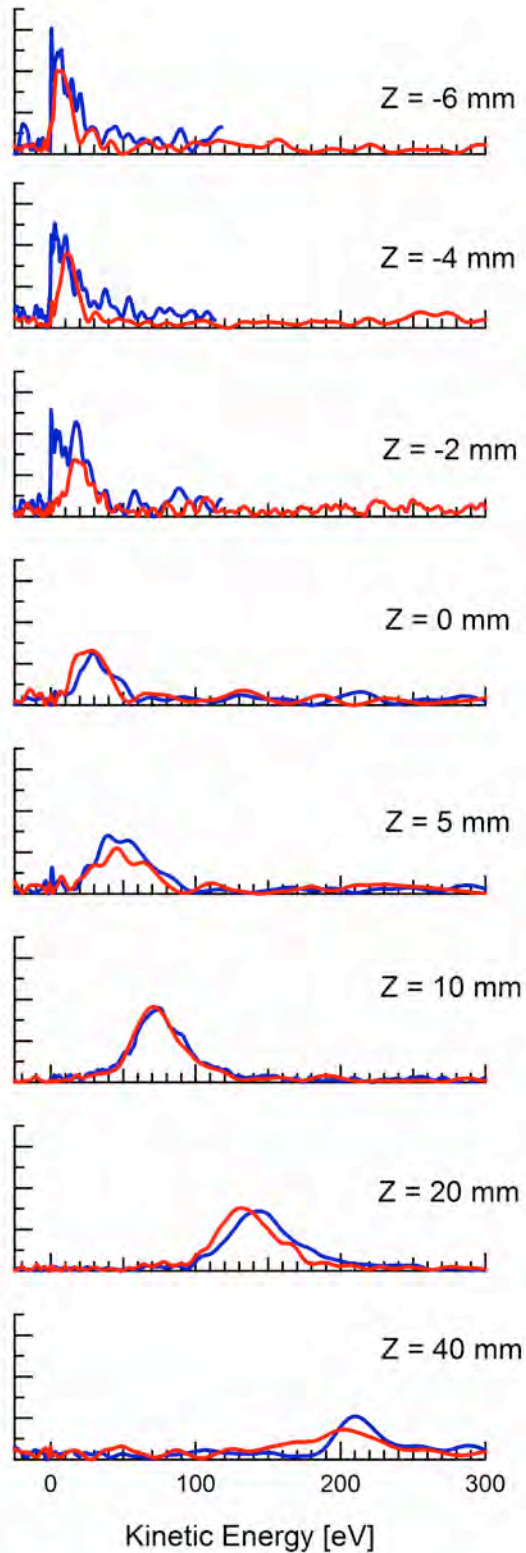


Figure S28. Centerline ion kinetic energy distributions for the nominal operating condition in red and reduced magnetic field operating condition in blue. The distributions are area normalized.

conditions, the radial ion velocities tend to have wider distributions at locations close to the exit plane of the thruster as compared to the points farther into the plume. This could be indicative of the strongly curved magnetic field profile seen in cusped-field thrusters that produces a wide distribution of velocity classes near the exit plane. This effect diminishes in strength farther downstream, due to the reduced influence of the radial component of electric field farther from the exit plane. Alternatively, the field strength may be strong enough to produce Zeeman broadening. However, by comparing the two operating conditions, it is noticeable that the reduced magnetic field case tends to have wider radial ion velocity distributions, but sharper peaks in the axial velocity than the nominal case indicating that while Zeeman broadening may be present, it is not the dominant broadening mechanism. Near the exit plane of the thruster, the wide radial distributions in the lower magnetic field case could be a function of the ions with slower axial velocities being pulled more effectively in the radial direction by the strong radial component of electric field. Similar to the axial velocity distributions, a stronger magnetic field seems to produce less variation in radial velocities.

Figure S28 shows the ion kinetic energy distributions at the centerline of the thruster channel for the nominal (red) and reduced magnetic field (blue) conditions. Previous studies on the CHT showed that the majority of the xenon propellant is ionized at the border of the annular and cylindrical region inside the CHT-30. The ion acceleration then occurs in the cylindrical region of the channel, along which the greatest potential drop occurs. However, comparing the centerline kinetic energies achieved by the exit plane of the thruster channel to those achieved outside shows that a large portion of the axial acceleration actually occurs in the thruster plume, at positions further than $Z = 5$ mm.

Throughout the plume, the width of the kinetic energy distributions remains similar for

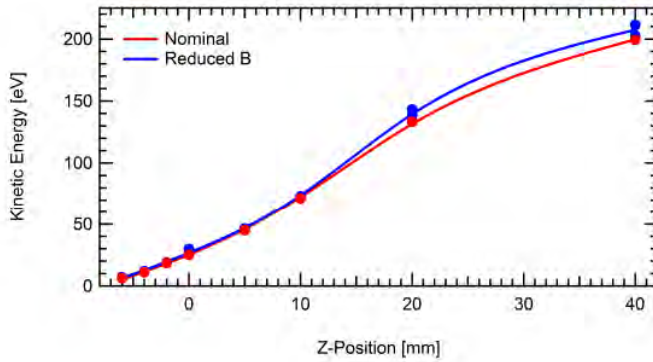


Figure S29. Most probable axial kinetic energies along centerline of plume for nominal and reduced magnetic field conditions.

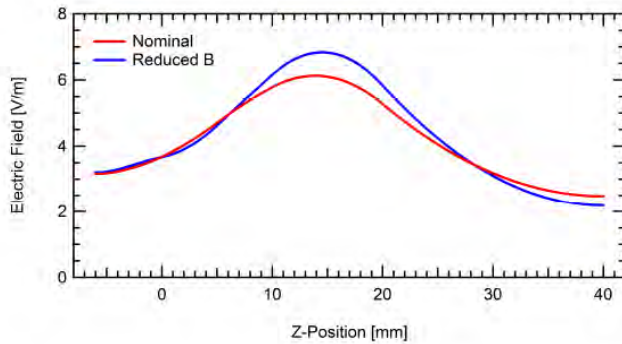


Figure S30. Centerline axial electric fields derived from most probable kinetic energies for nominal and reduced magnetic field conditions.

both operating conditions. However, at $Z = 40$ mm, the distribution for the nominal condition becomes much wider than that of the reduced magnetic field case (i.e. the full-width at half maximum (FWHM) is 25 eV for the reduced magnetic field case, and 50 eV for the nominal case). The wings of the energy distributions, however, when measured by one standard deviation on either side of the median kinetic energy value give a range of 177 eV to 228 eV for the nominal case, and 191 eV to 270 eV for the reduced magnetic field case - a wider range of higher energy ions for the reduced magnetic field case. The reason the range over which the reduced magnetic field kinetic energies is wider in terms of percentage of ions is that while the peak in the kinetic energy distribution is sharper for this condition, the wings are much shallower, favoring the higher energy side of the distribution. The reduced magnetic field condition appears to accelerate the ions more effectively at

locations farther into the plume.

Figure S29 shows the most probable axial kinetic energies along the centerline of the plume. The most probable value for both the nominal and reduced magnetic field kinetic energy is approximately 25 eV at the exit plane of the thruster, with an additional 175 eV to 188 eV gain in the plume. At a position 40 mm into the plume, this constitutes an energy of 200 eV for the nominal case and 213 eV for the reduced magnetic field case for an applied potential of 300 V. This confirms that the acceleration is primarily outside the thruster channel.

Figure S30 shows the axial electric field along the centerline of the thruster, derived from the most probable kinetic energy values. Comparing the electric fields makes the differences in acceleration seen in the velocity and kinetic energy distributions more clear. The reduced magnetic field case has a noticeably higher axial electric field around $Z = 10$ mm to 20 mm, allowing the ions to gain more energy in this region as compared to the nominal condition.

S2.3.3 Ion Velocity Distributions

Figure S31 shows the progression of ion velocity distributions across the exit plane of the thruster channel. Both the nominal and reduced magnetic field conditions behave similarly across the exit plane. The axial velocities slowly decrease across the width of the channel

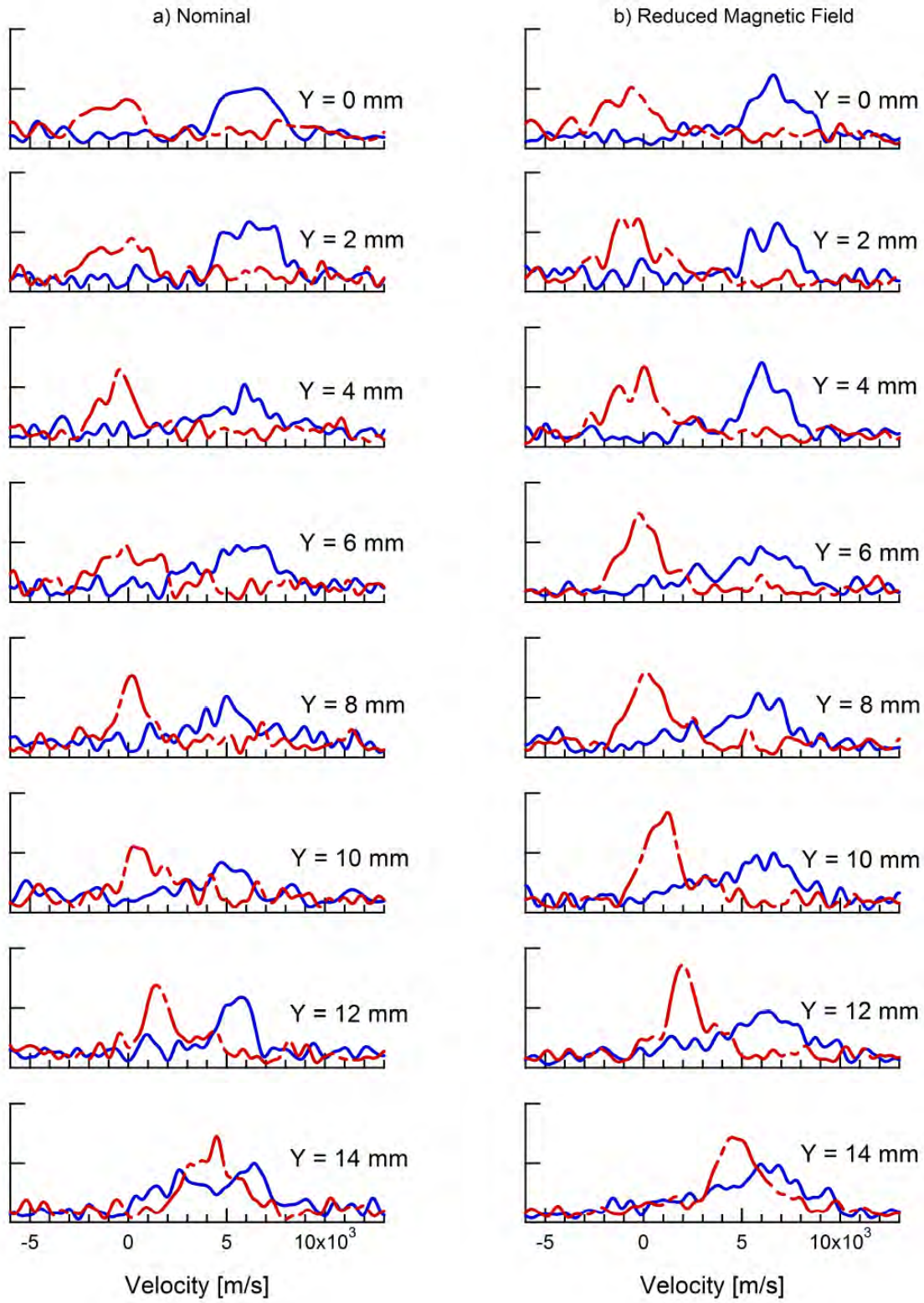


Figure S31. Exit plane ion velocity distributions for the nominal and reduced magnetic field operating conditions. Red is the radial distribution, blue is the axial distribution. The distributions are area normalized.

towards $Y = 14$ mm. The axial distributions broaden at positions away from the centerline, indicating a wider range of ion velocities, including a lower velocity tail in the distribution. For example, the nominal condition at $Y = 0$ mm has a median axial velocity of 5,960 m/s, with wings spanning 3,160 m/s to 7,870 m/s for 68% of the ions. At $Y = 14$ mm, the median axial velocity is slower at 4,630 m/s, with a wider span of 1,850 m/s to 8,640 m/s. The reduced magnetic field case loses slightly less axial velocity, starting at 6,600 m/s at $Y = 0$ mm and decreasing to 5,860 m/s at the channel wall. For both cases, this could be

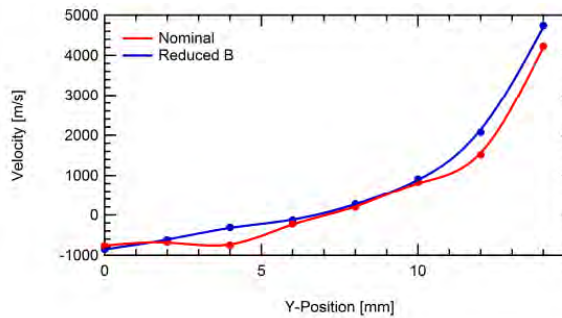


Figure S32. Most probable radial velocities along exit plane of thruster for nominal and reduced magnetic field conditions.

reminiscent of the convergent ion flux inside the thruster channel previously described by Smirnov, et al., [S14] where the more energetic ions are kept away from channel walls. Moving across the exit plane, the ions increase in radial velocity towards the channel wall. Starting at the centerline, the radial component of ion velocity is nearly zero for both operating conditions. But at a position of $Y = 14$ mm, the radial velocities become comparable in magnitude to the axial velocities.

Figure S32 gives the most probable values, 4,360 m/s for the nominal condition (compared to 4,630 m/s in the axial direction) and 4,870 m/s for the reduced magnetic field condition (compared to 5,860 m/s in the axial direction). This high radial component of ion velocity at the exit plane is indicative

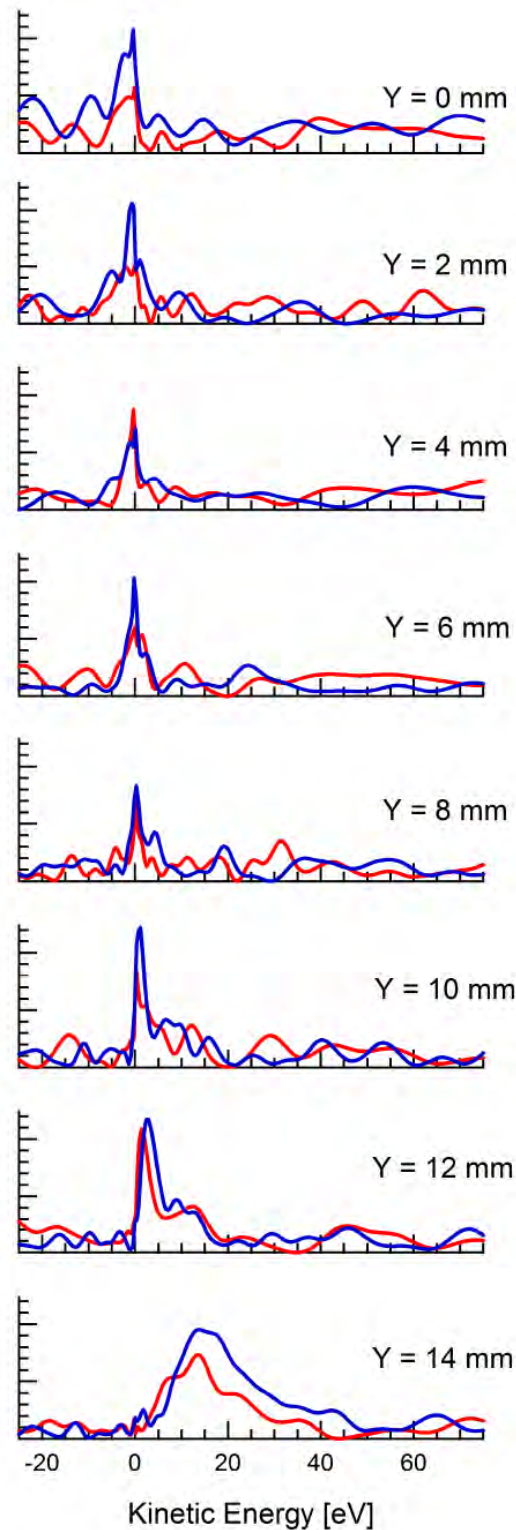


Figure S33. Most probable radial kinetic energy distributions along exit plane of thruster for nominal and reduced magnetic field conditions.

of the large plume divergence half angle that is typical of cylindrical Hall thrusters, but is very different than traditional annular Hall thrusters where the exit plane axial component of velocity is much higher than the radial. Also of note in Figure S32 is that the most probable radial velocities at $Y = 0$ mm are negative values. Besides the 500 m/s uncertainty, there are several contributing factors that may cause these velocities to be non-zero. These include the possibility that the centerline thruster is slightly misaligned, or more likely that the cathode being on one side of the thruster makes the plume slightly asymmetric.

S3.2.4. Ion Kinetic Energy Distributions

Figure S33 shows the radial kinetic energy distributions across the exit plane of the thruster. For both operating conditions, between positions of $Y = 0$ mm and $Y = 12$ mm, the peaks in the distributions are centered very close to 0 eV. Towards the channel wall, however, the tails of the distributions begin to stretch towards higher radial energies. The most probable radial kinetic energies are summarized in Figure 23. At $Y = 14$ mm, the most probable radial kinetic energy is 12 eV for the nominal case and 14 eV for the reduced magnetic field case. Adding these values to the nominal axial kinetic energies, 15 eV for the nominal case and 23 eV for the reduced magnetic field case at $Y = 14$ mm, shows that there is actually a gain in energy towards the channel wall at the exit plane. Both conditions start at approximately 25 eV at $Y = 0$ mm. The nominal condition increases to 26 eV at the channel wall, and the reduced magnetic field case increases to 37 eV. Overall, while there appears to be a convergent ion flux inside the thruster channel, the kinetic energy distributions at the exit plane indicate that the ions are very divergent just outside the channel.

Figure S34 shows the radial electric field profile across the exit plane of the thruster, calculated from the most probable values of radial kinetic energy. Previous studies have shown the half angle of the plume to be as large as 60° to 80° , compared to traditional annular Hall thrusters which have plume divergence half angles of approximately 45° to 50° [4]. This increased divergence angle could be due to the radial component of the electric field in this region being stronger than that of a traditional annular Hall thruster. This can be explained by the evolution of the magnetic field profile as it gets farther from the centerline of the channel. The resulting equipotential surfaces provide an electric field profile with a significant outward pointing radial component. From the exit plane outwards into the plume, all radial velocity components are therefore pointing away from the centerline. This plays a large role in the divergence of the plume, thereby reducing or eliminating the centerline ion flux seen inside the channel, resulting in a reduced mixing zone compared to annular Hall thrusters.

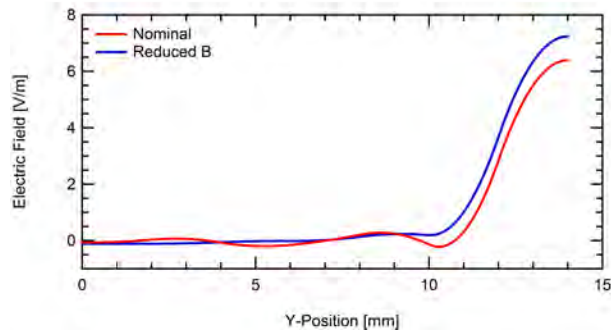


Figure S 34. Exit plane radial electric fields derived from kinetic energies for nominal and reduced magnetic field conditions.

Task Stanford-3. Electrostatic Probe Characterization of Wave Dispersion and Turbulence (Ongoing).

In addition to time-average ion transport properties obtained by LIF, we had also proposed studying the dynamical plasma behavior (fluctuations) within the channel and in the near-field of these thrusters. The goal was to use passively-biased Langmuir probes (triple probe for in-plane wave propagation determination) in ion collection mode impedance-matched and amplified for high bandwidth sensitivity and gain. These measurements were motivated by the desire to understand the possible role (if any) played by low and high frequency instabilities on electron transport.

Because the SCFT does not appear to have significant plasma fluctuations in comparison to the DCF-T, and because we did not have access to a DCFT in the first year of the grant, these measurements were carried out on an existing laboratory Hall thruster. In this Hall thruster, we expected MHz-level azimuthally propagating waves associated with the two-stream ion-electron instabilities, which have been postulated to account for cross-field electron transport at modest levels, i.e., 1eV in potential fluctuations. A question arose as to the existence and possible significance of such fluctuations in the cusped-field thrusters, since the strong magnetic fields will also likely trap electrons and prevent electron migration towards the anode. During the second year of the grant, the student involved in these measurements graduated and was not replaced. While measurements were obtained on the Hall thruster, they were not yet implemented in the MIT DCF-T, and so this portion of the task is incomplete and is not discussed here.

Task Stanford-4. Measurements of Plasma Potential and Plasma Temperature (Completed)

The potential distribution in the CCFT was extensively characterized using a floating emissive probe. The procedure for acquiring the potential measurements involves first mapping an unheated (floating) potential, with care taken to rapidly move the probe in and out of regions of strong heating so that it does not become self-emitting. Generally, this involves moving in and out along the axis, for varying radial positions. A 2D translation stage on which the thruster was mounted allowed for translational speeds of approximately 5 cm/s. After the floating potential measurements were completed, the probe was heated causing it to become self-emitting and the measurements were repeated to obtain the plasma potential, using usual theories, considering effects on ion collection associated with magnetic fields. The facility at Stanford is capable of time-resolving the probe signals, allowing the recreation of dominant temporal features in phase with low-frequency breathing oscillations, although this particular thruster did not exhibit strong oscillations. Time did not permit similar measurements on the DCF. The measurements obtained on the CCFT are summarized later in this report.

S4.1. Probe Measurements on CCFT with Krypton Propellant

The CCFT thruster underwent extensive diagnostic testing with a nude Faraday probe. The ion collecting area was 0.97 cm^2 , and both the probe collector and guard ring were biased to -20 V for electron repulsion. Krypton propellant was used, with a flow rate of 8.2 sccm , and a discharge potential and current of 300 V , and 0.361 A , respectively. During the Faraday probe testing, the cathode was mounted to the thruster, and both were mounted on a rotating translation stage with the axis of rotation positioned orthogonal to the intersection of the main thruster axis with the exit plane. The cathode was fixed at an axial distance of 2.8 cm ($\pm 1 \text{ mm}$) and a radial distance of 3.85 cm ($\pm 1 \text{ mm}$). The probe remained stationary, oriented along the central axis of the thruster at a distance of 20.5 cm from the exit plane. The collected ion current density as a function of angular position relative to the central axis of the discharge is shown in Fig. S35 (the current density profile is fitted with a spline which is forced through zero at $\pm 90^\circ$).

The DCF thruster plume appears to be conically shaped with two main wings of high current density located at an average angle of 34° (as measured from the central axis), with a small swell in current density located along the thruster axis. This discharge profile qualitatively matches the one obtained by MIT [S3]. The cathode is shown to have a significant effect on the plume, decreasing the width, angular position, and magnitude of the conical wing nearest to it.

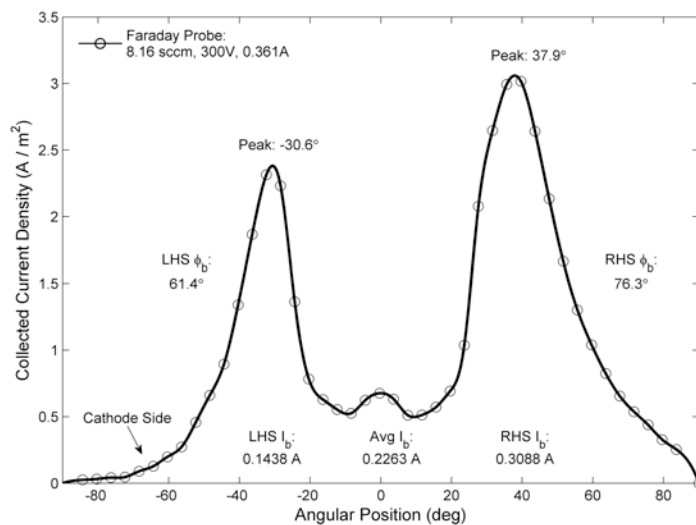


Figure S35. Ion current density collected over a sweep of the DCF thruster discharge. The spline fit is forced through zero at $\pm 90^\circ$. I_b represents the integrated beam current over the entire plume. ϕ_b is the angle corresponding to 95% of I_b for each half of the ion profile.

Further investigation is required to observe how widespread this effect is transmitted around the conical discharge, and the extent to which the ion current density in the plume is axisymmetric.

The beam currents (I_b) indicated on the diagram are calculated by assuming an axisymmetric plume and performing a stepwise volume-of-revolution numerical integration of the calculated spline fit according to:

$$I_b = 2\pi R \int_0^{\pi/2} j(\phi) \sin(\phi) d\phi$$

where R is the distance from the thruster exit plane to the Faraday probe, j is the collected current density, and ϕ is the angular position relative to the thruster axis. Averaging the independent calculations from each wing yields an integrated beam current of 0.23 A, and thus an average beam efficiency (I_b/I_a) of 62.7%. The divergence angle of the observed plasma plume is estimated in two ways: calculating the angles of the maximum collected ion current and those encompassing 95% of the total beam current in each wing. The angles of maximum ion current are calculated to be 30.6° and 37.9° respectively for the cathode and opposite side, while the 95% beam currents are found to be respectively 61.4° and 76.3° (an almost 20% reduction in divergence angle due to the presence of the cathode). It is clear from Fig. S35 that the cathode certainly has a large effect on all of these plume characteristics.

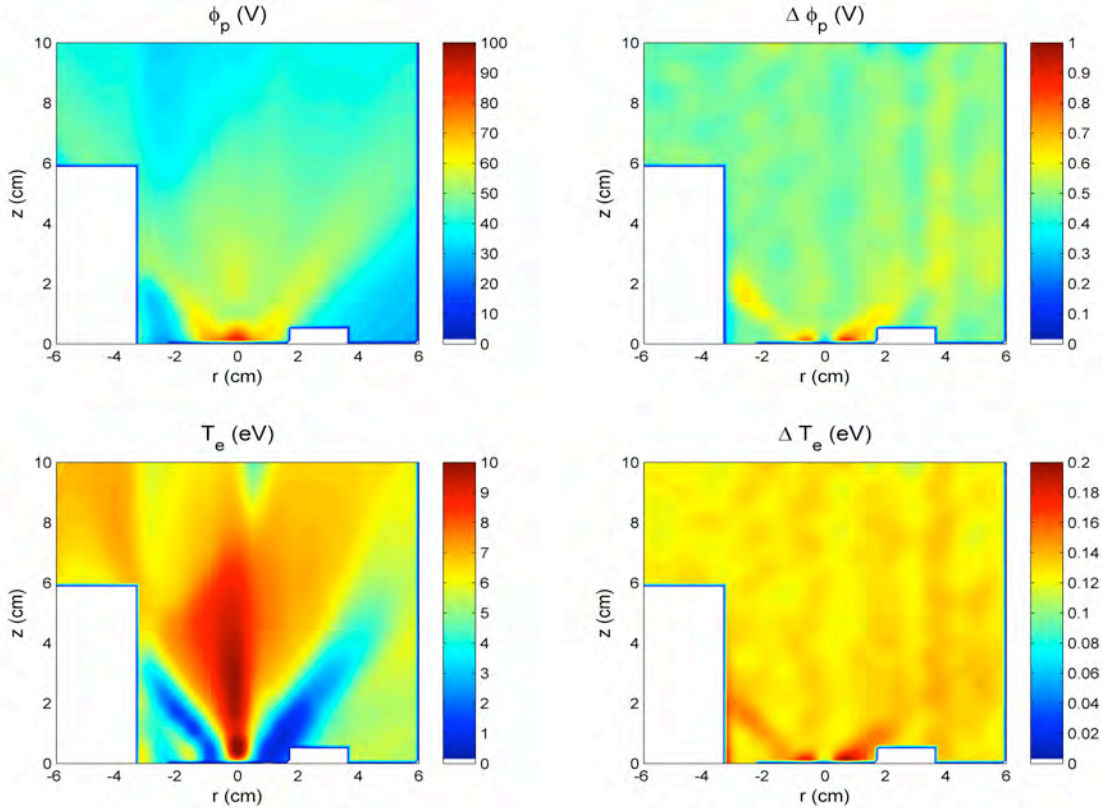


Figure S36. Floating plasma potential measurement and electron temperature calculation, with fluctuations (standard deviations), of the DCF thruster plume obtained with an emissive probe. The origin (0,0) is the intersection of the main thruster axis with the exit plane.

A study was also carried out with the emissive probe to measure the plasma potential (ϕ_p) and electron temperature (T_e) throughout a horizontal plane passing through the center of the thruster exit plane and cathode. The thruster was kept in voltage-limited mode at 300 V, drawing an average of 0.354 A with a flow rate of 8.2 sccm of krypton. The cathode was fixed at an axial distance of 2.83 cm (± 1 mm) and radial distance of 3.0 cm (± 1 mm). Probe data was not taken where the cathode was located, or very near a protruding bolt on the exterior face of the thruster. The panels of Fig. S36 show the resulting spatial map in the plasma potential (top left) as well as the fluctuation (standard deviation) in the plasma potential (top right) arising as a result of the high frequency (~ 100 kHz) fluctuations seen in the hot probe potential. The plasma potential reaches a maximum of 100 V along the central axis near the exit plane (at $r = 0$ cm and $z = 0.2$ cm). The potential along the axis passes through a depression near 50 V at $z = 1.0$ cm, before increasing to more than 60 V at $z = 2$ cm and gradually diminishing to below 40 V at $z = 6$ cm. A distinct feature of the plasma potential measurement in this thruster is the relatively high potential region coinciding with the conical emission seen in photographs and the two peaks in the ion current trace (Fig. S35). The potential in these “wing” regions, can be as high as 70 V falling to less than 50 V at larger radial positions. We note that the conical wing regions very near the exit plane are also a source of high frequency fluctuations, as apparent in the panel at top right; however, the standard deviation in this fluctuation is generally less than about 1 V.

The observed plasma potential and cold-probe floating potential (not shown) is used to determine the electron temperature in the near-field (see bottom-left panel in Fig. S36). The conical plume, generally of high plasma potential, appears to be a region low in electron temperature. Also apparent is the presence of a large jet of high electron temperature plasma that is ejected throughout the interior region of the plume. This region of elevated electron temperature along the thruster axis is concomitant with the region of increased plasma potential near the centerline. The lower right panel of Fig. S36 depicts fluctuations (standard deviation) in electron temperature computed from the measured fluctuations in hot and cold probe signals. The magnitude of the maximum fluctuations in plasma potential and electron temperature are $\sim 1\%$ and $\sim 2\%$ of the mean (time-averaged) values, respectively within the measurement domain.

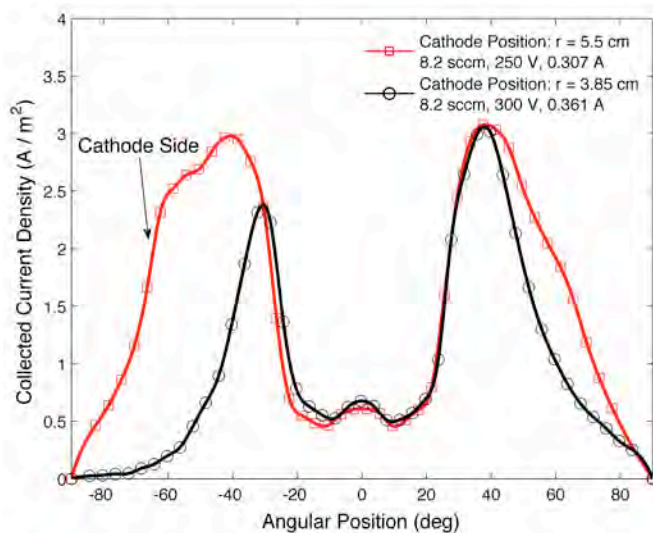


Figure S37. Two ion current density profiles at differing radial cathode locations. The influence of the cathode is clearly seen on the left side of the discharge.

measurement domain.

In addition to the operating conditions and performance data mentioned previously, the DCF thruster exhibited numerous irreproducible operating modes that resulted in both unusually high and low thrust efficiencies. One notable high-current mode (which has, as yet, been elusive to reproduction) resulted in anode efficiencies well above 30% in an operating range of 160 W to 180 W at the 8.2 sccm, 300 V point used continuously throughout our testing. Further investigation is ongoing to recreate the operating conditions of this mode. In addition, unusually low

anode efficiency values were obtained especially at a cathode radial location of 5.5 cm. The explanation for the poor performance at this location (still irreproducible after early tests) is the subject of current research. An example of this phenomenon is demonstrated in the ion current densities of Fig. S37; one might assume from the ion profiles that the point at $r = 5.5$ cm is more efficient, yielding more ion current. Yet, it is in fact the opposite. Because of uncharacteristically low thrust, the 5.5 cm point has a very low specific impulse (I_{sp}) of 440 s, compared to the 980 s of the 3.85 cm point, making the latter point much more efficient. These data, taken for a range of operating points during this relatively poor mode of thruster operation demonstrates the “squeezing” effect that the cathode imposes on the discharge plume. We note that the center and far wing of the $r = 3.85$ cm discharge matches very well with the $r = 5.5$ cm trace where the cathode is farther away, yet the closer wing is vastly reduced in both extent and total beam current. This result suggests that the cathode placement and overall electron emission efficiency may be a very influential means of tuning the divergence and intensity of the plasma plume.

S4.2. Probe Measurements on CCFT with Xenon Propellant

Emissive probe measurements were also carried out on the CCFT operating on xenon – the more common propellant used in space propulsion applications. The emitting portion of the probe consists of a 2 mm diameter loop of 150 μm diameter thoriated-tungsten (1%) wire, connected to copper wire encased in a 2.5 mm diameter alumina tube. 2.5 A of direct current is driven through the probe to heat the thoriated-tungsten filament until its signal is saturated, at which point the probe filament is floating at the potential of the surrounding plasma.

Figure S38 shows the emissive probe measurements of the plasma potential, for both operating conditions. Probe data was taken in a horizontal plane passing through the center of the thruster exit plane and cathode, excluding area occupied by the cathode and a bolt on the exterior face of the thruster. For the power matched condition, the maximum plasma potential measured in the plume was 37 V at the edges of the discharge channel wall near the exit plane of the thruster ($Z = 0$ mm, $R = \pm 10$ mm). By 20 mm into the plume, the plasma potential drops to around 20 V, except for a conical jet of higher potential at an angle of 35°

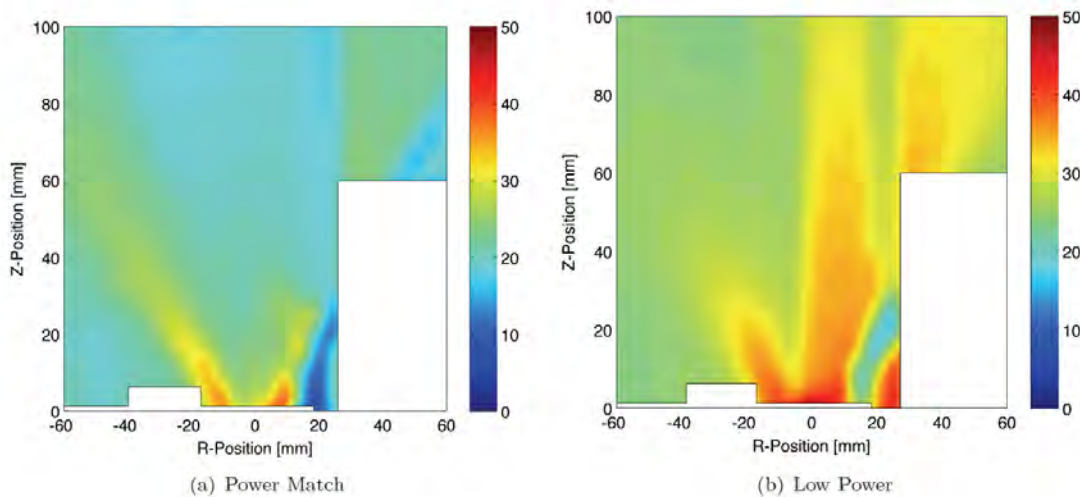


Figure S38. Plasma potential measurements in the near-field DCF thruster plume operating under (a) power matched, and (b) low power operating conditions.

with respect to the outward normal from the exit plane which remains as high as 30 V by 20 mm into the plume. The jet is asymmetric, being interrupted on the cathode side by a region of lower potential (~ 10 V). The region of elevated plasma potential corresponds visually with the luminous conical jet seen in photographs. When operating on krypton, this region also correlated with the highest ion current density.

For the low power condition, the maximum plasma potential measured was higher than the power matched condition (described in S3 above): 46 V at the exit plane of the thruster along the centerline ($Z = 0$ mm, $R = 0$ mm). The potential profile also displays a somewhat conical shape in the regions of higher potential; however, the potential also remains elevated throughout the center of the cone (upwards of 35 V on the cathode side). Once again, this corresponds to the distribution of luminous regions observed throughout the conical plume. Of note when comparing the two operating conditions, the power matched case has a larger potential drop inside the thruster channel (300 V to less than 50 V at the exit plane), whereas the low power case has a potential drop that is more distributed throughout the plume (only 150 V to 60 V at the exit plane). With the bulk of the plume remaining at a 25 to 35 V plasma potential, the low power condition appears to be less efficient at converting applied anode potential to ion acceleration. Figure S39 gives a close-up of the plasma potential measurements, including points inside the discharge channel, with overlaid contours of the axial kinetic energy profiles derived from LIF measurements of axial ion velocity. Radial LIF measurements were not taken in this experiment; therefore, the kinetic energy contours should not be taken as an overall magnitude. For the power matched condition, Figure S39(a) shows that there is a large drop in potential between $Z = -6$ mm inside the thruster channel

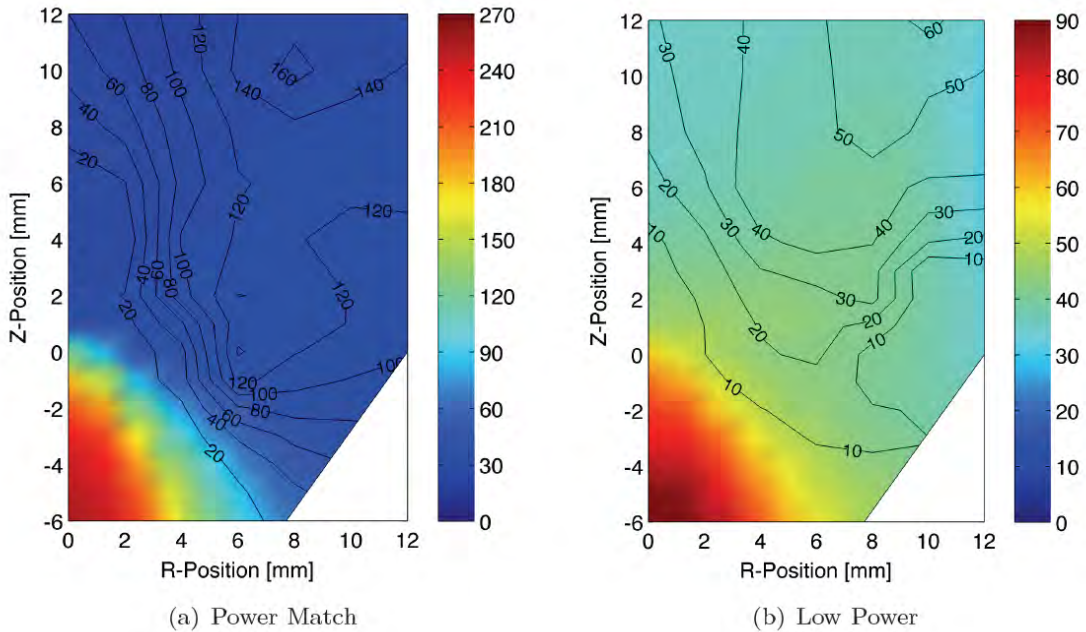


Figure S39. Close up of plasma potential with kinetic energy contour overlay for the DCF thruster plume operating under (a) power matched, and (b) low power operating conditions.

and the exit plane at radii less than $R = 7$ mm (i.e. the radius at the edge of the cylindrical portion of the thruster channel). The border between high and low potential follows a portion of the kinetic energy contour that delimits ~ 20 eV ions. However, this 20 eV region extend 8

mm into the plume, while the potential drop appears contained within the thruster. The plasma potential remains relatively constant 30 V outside the thruster. This appears not to match the gradient seen in the kinetic energy contours, where ions gain energy from 20 eV to 160 eV by 12 mm into the plume.

Qualitatively, the low power plasma potential map seen in Figure S39(b) is very similar to the power match condition, exhibiting a large potential drop just inside the thruster exit plane followed by relatively constant potential out to 12 mm. The potential drop inside the thruster is less severe for the low power condition, only decreasing from 90 V to 40 V, compared to the 230 V drop seen in the power matched condition. Again, the lowest kinetic energy contour (this time 10 eV) more closely matches the potential drop, however the gain in axial kinetic energy outside the exit plane is unmatched by any further potential drop.

Figure S40 shows the plasma potential and ion kinetic energies along the centerline of the thruster for both the power matched and low power operating conditions. This figure better illuminates the differences between the LIF measurements described earlier, and the probe

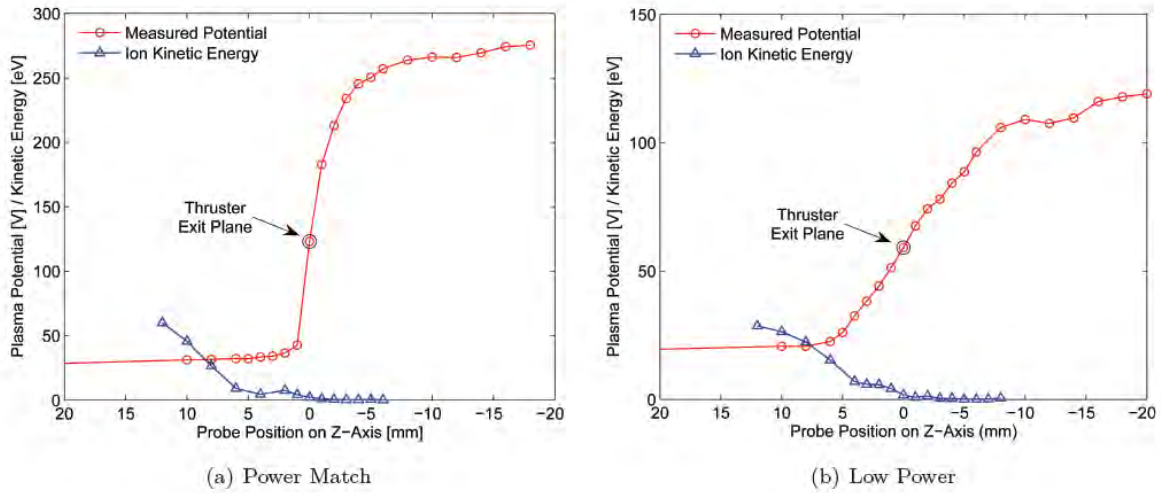


Figure S40. Plasma potential and axial ion kinetic energy measurements along the centerline of the DCF thruster operating under (a) power matched, and (b) low power operating conditions.

measurements, as well as those between the two operating conditions. The sharp potential drop seen near the exit plane for the power match condition is more gradual for the low power case. For both conditions, the majority of the gain in axial ion kinetic energy does not occur until approximately 5 mm outside of the thruster, at which point the plasma potential has already flattened out to a nearly constant value. (The differences between the plasma potential maps and LIF derived kinetic energies could have several causes. As mentioned above, the difference in background pressure at the two facilities could slightly shift the regions of ion acceleration corresponding to the drop in potential. The SPPL chamber background pressure was approximately twice that of the AFRL chamber, likely resulting in the potential drop and peak ion acceleration being pushed upstream. Also, emissive probes are inherently intrusive by nature, with the potential to alter the operation of the thruster, especially when taking measurements inside the thruster channel. Therefore, when comparing measurements from the different facilities, differences should be expected, especially near the exit plane of the thruster.

Task Stanford-5. Kinetic Simulations (Completed).

Understanding the electron dynamics in these cusped-field thrusters is a primary component of the Stanford research. The Stanford team carried out preliminary simulations using electron kinetic (particle) tracking with the prescribed magnetic and (measured) electric fields. This provided us with a window into the particle dynamics, including electron-scattering (from walls and heavy particles) and B-field mirroring, which we expected to see in regions very near the anode, and in the wall cusped regions, where the B-fields converged. For a prescribed static magnetic and electric field distribution (provided by experiments, e.g., see Task Stanford-4), high-fidelity time-integrating methods were utilized to track electrons launched from a simulated cathode. Electron collisions were not included in the simulations carried out so far, although the effect of secondary ionization on transport through the birth of electrons at locations other than the cathode was studied. Including momentum scattering and ionization collisions in the DCF/CHT configuration is the subject of continuing research.

S5.1 Electron Trajectory Simulations

In both Hall thrusters, as well as in these families of cusped-field thrusters, electrons released from the external cathode may either service the discharge in the channel / near field or depart with ejected ions in the plume, maintaining charge neutrality. Electrons remaining near the thruster approach the channel on indirect paths, impeded by the magnetic field structure and collisions with the other species. Certain collisions between electrons and neutral propellant atoms produce propellant ions that are ejected into the plume by the primarily axial electric field, generating thrust. Secondary electrons “born” through ionization events may also travel to the anode, ionize a different propellant atom (“avalanche ionization”), or migrate out into the plume. Specific details of electron transport from the cathode to the anode, including ionization, remain an active area of research; these processes directly correlate with thruster performance and are integral in our understanding of these devices.

The overarching goal of these simulations is to further characterize the physics of the

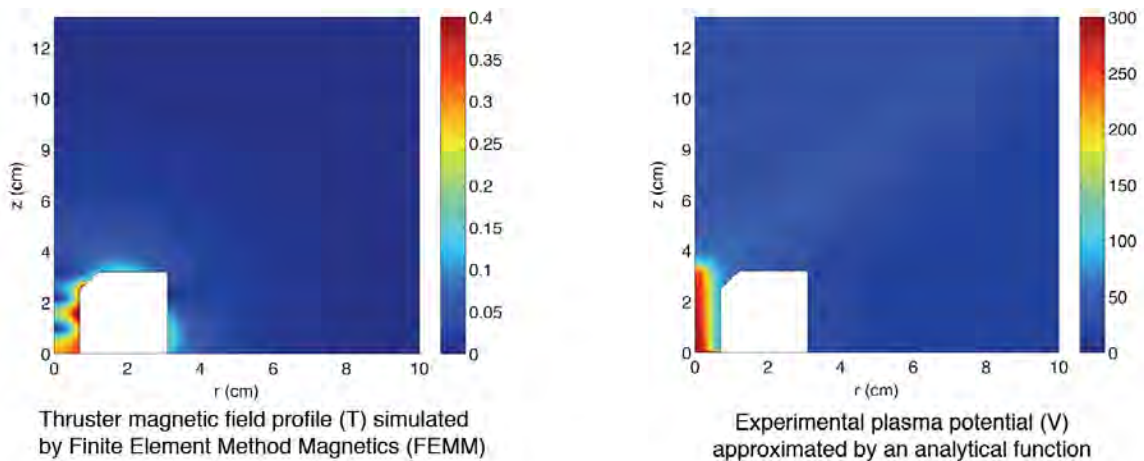


Figure 41. Left: simulated magnetic field in the vicinity of the exit and in the outer channel region. Right: measured plasma potential. These results are used in the kinetic simulations.

cathode-thruster circuit, including identifying probable regions of propellant ionization, by numerically simulating test electron trajectories throughout the thruster domain.

The kinetic simulations use the Buneman leapfrog numerical method and solve the equations of motion at any discrete point in the domain. Standard 2D interpolation schemes solve for the electric field (given the measured plasma potential described above) and the simulated magnetic field. A modified time step ensures single position advancement does not span more than one grid space (1 mm x 1 mm) or 1% of one cyclotron period.

The first simulations were conducted with the electron release at the experimental cathode location, with a distribution of energies that reflect the cathode temperature. The electrons are not allowed to collide with anything other than the wall, which assumed to have a sheath potential (15V) that can reflect some fraction of the incident electrons. Electrons with energies high enough to overcome the sheath repulsion scatter from the wall with random energy and velocities at the wall temperature. In all, 119 electrons were tracked for at most 10^6 spatial advancements. We found that the high magnetic field strengths force tight electron gyro-orbits that are expensive to compute for a relatively small advancement of the guiding center. All of the released electrons remained trapped in the domain (i.e. had not reached the anode or the far-field boundary) after each had completed these 10^6 position advancements. Clearly, the absence of collisions is a significant restriction on the transport and the majority of the electrons remain in the vicinity of the exit plane of the thruster and mirror off of the first cusp. The conclusions that can be drawn from these studies is straightforward – the non-uniform fields alone cannot account for direct transport from the cathode to the anode in this discharge. This result was somewhat expected, but perhaps not to this extent.

These first simulations prompted us to conclude that secondary electrons generated by volume ionization through inelastic electron – neutral collisions provide a birth of electrons in regions of the exit plane/channel that more readily allow electrons to reach the anode. To better understand this possibility, we have carried out simulations where we release electrons at various points within the domain in order to mimic their “birth” as a result of ionization. In these simulations, the electrons are born with zero energy (zero velocity). In the simulations

carried out so far, we have released over 7500 electrons, equally throughout the domain and track the final location to as much as 10^6 position advancements.

Figure 42 shows the results of these simulations. The color coding in the figure represents the fate of electrons released at that location. Blue indicates that electrons released (or “born”) at that location end up in the plume. Red indicates that electrons born at this location end up reaching the anode. White represents electrons that are trapped in the domain for the duration of the simulation. We see from this figure that secondary electron production, or scattering must take place along the axis

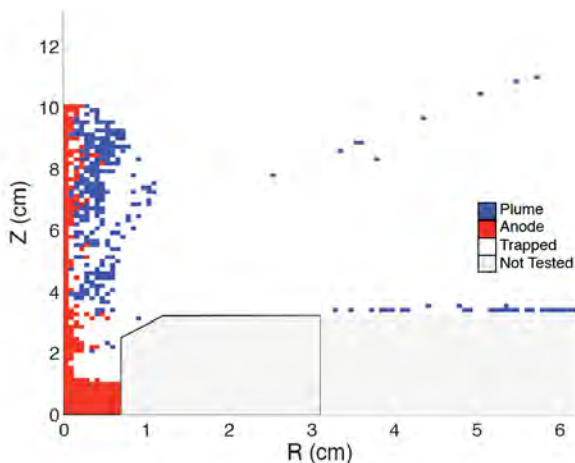


Figure 42. Mapping of location of released electrons and their fate. Blue indicates released electrons that end up in the plume, whereas red are locations of released electrons that reach the anode.

(or very near the anode) for an electron to eventually reach the anode. Secondaries or scattering taking place off-axis (blue) results in electrons reaching the upper domain (plume). Anode transport therefore requires a scattering event of some sort (momentum transfer or ionization), very near the axial regions of the channel.

Simulations were also carried out to determine the sensitivity in the transport of primary electrons into the channel based on the cathode location. The findings are consistent with the first simulations described, that unless the cathode is located very near the axis, primaries cannot reach the anode directly, and must undergo scattering or produce low energy secondaries very close to the axis. Ongoing simulations include studying the impact that high frequency, high phase velocity potential fluctuations may have on primary and secondary electron transport within the divergent cusped field channels.

References

- [S1] Y. Raitses and N.J. Fisch, "Parametric investigations of a nonconventional Hall thruster. *Physics of Plasmas* 8, 2579 - 2586, 2001.
- [S2] D.G. Courtney, M. Martinez-Sanchez, "Diverging cusped-field Hall thruster," *Proceedings of the 30th International Electric Propulsion Conference. IEPC-2007-39-2007*.
- [S3] D.G. Courtney, "Development and characterization of a diverging cusped field thruster and a lanthanum hexaboride hollow cathode," M.Sc. Thesis, Massachusetts Institute of Technology, 2008.
- [S4] J.E. Hansen and W. Persson, "Revised analysis of singly ionized xenon, Xe II," *Physica Scripta* 4, 602–643, 1987.
- [S5] L. Brostrom, A. Kastberg, J. Lidberg, and S. Mannervik, "Hyperfine-structure measurements in Xe II." *Physical Review A*, 53, 109–112, 1996.
- [S6] W.A. Hargus Jr., and M.A. Cappelli, "Laser-induced fluorescence measurements of velocity within a Hall discharge," *Applied Physics B* 72, 961–969, 2001.
- [S7] H. Geisen, T. Krumpelmann, D. Neuschafer, and C Ottinger, "Hyperfine splitting measurements on the 6265 Angstrom and 6507 Angstrom lines of seven Xe isotopes by LIF on a beam of metastable Xe(3P0,3) atoms," *Physics Letters A*, 130, 299–309, 1988.
- [S8] W. Fischer, H. Huhnermann, G. Kromer, and H.J. Schafer, "Isotope shifts in the atomic spectrum of xenon and nuclear deformation effects," *Z. Physik* 270, 113–120, 1974.
- [S9] D.H. Manzella, "Stationary plasma thruster ion velocity distribution," *Proceedings of the 30th Joint Propulsion Conference and Exhibit, AIAA-1994-3141*, 1994.
- [S10] W.A.Hargus Jr., M.R. Nakles, "Ion velocity measurements within the acceleration channel of low- power Hall thruster," *IEEE Transactions on Plasma Science* 36(5):1989–1997, 2008.
- [S11] S. Mazouffre, D. Gawron, V. Kulaev, and N. Sadehgi, "Xe+ ion transport in the crossed-field discharge of a 5-kW-class Hall effect thruster, " *IEEE Transactions on Plasma Science* 36, 1967–1976, 2008.
- [S12] N.A. MacDonald, M.A. Cappelli, and W.A. Hargus Jr., "Laser-induced fluorescence velocity measurements of a low power cylindrical Hall thruster," *Proceedings of the 31st International Electric Propulsion Conference*, 2009.
- [S13] C.V. Young, A.W. Smith, and M.A. Cappelli, "Preliminary characterization of a diverging cusped field (DCF) thruster, *Proceedings of the 31st International Electric Propulsion Conference, IEPC-2009-166*, 2009.
- [S14] A. Smirnov, Y. Raitses and N.J. Fisch, "The effect of magnetic field on the performance of low-power cylindrical Hall thrusters, *Proceedings of the 29th International Electric Propulsion Conference, IEPC-2005-099*, 2005.

Detailed Report on Tasks MT1 to MT4

Rather than following the original Task breakdown for MT1 to MT4 this portion of the report is organized by investigated topics, in an attempt to follow the logical thread as our understanding of the complex issues gradually developed from the various tests and calculations. It is to be emphasized that our level of understanding at the start of the project was truly deficient, despite the successful operation of the original thruster. We had conjectured for example that ionization might be concentrated in the first cusp region, near the anode; it is now thought to be concentrated near the exit plane, in the vicinity of the last separatrix. We had expected a strong effect of the partial ion magnetization near the cusps; it was later shown that ion confinement is almost fully electrostatic, in sharp potential structures set up by the magnetically confined electrons. We had speculated that the hollow plume angle might be related to the wall divergence; later tests with the Stanford cylindrical variation have shown that the wall angle plays no role. Our Report will attempt to link the successive small discoveries and how they motivated other experiments and models. Our current level of understanding is still deficient in some regards, which we will document as well.

1. Design and fabrication of DCF test thrusters

The original DCFT [Ref 1] was improved upon to enable simpler and more robust electrical and flow connections to power and flow systems for testing, ease manufacturing and assembly efforts, and to address some problems noticed in early tests. A schematic representation of the DCFT design is shown in Figure 1. All the main parts and assemblies are shown in this figure, except for the neutral injection pathway. A detail of the anode assembly is provided in Figure 2, and the neutral injection is illustrated to scale in Figure 3. Not shown are the end cap used to hold the cone in place, the screws used to contain the magnets and core within the outer case, the mounting plates, and the assembly cylinder. Complete engineering drawings for the thrusters used in these studies were provided to the Edwards AFB AFRL machine shop and Space Propulsion Branch Micro-propulsion Research Group. Drawings of the original design are available in the Master's Thesis submitted by Dan Courtney to MIT in 2007 [Ref 5]. The list of all parts labeled in these figures is provided in Table 2, along with the materials and suppliers for each component.

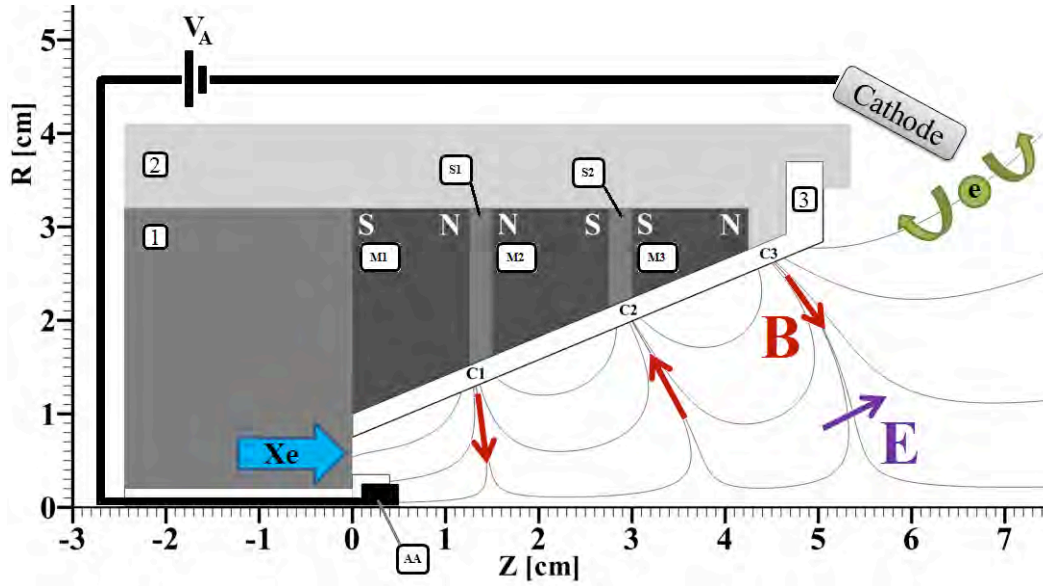


Figure 1: A scaled schematic of the DCFT. The injection of neutral propellant is not shown here.

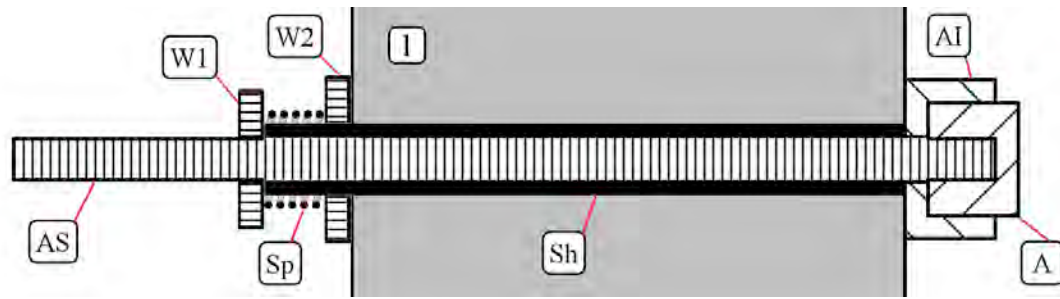


Figure 2: Anode assembly detail of redesign. The back end of the anode stem (AS) is threaded to allow compression of the anode spring (Sp), which holds the anode insulator (AI) flush with the base core (1). The anode stem and anode (A) are threaded, and mate as shown to hold the anode in place.

In the original design, the flow line and anode both accessed the main chamber using holes drilled on or near the thruster axis, through the base core. The flow path was modified to enter the core at an angle, as shown in Figure 3. This was done to eliminate any arcing between the anode connection and flow line, as well as to allow easier access to the anode electrical connection during thruster installation.

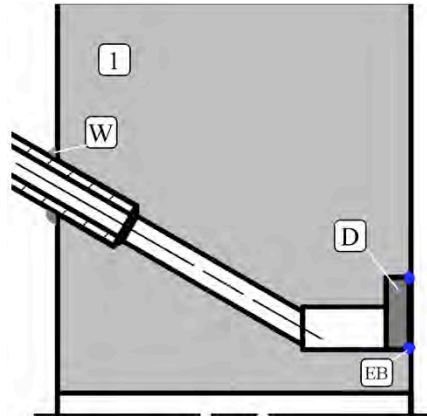


Figure 3: Neutral injection (NI) redesign, not shown in Figure 1. The diffuser disc (D) has 10 μm pores. The hole shown on axis is where the anode assembly fits through the base core (1), as shown in Figure 1.

Table 2: The parts labeled in Figures 1,2,3 and Ref [5] are named, with the supplier and material of each part provided.

Label	Part Name	Material	Supplier
1	Base core	1018 Steel	bulk material
2	Outer case	Aluminum	bulk material
3	Insulator Cone	HP-BN	St. Gobain/ Ferro-Ceramic Grinding Inc.
M1-M3	Permanent magnets	SmCo 3212	Dexter Magnetics
S1, S2	Magnet spacers	1018 Steel	bulk material
AA Anode Assembly			
A	Anode	AXF-5Q Poco graphite	bulk material
AI	Anode insulator	HP-BN	Eric's Machine Shop
Sh	Anode sheath	HP-BN	Eric's Machine Shop

AS	Anode stem	316 SS	Eric's Machine Shop
W1	Washer 1	HP-BN	Eric's Machine Shop
W2	Washer 2	HP-BN	Eric's Machine Shop
Sp	Assembly spring	316 SS	Lee Spring
<hr/>			
NI	Neutral Injector		
D	Diffuser	316 SS (porous)	Mott Corporation
EB	Electron beam weld	-	Electron Beam Engineering, Inc.
W	Tig weld	-	Electron Beam Engineering, Inc.
<hr/>			

A common problem that arose during tests of previous anode assembly designs was arcing between the anode stem and thruster body. In some cases, the arcs caused the anode sheath to fail. Also, in an effort to improve heat conduction away from the anode, BN was temporarily replaced with AlN as the insulator material. This decision was reversed when arcing events increased and often shorted the anode to the thruster body, necessitating the replacement of the failed parts. BN remains a superior choice of insulator because of its high dielectric strength, which is at least 20 times greater than for AlN. The anode assembly was then redesigned as shown in Figure 2, with much improved electrical isolation between the thruster body and anode stem provided by the anode sheath extending past the thickness of the core, and by washer #2, which prevents any shorts from developing that use the assembly spring as an intermediary. Additionally, to inhibit arcing caused by leaking neutral propellant, the welds shown in Figure 3 were included in the new design. The new design was used for Laser Induced Fluorescence and long-duration testing of the DCFT, where no troubles operating the thruster occurred for over 260 h of operation. Practical considerations for future designs of laboratory thrusters include the replacement of the 316 SS diffuser, part of the neutral injection system, with a porous ceramic. This would greatly reduce the deposition of sputtered steel on internal chamber surfaces, which was observed during the aforementioned tests.

For reference in the discussion of the following sections, we include here a standard magnetic map of the thruster, showing the location of the magnetic cusps and the multi-cell magnetic structure (Figure 4). Notice the existence of three distinct separatrices, which are the surfaces separating magnetic cells. At the intersection of each of these surfaces with the

axis of symmetry, the field is zero, and it reaches a local maximum, with alternating direction, at a location between these zeros. The magnitude of the field is plotted in Figure 5. Notice the high field intensity near the cusps and also near the anode.

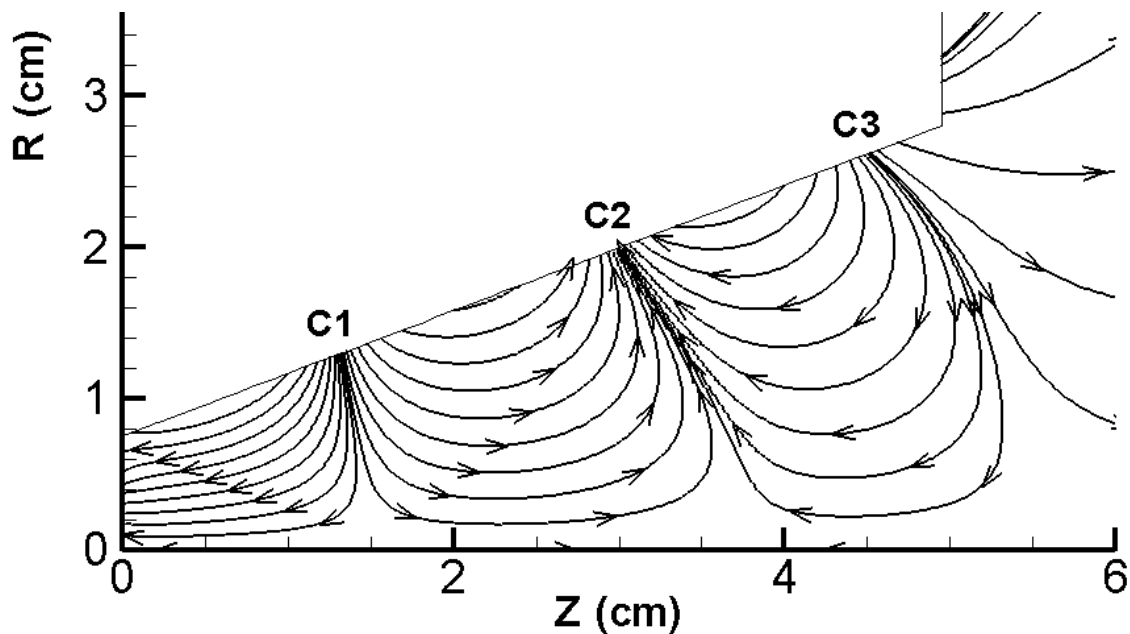


Figure 4: Representative field lines within the DCFT chamber. Field line density does not correspond to the magnitude of the field in this figure.

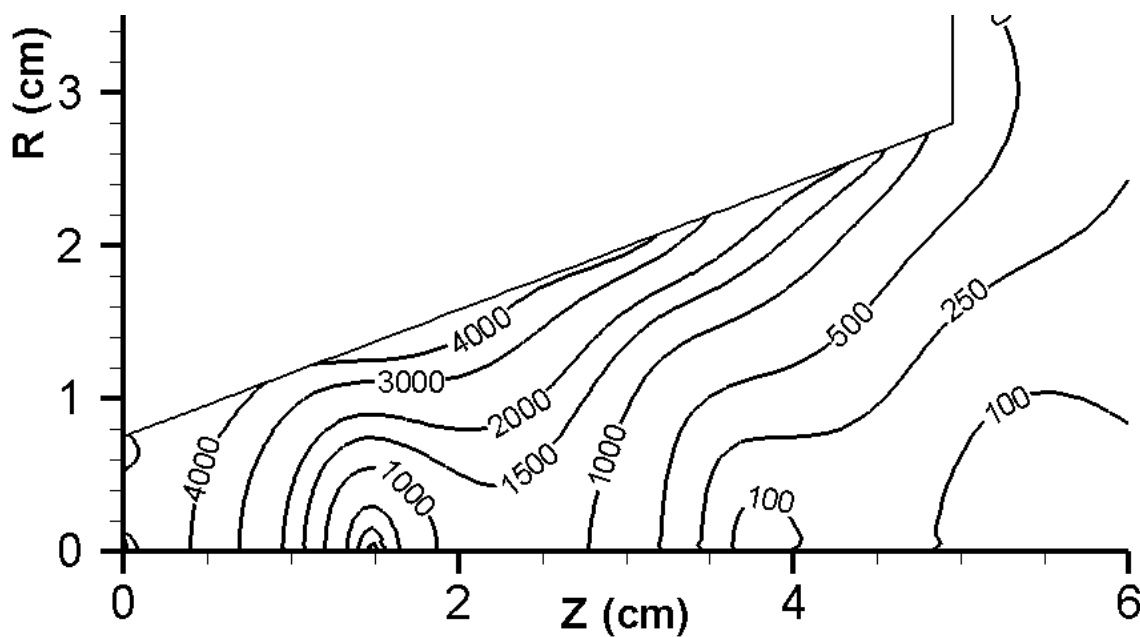


Figure 5: Magnetic field magnitude (Gauss) within the channel of the DCFT thruster.

With significant assistance from the Edwards AFB AFRL machine shop and the Micro-propulsion Group at the Space Propulsion Branch, enough parts to complete 4 thrusters were acquired and machined during the summer of 2009. One thruster went to the Stanford Plasma Physics Laboratory, one stayed at the AFRL, and two were brought back to MIT. Plans for sending one thruster to the Princeton group were delayed, but the thruster is still available for any continuation of the research there. The thrusters have provided a common test bed on which diverse sets of measurements have been acquired, all of which should complement one another. Tests run with these thrusters have contributed a large portion of the data presented in this report, demonstrating that this effort has had a positive impact on collaborative efforts between MIT, Stanford and the AFRL.

2. Exploration of anode position effects

The initial design of the DCFT was undertaken with consideration towards flexibility in assessing some of the major design parameters. The axial position of the anode within the discharge chamber and consequently the number and strength of cusps between anode and cathode is one such adjustable parameter which has significant consequences for any subsequent design iterations. A number of Boron Nitride spacers were inserted between the graphite anode cap and the upstream end of the discharge chamber in order to investigate these effects.

The collecting surface was moved 20 mm downstream of its nominal location, putting it within the 2nd downstream point cusp and likely eliminating any major effects of the first wall cusp on thruster performance. Simulations of the magnetic field using Ansoft's Maxwell SV predict for the outermost line that intersects the anode a mirror ratio of $R=2.7$ (3550 G/1320 G) at the nominal anode location and nearly double that, $R=3.7$ (1260 G/340 G), at its new location in the second point cusp. For the centerline, the mirror ratio is in both cases infinite.

Anode I-V curves in the new configuration show that the current increases on the order of 100% for the same mass flow rate, though no visual change in the plasma plume is observed. For example, an anode current of 1.1 A was obtained at 175 V and 8.5 sccm of xenon, a flow rate which corresponds to a maximum equivalent current of 0.61 A of singly charged ions (0.68 A when the cathode flow is included), compared to a nominal current of around 0.6 A.

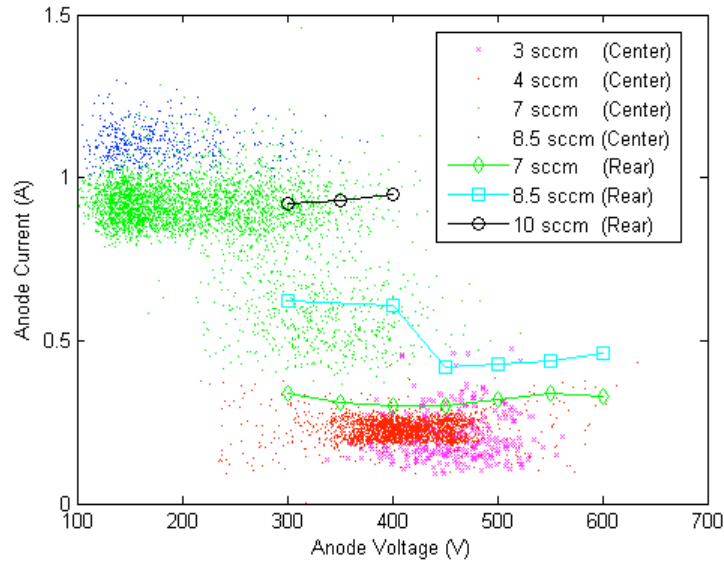


Figure 6. Anode I-V curves for both center (in reference to axial position) and rear-mounted anodes

Unfortunately, no probe measurements of the beam current in the 2-cusp mode have been made up to this point, however, simple estimates suggest the beam efficiency (beam current/anode current) is far less than in the nominal case. A beam current of 0.46 A is measured with the rear-mounted anode at 450 V and a flow rate of 8.5 sccm, resulting in a beam efficiency of 74%. In the exceedingly optimistic case of full ionization of the incoming flow with 20% doubly charged ions, the beam current would still only be 0.71 A leading to a beam efficiency of 65% in the centrally-mounted anode configuration. It seems likely then that the addition of the third cusp acts to throttle the back-streaming electron current and increase the efficiency of the thruster, barring any decrease in the efficiency of ion acceleration or ion production. However a more thorough experimental campaign would be necessary to affirm any such conclusion.

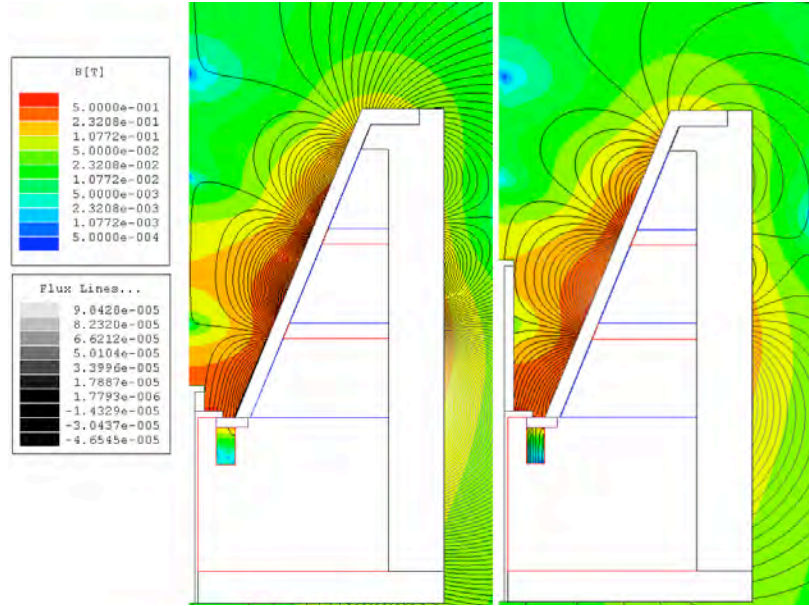


Figure 7. Maxwell SV simulations of the magnetic field for the center (right) and rear-mounted (left) anodes, showing in both cases the anode resides at a point cusp

Measurements of the AC component of the anode current were also made which revealed an increase in the fundamental frequency of current oscillations in the centrally-mounted anode case. The normal peak-to-peak frequency of the large amplitude fluctuations observed in high current mode operation at 8.5 sccm are measured to be 3.6-4 kHz, while the centrally-mounted anode case results in a frequency of 8.3 kHz. The normal anode position is about 44.5 mm from the exit of the discharge chamber, so by re-positioning it 20 mm downstream the time for an average neutral particle to stream from anode to exit is roughly cut in half. The doubling of the fundamental frequency observed with the halving of the refill time lends support to the idea of the anode current waveform being a form of relaxation oscillation.

This work is unpublished, but was discussed in the MIT presentation at the 2009 AFOSR Contractors Meeting.

4. Internal surface probing

The work in this section was presented in Refs.[6,7], where additional details can be found. A custom-machined version of the 5-cm long, Boron Nitride (BN) shell which insulates the conical discharge chamber was fabricated with 18 through-holes at various axial and azimuthal locations for the insertion of flush-mounted Langmuir probes. The purpose of the internal probe study is to examine the efficacy of the thruster design in limiting erosion by ion impact.

The relatively large area of the insulating Boron Nitride cone allows for the integration of a large number of flush-mounted probes, which when sized to allow the application of thin-sheath probe theory are still small enough to limit perturbations to device operation and maximize spatial resolution. Determination of the plasma characteristics by the probes is

obscured, however, by the strong magnetic fields of $\sim 1\text{-}5\text{kG}$ at the discharge chamber walls, with widely varying angles of incidence.

Probe theory for magnetized plasmas has been derived in many forms, with much of the literature dedicated to flush-mounted applications along the walls of fusion devices [Refs. 8-11]. Several of these theories are based on equating the electron flux along a magnetic flux tube towards a probe with the perpendicular electron flux into that tube by either classical or anomalous diffusion. The theories consider geometries where electrons diffuse towards the probe along field lines normal to its surface with constant magnetic field strength everywhere. This parallel diffusion is accommodated solely by perpendicular diffusion into the flux tube, which is driven by a density gradient pointing from the collection area out to the surrounding bulk plasma. Correspondingly the electron current collected by the probe decreases compared to the un-magnetized case. The various theories appear to diverge in their characterization of the I-V curve for a magnetized electron population, but it is widely accepted that the normal, un-magnetized probe theory may be applied for probe biases below the floating potential.

In our case the probe collection can be split into two fairly different regimes. In and around the cusps the field is nearly perpendicular to the probe face and connects to the bulk plasma in the center of the chamber. In contrast, the probes between cusps intersect the field lines at highly oblique angles and are accessible only to electrons which have diffused from the bulk across the strong perpendicular magnetic field.

Anode Voltage	410 V
Anode Current	330 mA
Anode Flow Rate	0.68 mg/s Xe
Cathode Flow Rate	98 $\mu\text{g/s}$ Xe
Keeper Current	0.5 A

Table 1. Thruster operational conditions during internal probe experiment
The thruster was operating in LC mode.

Results show strong localization of the ion flux at the magnetic cusps, where the field is nearly perpendicular to the chamber surface. Collected ion current drops by two to three orders of magnitude at locations where the field line is more than 12° from the wall normal direction .

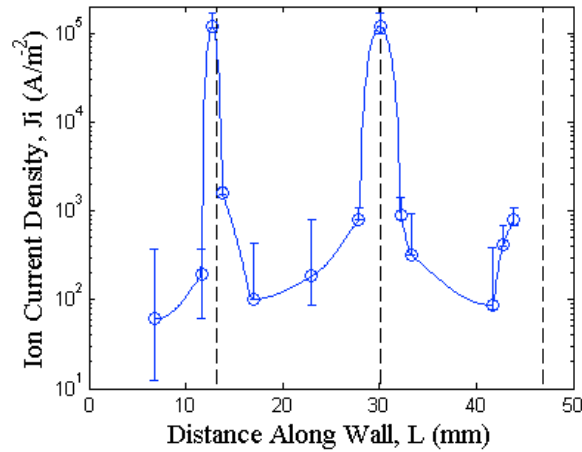


Figure 8. Measured ion current density vs. probe distance from rear wall at nominal conditions. Dashed lines indicate approximate wall cusp positions.

The intense localization of the ion flux to the walls near the cusps is expected in a simple sense from the insulating boundary condition. Electron flux to the walls between cusps is limited by cross-field diffusion across a strong magnetic field, and since no current is collected by the walls the ion flux is limited as well. Experiments on various devices and models verify the observed channeling of ions towards the cusp, with the kinetic model described in this report predicting similar confinement for both un-magnetized and fully magnetized ions.

Fitting a Gaussian curve to the ion current density profiles at each of the cusps gives loss widths of 1.1-mm at the furthest upstream cusp and 1.6-mm at the second cusp. The ion loss width is taken as the full width at half maximum of the fit and is commonly found to be roughly equal to the hybrid gyrodiameter, [12,13]. Hybrid gyrodiameters of 0.8 and 1.6-mm would correspond to perpendicular ion energies of 1 and 14-eV respectively at each of the two upstream cusps, based on the electron temperatures measured there.

The total ion current lost to the walls at each upstream cusp is also estimated by integrating over the Gaussian fits, yielding currents of 8 and 24-A. An ion current of 8 A to the wall would correspond to a power loss around 220 W, compared to the available 135 W, under modest estimates. The curve fits are not expected to be highly accurate due to the sparseness of the data set. Assuming a cusp width equal to the probe diameter gives a current of 2-A in the first cusp alone, corresponding to a power loss of at least 55 W.

A large dip in electron temperature was found near the two resolved cusps, with temperatures reaching as low as 3.5 eV. The temperatures found between cusps, ranging from around 10-20 eV, are more indicative of the temperatures required for efficient ionization. The error bars shown in electron temperature plot reflect the effect changes in selection of ion current have on the slope of the derived electron current near the floating potential.

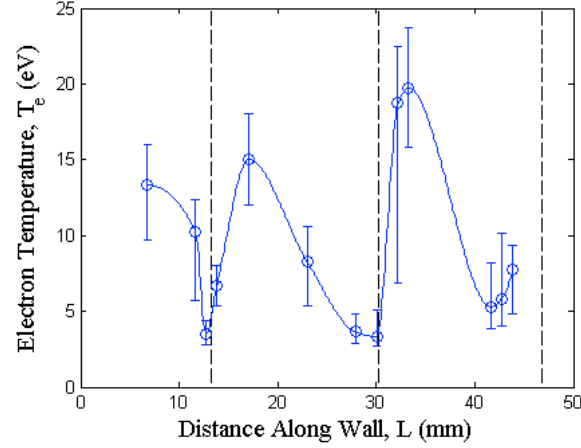


Figure 9. Electron temperature vs. probe distance from rear wall at nominal conditions. Dashed lines indicate approximate wall cusp positions.

The measured values of ion current and electron temperature are used to extract information on the electron density profile. The densities shown are generally higher than those predicted by the fully kinetic PIC simulation described below by one to two orders of magnitude.

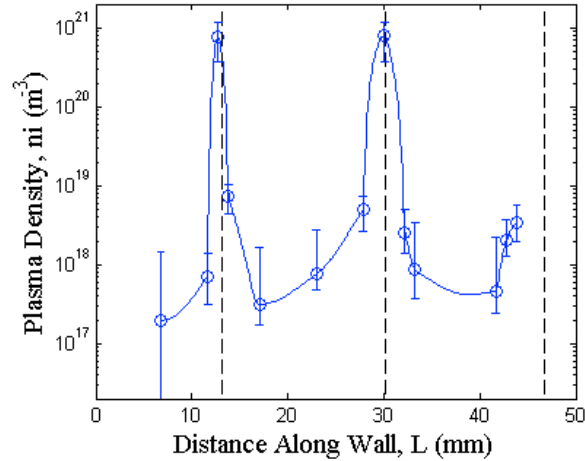


Figure 10. Electron density vs. probe distance from rear wall at nominal conditions. Dashed lines indicate approximate wall cusp positions.

The plasma potential is estimated both by using a combination of floating potential and temperature measurements and by finding the root of the second derivative of the I-V curve (generally referred to as the Druyvesteyn method). The results of both methods give potentials less than half of the applied voltage, in stark contrast with typical internal probe results in Hall thrusters where the full anode potential is measured by flush probes upstream of the acceleration region. We also observe the formation of strong potential valleys in the cusps, as expected from theoretical considerations of a stationary plasma. The steep potential gradients on either side of the cusp act to channel the ions into the region where the electrons are magnetically confined.

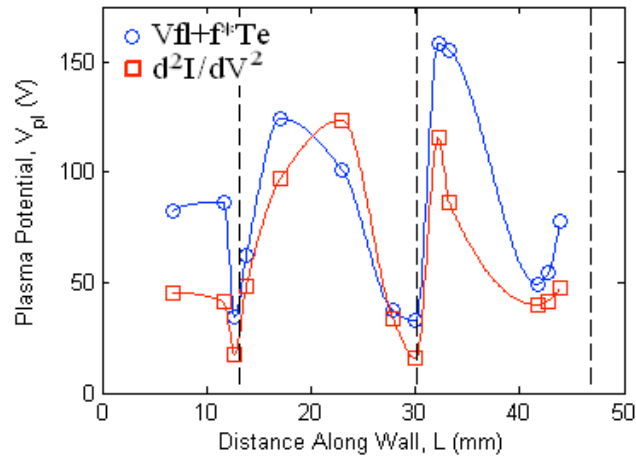


Figure 11. Plasma potential determined by two methods vs. probe distance from rear wall at nominal conditions. Dashed lines indicate approximate wall cusp positions.

The multiple cusp, magnetic field topology of the DCFT obfuscates interpretation of the probe data. In the simplest sense, each probe collects from a flux tube which terminates on two very distinct regions of the thruster. Several pairs of probes (13-18 and 14-17 in particular) appear to collect from nearly identical flux tubes, but yield different results for temperature and potential. Generally, the probe data are considered as an average of the plasma parameters over each collecting flux tube, but for probes near the cusps, where collisions may no longer be negligible, and near the exit, where ions may have gained significant directed motion, the precise region being sampled is not obvious.

The probe data show higher ion densities in the cusp than expected and lower potentials everywhere. Some of the error in ion current density can be attributed to uncertainty in the collecting area. The values shown here use the nominal cross-sectional area of the tungsten wire, but images obtained post-experiment with a scanning electron microscope show considerable deviation from a flat collecting face in several of the probes. The diameter of the tungsten wire used was also smaller than the holes drilled through the BN wall by 0.1-mm. If the area of the probe holes is taken as the collecting area the values given here for current and number density are halved.

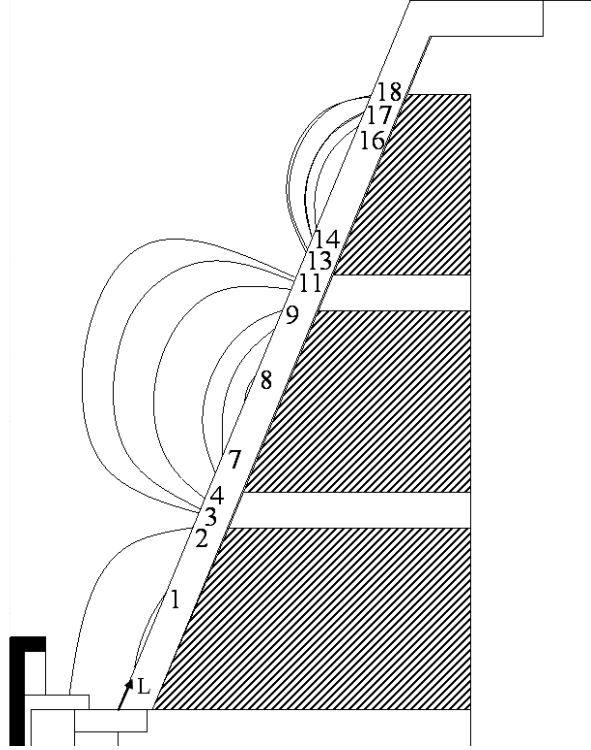


Figure 12. Simulated Magnetic Flux Lines which connect to flush probes are shown. Probe numbers are given at approximate position where flux tube terminates on probe surface. Malfunctioning probes not pictured.

Certain probes also exhibit a white aureola after testing, similar in coloration to the cusp region where ion bombardment is at its highest. Only probe 1 displayed a significant halo effect after the testing described here, however much larger aureolas developed during recent, more extensive testing and are shown in Figure 13. It is clear from the size of the aureolas that the probes are perturbing a region much larger than the probe diameter.

In an attempt to quantify the extent of ion collection area expansion, two estimates of the plasma density made using the electron current are compared to densities obtained from ion saturation. The Druyvesteyn method described elsewhere [Demidov et al., Rev. of Sc. Instr. 73 (3409), 2002] uses the second derivative of the I-V curve to find the electron energy distribution function (EEDF), which when integrated over all energies gives the electron density. The second method involved linearly extrapolating the electron saturation current from the $\ln(I_e)$ vs. V_p curve to the plasma potential and using it to estimate density.



Figure 13. Photograph of 5 probes furthest downstream after recent testing. A white ring is visible in the middle is the second cusp. Large aureolas can be seen around four of the probes.

We can estimate an effective ion collection area-to-probe area ratio by dividing the density found using the ion saturation current and probe area with the density found from either of the two methods described above assuming these new values are more representative of the actual plasma density in the device. The results of this simple model show that the same trend in effective ion collection area is obtained with either method. The effective area appears to peak near cusps with collection diameters of around 3-mm in these regions. These diameters seem somewhat feasible, at least, when compared to the aureola diameters of around 1-5 mm which developed after longer duration testing. When the ion flux is corrected by the EEDF obtained area ratio we find total currents of 60-mA in the first cusp and 220-mA in the second.

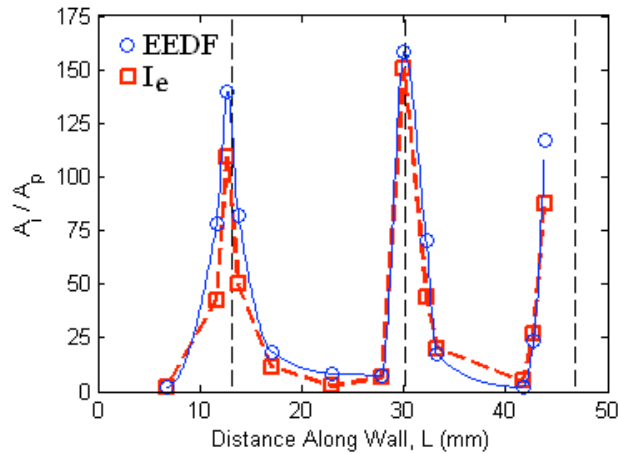


Figure 14. Effective ion collection area to probe area fraction determined by two methods vs. probe distance from rear wall at nominal conditions. Dashed lines indicate cusp positions

Both of the methods used for collection area estimates rely on accurate values for the plasma potential and on the assumption of minimal distortion of the electron current by the magnetic

field. The Druyvesteyn method is particularly difficult to apply at the cusps, where electron saturation cannot be measured due to limits on the current collectable by the Keithley 6517 used in the experiments. At these points the second derivative curve is linearly extrapolated down to zero. In either case the estimate of an effective collection area is not intended as conclusive evidence that such a phenomena is actually at work, but rather more as an illustration of the discrepancies that occur when simple probe theories are applied to the data.

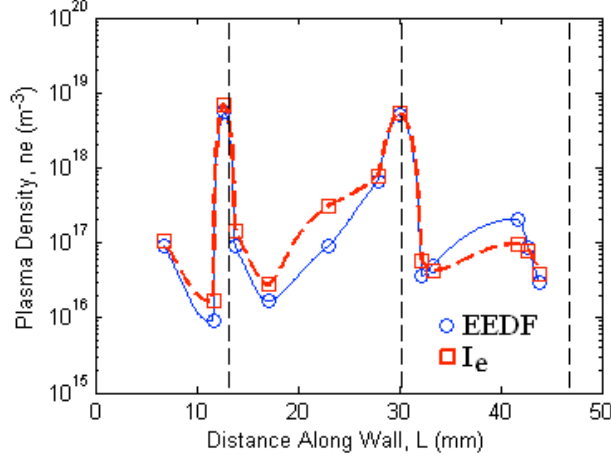


Figure 15. Electron density determined by two methods vs. probe distance from rear wall at nominal conditions. Dashed lines indicate cusp positions

Ultimately, though the data qualitatively match predictions, they are quantitatively inconsistent. The reasons behind the surprisingly high ion densities and low plasma potentials measured are as yet unclear, though they may be connected to unexpectedly large perturbations to the plasma by the probes. Further testing is planned which attempts to remove some of the systematic errors perceived to affect the experiments described here, and which will be necessary to verify the results.

5. Cusp kinetic theory

In an effort to clarify the physics on the electron and ion confinement in the cusp areas of DCF-like thrusters, ideal, collisionless kinetic theory was applied to a convergent \mathbf{B} field region leading to a wall on which a sheath is present. This work has been described in full detail in Ref [14], which is a result of the collaboration between MIT and the UPC, Madrid.

A quasi-neutral pre-sheath develops in the wall vicinity, and electrons are strongly confined away from the wall, both electrostatically and magnetically (due to magnetic mirroring); this justifies using an isothermal barometric Boltzmann relation to relate electron density to potential:

$$n_e(\phi) = n_\infty \exp(e\phi / kT_e) \quad (1)$$

On the other hand, the ion population is attracted to the wall by the electric field, but repelled by the mirror forces, and their distribution function needs to be established separately. This is

done through the fact that the distribution function is an arbitrary function of the particle constants of the motion, this function to be selected so as to merge into a prescribed distribution far from the wall, where the B field is zero or very small. Once the ion distribution function is derived, its velocity integration produces the ion density as a function of the potential and the local B field strength, and when this is equated to the electron density (Eq. 1), the potential at a prescribed B field is calculated. The bulk of the derivation is made under the assumption that ions are strongly magnetized, so that the constants of the motion are the total energy and the magnetic moment:

$$E = \frac{m_i}{2}(w_{\parallel}^2 + w_{\perp}^2) + e\phi$$

$$\mu = \frac{m_i w_{\perp}^2 / 2}{B} \quad (2,3)$$

However, one of the main contributions of the work, which is more rigorously explained in reference [14], is that almost the same formalism applies if the ions are not magnetized, but the electrons are. This comes about because the tight electron confinement produces a narrow and strong potential depression in the vicinity of the central B-line leading to the cusp, and since this “electrostatic canyon” is convergent, the ion-confining forces it produces have a component away from the wall, in complete analogy with the mechanism that produces magnetic mirror forces. This leads to the appearance of a new adiabatic invariant, entirely analogous to the magnetic moment, but of electrostatic origin; in case of non-magnetized ions, this new invariant replaces the magnetic moment as one of the necessary constants of the motion, and the rest of the formalism is not affected.

The theory is first developed in full analytical form for a mono-energetic distribution, and is then generalized to the Maxwellian case. It turns out that the mono-energetic version, much easier to visualize and calculate, ends up producing nearly the same moment predictions as the more realistic Maxwellian model, with the exception of the parallel transport of parallel random energy, which is zero in the mono-energetic case, but not in the Maxwellian case. The nature of the ion distribution function in this mono-energetic case is illustrated

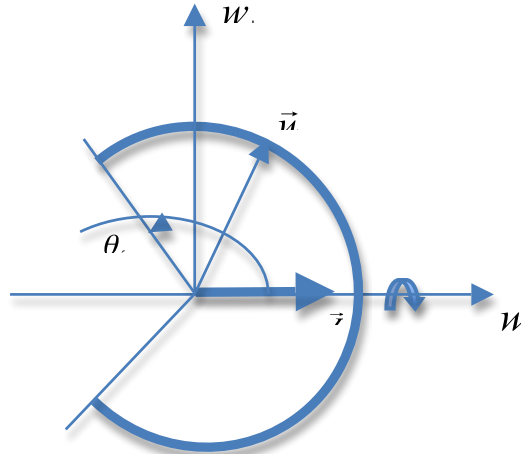


Fig. 16. Shape of the ion distribution function at one (B, ϕ) location, and for one particular energy; the limiting angle is $\theta_T = \sin^{-1} \sqrt{\mu_T / \mu_m}$, which is 90° at $B=B_T$ and 180° at $B=0$. Here, μ_m is the maximum magnetic moment (corresponding to particles bouncing back at the given location) and μ_T is the minimum of the μ_m values along the magnetic tube, occurring where $B = B_T$.

in Fig 16. It is a spherical shell in velocity space with a cutout that reflects the particle velocities that are missing due to absorption at the wall. The case in which the distribution is Maxwellian far from the wall yields a distribution made up of energy shells like that in the figure.

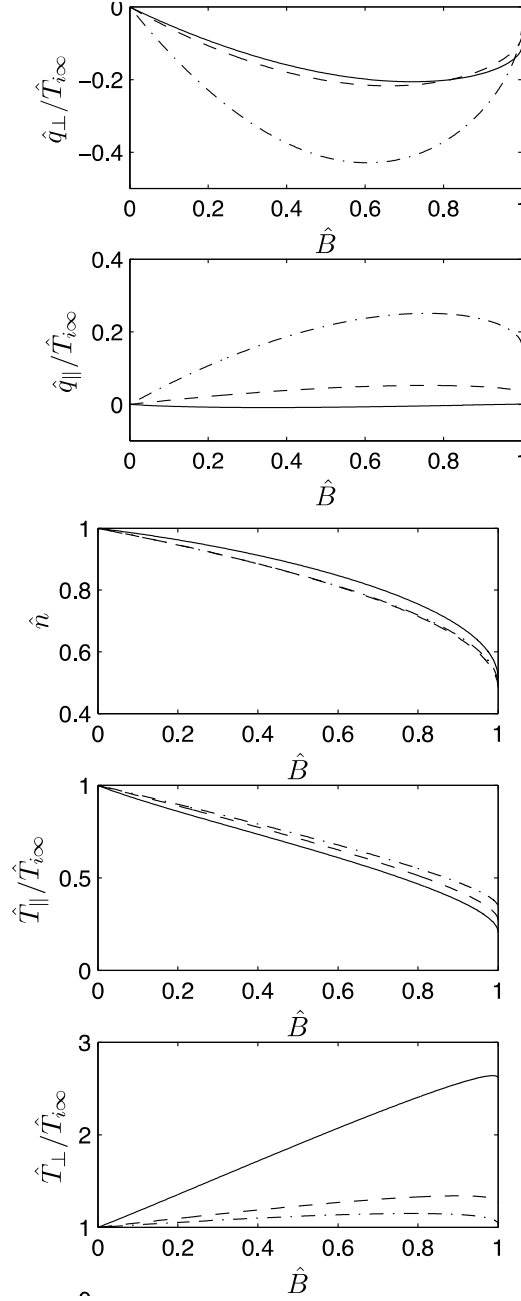


Figure 17: Spatial profiles (in terms of B) of main magnitudes for a Maxwellian population of ions. Solid and dashed lines are for $\hat{T}_{jc} = 0.1$ (solid), 1 (dashed), and 10 (dash-and-dot).

Once the ion distribution function is known, moments can be easily computed by integration. Figure 17 shows a selection of these moments, Ion temperatures are normalized by T_e , density by that at infinity, and heat fluxes by $n_\infty k T_e \nu_{Bohm}$. Both heat fluxes shown are in the parallel direction, but q_{\parallel} is the transport of parallel random energy, whereas q_{\perp} is that of perpendicular energy.

One important conclusion from Fig. 17 is that the density ratio at the wall (and hence the wall potential, from Eq. 1), is very similar in magnitude to what one finds in non-magnetized pre-sheaths. This is further emphasized in Fig. 18, that collects sheath-entry quantities over a range of ion/electron temperature ratios. Perhaps the most important parameter here is the normalized sheath-entry flux, $\hat{\Gamma}_i = n_s u_s / (n_\infty \sqrt{kT_e / m_i})$, which is in all cases of order unity. This is not a trivial result, because there is an intuitive expectation that the magnetic mirror repulsion will have the effect of reducing this ion flux. Instead, the wall-protecting role of the cusp is fulfilled solely by the restriction of the “spot size”, ie, the wall area that can be reached by ions that originate in the Maxwellian bulk. This spot size is determined by how the flux tubes are filled through diffusion in the collisional distant plasma, and is therefore outside the scope of the present theory. As noted in Section 4, various authors have found it to have widths of the order of the hybrid gyro radius, and this agrees with our measurements.

One additional consequence of the availability of the exact ion distribution function and its moments is the possibility of verifying some of the lower-order moment equations (continuity, momentum, parallel and perpendicular energy...). These are normally truncated at some level, or terminated through ad-hoc closure models that relate the highest moments to combinations of the lower ones. For example, a common approximation is the neglect of the “heat fluxes”, or their approximation via a Fourier-like thermal conductivity. This is clearly not appropriate in low-collisionality situations, where the lack of symmetry of the distribution function that gives rise to heat flow is solely due to particle loss at the wall, and is therefore non-local and unrelated to collision events. We have re-derived the exact moment equations listed above for our collision-less situation, and have verified that they are exactly satisfied by our kinetic solutions, provided the kinetic heat fluxes are included; this does not, unfortunately, solve the closure problem, because the kinetic information is not normally available a priori, but it can serve as a useful test of future proposed closure schemes for low-collisionality situations. As a final point of interest, we found that the exact parallel and perpendicular energy (or pressure) equations admit a pair of exact conservation laws that extend the classical Chew-Goldberger-Low laws (Ref [15]), in which the heat flows were simply neglected. These new equations are:

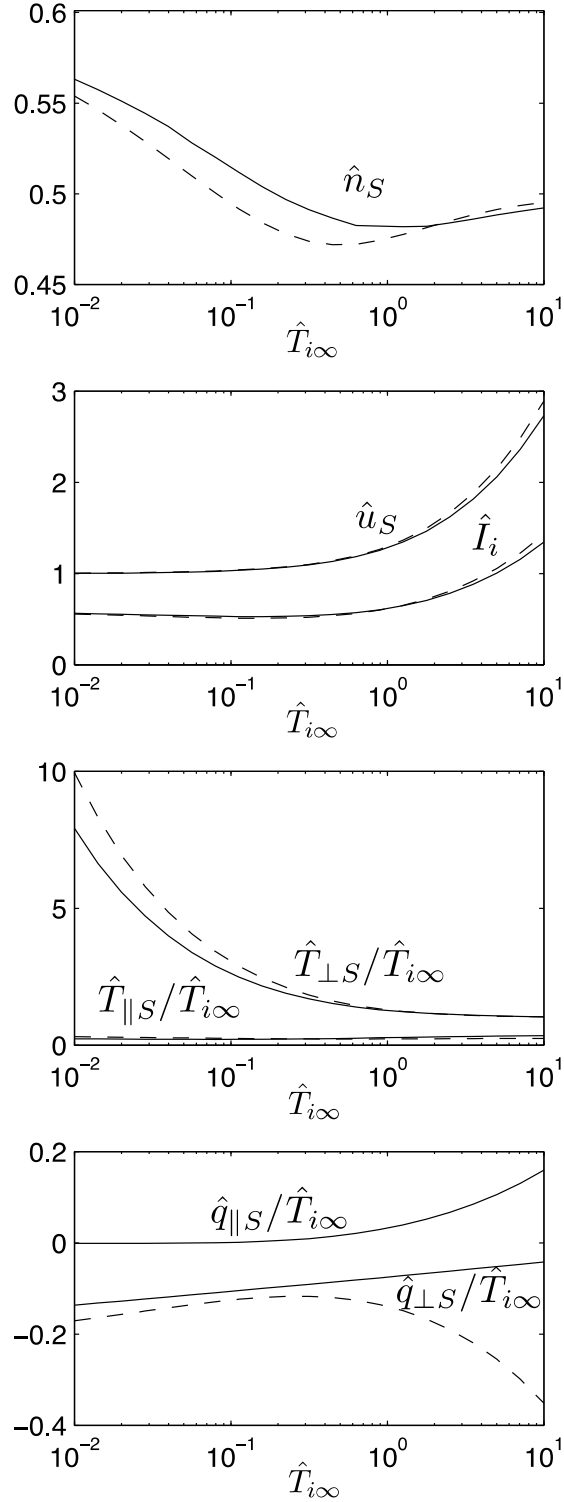


Figure 18: Parametric response at the sheath edge S for Maxwellian (solid) and monoenergetic (dashed) population of ions in terms of its unperturbed temperature. For the mono-energetic population, $q_{\parallel} = 0$.

(a) An extended form of the conservation of mean magnetic moment:

$$\frac{d}{dz} \left(\frac{kT_{i\perp} + q_{i\perp} / \Gamma_i}{B} \right) = 0 \quad (4)$$

(b) An extended total enthalpy conservation law:

$$\frac{dH_i^*}{dz} = 0 ; \quad H_i^* = \frac{1}{2} m_i v_i^2 + \frac{3}{2} kT_{i\parallel} + kT_{i\perp} + \frac{q_{i\parallel} + q_{i\perp}}{\Gamma_i} + e\phi \quad (5)$$

Here $\Gamma_i = n_e u_i$ is the ion flux, and the other symbols have the customary meaning.

6. Spectroscopic exploration

At the outset of the grant we acquired broad band spectra, from 300-1000 nm, of the thruster operating in three distinct operational modes (Ref.[6]). The high current (HC) mode was obtained with the anode at 430 V and 0.58 A (8.5 sccm of Xe), and is characterized by a bright, filled-in plume and large amplitude anode current oscillations. The low current (LC) mode corresponds to the visual coalescence of the plume to angles around 30° from the thruster axis and a steep drop-off in the amplitude of anode current fluctuations, and was obtained for this study with the anode at 415 V and 0.47 A (8.5 sccm). A third, less common, mode was obtained with an anode voltage of 280 V and current of 0.85 A (8 sccm of Xe), which is visually diffuse and reddish and marked by high levels of anode current with little fluctuation. This mode is referred to here as the ultra-high current (UHC) mode and is briefly mentioned in a later study on anode current oscillations where it is found to coincide with high vacuum chamber pressures.

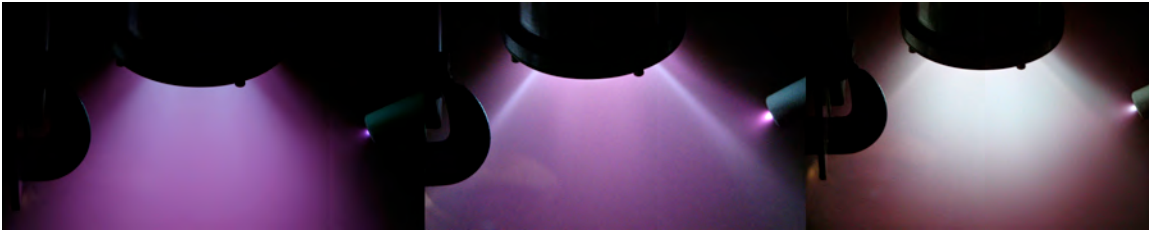


Figure 19. Images of the DCFT near plume in (far left) UHC (middle) LC and (far right) HC modes

A 1-m telescoping assembly was used for the broad spectra which collects radiation from a large volume of the plume, viewed axially. The high density plasma inside the discharge chamber and up to several centimeters past the exit is expected to dominate the collected emission. The necessarily high ionization rates and strong possibility of a non-Maxwellian electron distribution in the discharge chamber make it difficult to confidently apply a Coronal model to the collected radiation as is sometimes done to good effect in Hall thruster plumes.

Over 230 Xe I and II lines were identified within the measured spectra, but only 23 lines from each species were found with documented Einstein coefficients. These lines and their properties are tabulated in Appendices B and C of Ref. [6] along with the calibrated radiant

flux density results for each operational mode. The relative populations for the upper states of each line can be estimated based on the normal emission coefficient equation, under the assumption that the plasma is optically thin.

For all three operational modes the neutral Xenon spectrum is dominated by radiation from the highly populated, low energy upper states at NIR wavelengths. The high energy levels, resulting in visible Xe I lines account for more of the total population in the UHC spectrum than in HC and LC operation, totaling 15.4% of the total compared to 13.4% and 12.7% respectively.

Conversely, in the Xe II spectrum the high energy levels account for the highest percentage of total emission when operating in LC mode. The eight ion lines with upper level energies above 15 eV account for 22.4% of LC emissions, compared to 19.5% and 20.4% for the UHC and HC modes respectively. The slight increase in higher energy level population may be due, amongst other possibilities, to an elevated electron temperature in the discharge chamber, Xe III recombination in the plume or quite plausibly to the lack of a large sample size of Xe II lines.

The ratios of measured Xe II populations to Xe I (calculated from measured radiant fluxes and tabulated Einstein coefficients) are low for all three modes, likely due to the smallness of the subsets for which transition probabilities are available. The UHC and HC mode spectra exhibit nearly identical ion-to-neutral ratios of 5.02% and 5.04%, respectively, while the LC mode fraction is much lower at 2.15%. For comparison, the ratios of the total radiant flux from all 149 measured Xe II lines to all 89 Xe I lines are 0.277, 0.261 and 0.126 for the UHC, HC and LC modes. The substantially lower ion-to-neutral fraction measured in the LC mode is in keeping with the large drop in utilization efficiency measured by electrostatic probes in the plume.

Spectral measurements in the 470.5 - 479.5 nm range were made in order to examine trends in emission from multiply charged ions, which went uncaptured by the broadband spectra. Multiple Xe III, IV and V lines lie in this range, but measurements only revealed radiation from doubly charged ions despite integration times of several minutes (compared to 5 seconds for broadband scans).

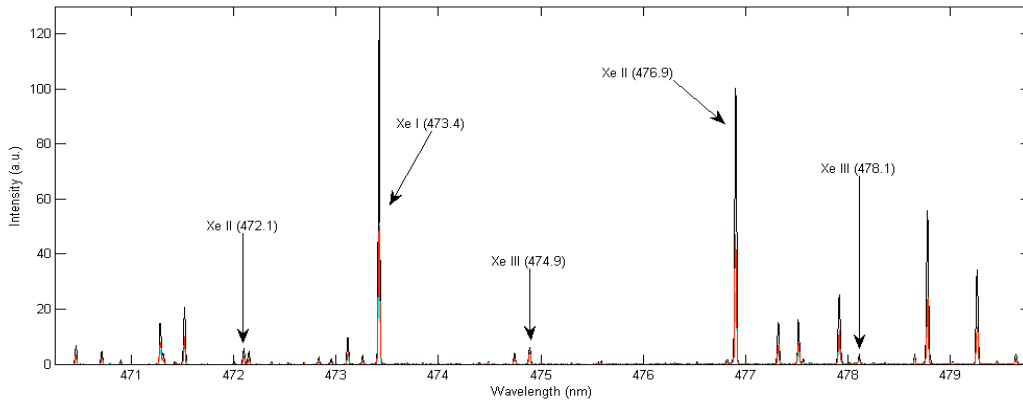


Figure 20. Narrow band spectrum exhibiting Xe I-III lines for UHC (black), HC (red) and LC (blue)

The two brightest, resolvable Xe III lines are at 474.9 nm and 478.1 nm. The 478.1 nm line exhibits particular qualities, shared by the Xe II line at 472.1 nm. Both lines have high energy upper states which are not radiatively linked to any higher states, eliminating cascade contributions in the population rate equations and any pressure dependence that could come about from radiation trapping. At the same time a high upper level energy typically makes it hard to apply coronal equilibrium approximations due to small excitation cross sections from the ground state and slow radiative decay times. The current assumption that the ion line intensities are linearly proportional to ion species density times electron density is admittedly not well founded without knowledge of the various excitation cross sections or transition probabilities.

Further complicating analysis of Xe II emission is the possibly large contribution from asymmetric charge exchange, where a Xe^{2+} ion collides with a Xe^0 atom and leaves two excited Xe^{1+} ions. Miller et. al. [Ref. 16] measured a $3 \times 10^{-20} \text{ m}^2$ cross section for such a process for 600 eV doubly charged ions, compared to typical Xe II excitation cross sections of less than 10^{-22} m^2 for electronic collisions.

The only Xe I line that was observed, at 473.4 nm, is populated by 6 higher energy states, including two which have resonant transitions with the ground state and therefore the excitation cross section for this line is likely strongly dependent on the neutral density.

Anode voltage and mass flow rate scans were performed with the thruster operating in UHC mode to examine trends in Xe I, II and III emission. The voltage scan was performed at a constant flow rate of 8 sccm and near constant anode current of 0.89A. The intensity ratios of the aforementioned lines suggest an increasing ion-to-neutral ratio with applied potential, peaking around 215 V in UHC mode, while the fraction of doubly charged ions appears to gradually decrease.

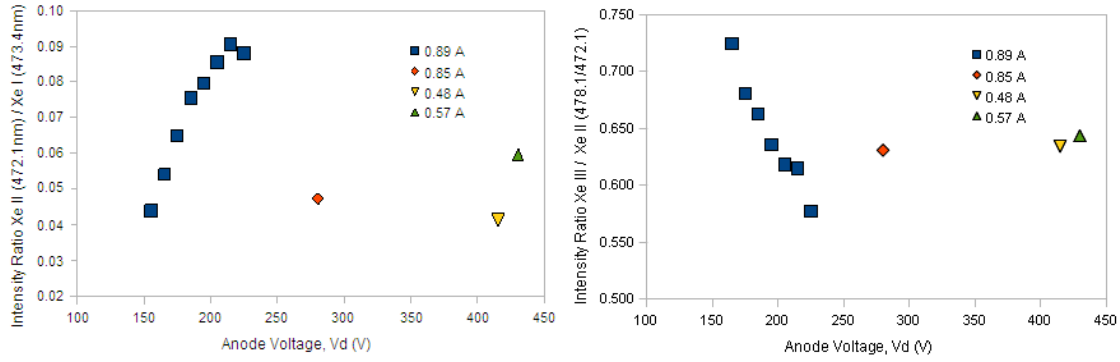
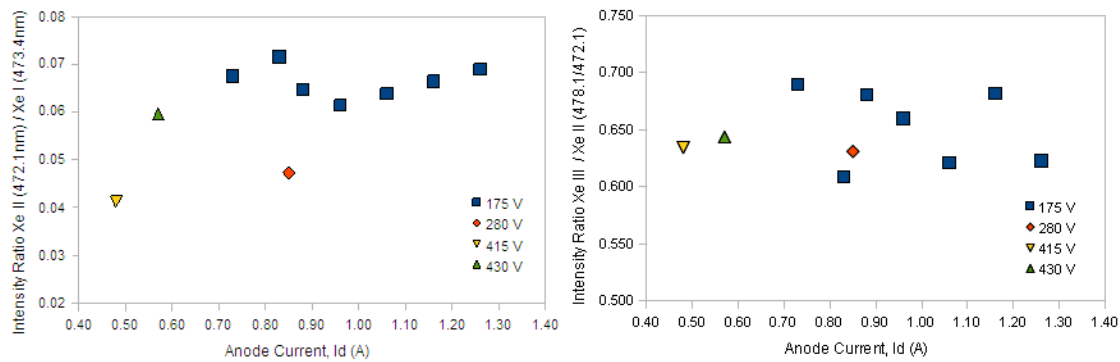


Figure 21. Ratios of Xe singly-charged (left) and doubly charged (right) ions to Xe emission intensity one charge state lower as a function of anode voltage, roughly constant anode currents. Red and blue markers are in UHC mode, yellow is in LC mode and green is in HC mode.

Similar spectra were taken at various anode voltages of the BHT-200 Hall thruster for comparison. The Xe III/Xe II intensity ratio was also seen to decrease slowly with voltage and had an average value of 0.68 compared to 0.64 on the DCFT. Measurements by Ekholm and Hargus [Ref. 17] on a BHT-200 taken with an ExB probe suggest the $\text{Xe}^{2+}/\text{Xe}^{1+}$ fraction ranges from around 4-7%. A more reliable comparison can be made between the LC and HC mode data, with LC mode showing both a lower ion-to-neutral fraction and $\text{Xe}^{2+}/\text{Xe}^{1+}$ fraction, due to the expected similarity in temperature. It would seem then that the transition from HC to LC mode results in substantially less ionization of the incoming propellant into the singly charged state, with perhaps a smaller reduction in the overall production of doubly charged ions.

The effects of neutral flow on the observed emission intensity ratios was examined by varying the flow rate from 7 to 10 sccm in 0.5 sccm increments at a constant anode potential of 175 V. The results suggest surprisingly little dependence of the ion-to-neutral ratio on mass flow rate within the UHC mode. In this case, the Xe III line emission intensity grows



with flow rate roughly proportionally to the Xe II emission intensity.

Figure 22. Ratios of Xe singly-charged (left) and doubly charged (right) ions to Xe emission intensity one charge state lower as a function of anode current, at constant anode current. Red and blue markers are in UHC mode, yellow is in LC mode and green is in HC mode.

The presented ratios contain a temperature dependence, the extent of which is not quantified. The ratio of NIR Xe I emission lines at 823.1 nm and 828 nm is used to allow some

estimation of the electron temperature dependence on discharge conditions, as has been done by several authors to diagnose the electron temperature of similar electric propulsion plasmas. The dependence of the 823 nm / 828 nm ratio on temperature, as calculated by Karabadzhak et al [Ref. 18], is dependent on the electron energy distribution function, which may deviate substantially from the assumed Maxwellian, as well as the ion energy. Using the method of Karabadzhak et al. we find temperatures at all conditions that are in excess of 20 eV and therefore outside the range of prediction by this technique.

The general trend, regardless of the distribution shape, is a decrease in the ratio of emission intensity from 823 nm to 828 nm as the electron energy increases. This trend is mirrored, as expected, by the ratios measured from the DCFT operating in UHC mode. The effective temperature is seen to increase with the anode potential until the mode change from UHC to LC, whereupon the temperature appears to drop dramatically. Results from the flow rate scan demonstrate a gradual drop in temperature as the input neutral flow is increased, likely due to a quenching of the electron energy by increased collisions with neutrals.

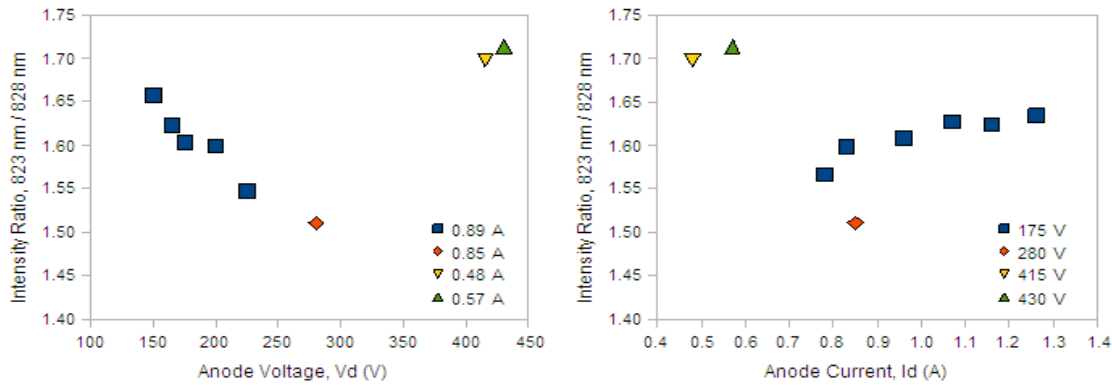


Figure 23. Ratios of Xe I lines used to diagnose electron temperature vs. anode voltage (left) and anode current (right). Red and blue markers are in UHC mode, yellow is in LC mode and green is in HC mode.

It is important to note that the lack of spatial resolution ultimately hinders much interpretation of the results. The volume integrated measurements do not capture the entirety of the plasma radiation and are affected in an unquantified manner by the differences in plume geometries in the different operational modes.

Axial trends in ion velocity were also measured by observing the Doppler shifted profiles of the Xe II line at 484.33 nm. This particular line is chosen due to its high relative intensity and proximity to two high intensity neutral lines. The neutral lines are used to perform a linear wavelength calibration for each spectrum observed.

The spectral measurements have a pixel-to-pixel resolution of 1 pm when centered at 483.7 nm, which corresponds to a Doppler shift of roughly 600 m/s projected along the line-of-sight. Even at 1000 K, the thermal speeds of neutral particles will fall below the pixel-to-pixel Doppler shift speed and the neutral emission measured at any angle can be considered spectrally stationary. Charge exchange ions created downstream of the main potential drop may also be stationary within the measured spectra, and can be expected to contribute to the shape of the ion line intensity profiles.

An optical fiber is set to view the plume radially 35 mm downstream of the thruster exit while another views the plasma at a 30° angle from the thruster axis, pointing downstream and crossing the path of the radial fiber on-axis. Data are presented with the thruster operating in HC mode at 260 V and 0.76 A. The radial fiber view of the Xe II line exhibits the expected symmetry, with a stationary peak due to the axially directed ions near the center of the plume likely mixed with a number of slow moving charge exchange ions. The extended wings in the radially viewed line are due to Doppler shifted emission from ions with divergent velocity vectors.

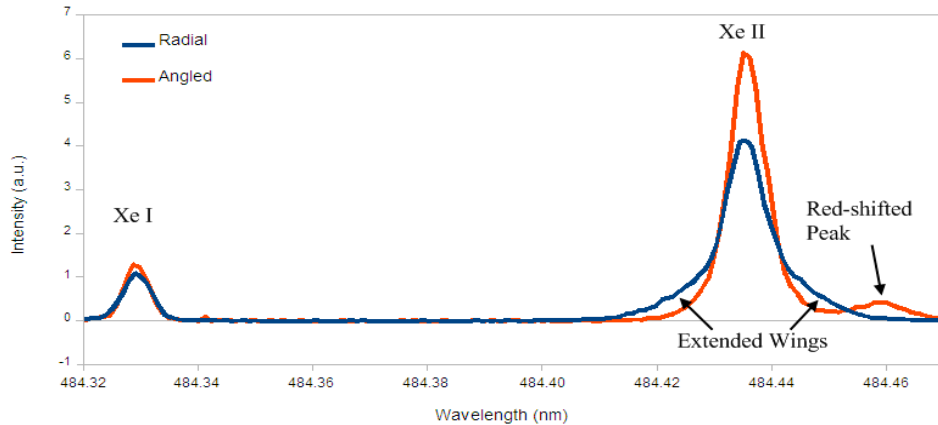


Figure 24. Radial and angled optical fiber viewed emission spectra of DCFT plume 35 mm downstream of exit

In essence the angled fiber is expected to collect from three distinct regions. A nearly unshifted contribution (due to orthogonality with the viewing angle) is expected from the collimated beam emanating 30-40° from the thruster axis on the near side. A slightly red-shifted population is expected near the thruster axis, and a strongly red-shifted peak is expected where the optical view meets the collimated beam on the far side.

The small red-shifted peak seen from the angled view is at a wavelength 23.3 pm higher than the larger unshifted peak, corresponding to a velocity component of 14.3 km/s, 60° off axis. The velocity required of a purely axially moving ion to exhibit such a large Doppler shift is beyond that possible with the supplied anode potential. The low intensity, red-shifted peak must then be due to divergent ions on the far side of the thruster axis.

The angle at which the ion velocities diverge from the thruster axis is gauged by the emission of the brighter, divergent ions on the near side of the axis. Since no red or blue shifted near-side population is observed, the velocity angle must be nearly orthogonal to the line-of-sight, and thus around 26-34° from the thruster axis.

At 30°, the observed red-shifted population is then traveling at 16.5 km/s, corresponding to a potential drop of 190 V. The velocity at this angle measured 65 mm downstream of the exit is 17.5 km/s, which corresponds to the expected 210 V acceleration, or 50 V below the anode potential. The Xe II line profiles from both fibers were measured every centimeter from 3.5

up to 6.5 cm from the thruster exit. At greater axial distances the signal becomes too weak to obtain a reliable measurement.

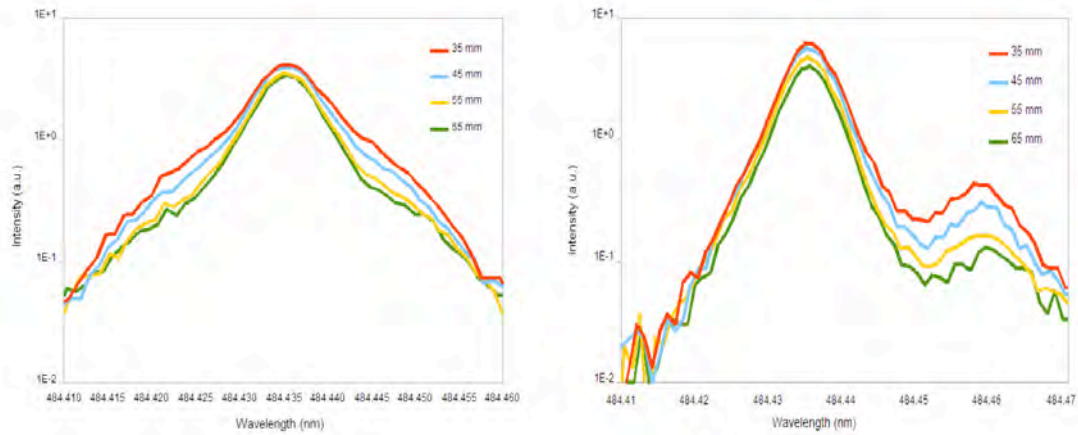


Figure 25. Xe II Line Emission Intensity vs. Wavelength at Various Distances from the Thruster Exit. Viewed (left) Radially and (right) at a 60° Angle. Operating at 260 V and 0.76A with 8 sccm of Xenon.

The line profile evolution shows the main peak intensity dropping less than the Doppler shifted regions further from the thruster exit under both views. The red-shifted peak measured by the angled fiber tends to move to slightly redder wavelengths with distance from the exit, resulting in a slow divergent ion velocity evolution. The uncertainty in the measured Doppler shift is taken as half the inter-pixel distance, corresponding to a velocity of 360 m/s.

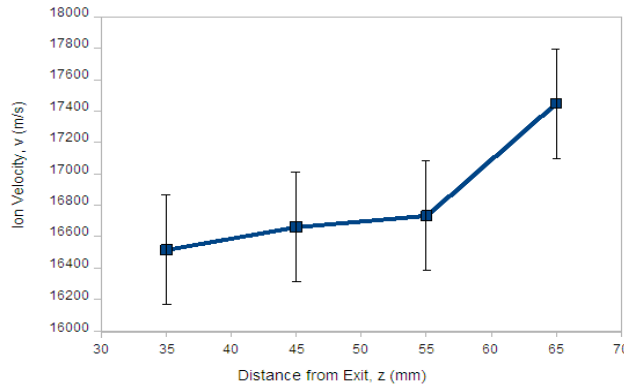


Figure 26. Evolution of measured Doppler velocity for an assumed 30° off-axis jet with distance from thruster exit. Operating at 260 V and 0.76 A with 8 sccm of Xenon.

The effects of anode potential on the Xe II line shapes were also measured. The anode current was maintained at 0.76 A during the voltage scan by adjusting the mass flow rate. Increasing emission from the far wings of the radially viewed ion line is observed with increasing anode potential. The intensity appears nearly constant for all anode potentials around 9-10 pm from the central wavelength, which would correspond to an ion velocity around 12 km/s pointed 30° off axis.

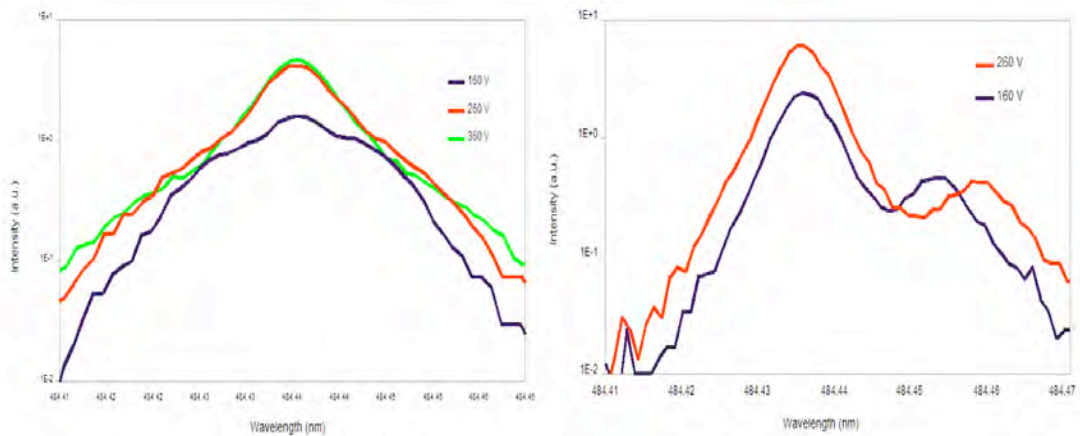


Figure 27. Xe II Line Emission Intensity vs. Wavelength at Various Anode Voltages. Viewed (left) Radially and (right) at a 60° Angle. Operating at around 0.76A with 8 sccm of Xenon.

The red-shifted peak, viewed by the angled fiber, at a 160 V anode potential corresponds to a divergent ion velocity of 12 km/s, or the equivalent of a 100 V accelerating potential. The accelerating voltage is 60 V below the anode potential, compared to a 70 V difference measured at the same location with 260 V applied to the anode.

7. Plume Structure Data

Ion current density and ion energy flux distributions in the plume were measured using a Faraday cup and retarding potential analyzer. Experiments were carried out in Chamber 1 of the Edwards AFB AFRL Space Propulsion Branch from July-August of 2009. The thruster used in these tests is identical to the thruster built and characterized for the first tests of the concept [1,5]. During tests and measurements, the chamber xenon pressure did not exceed 3.5 μ Torr. The cathode location was identical to the position reported in previous studies.

Figures 28 and 29 show the thruster operating in the high and low current modes, respectively. Details of the study not given here were presented previously [Ref. 19].

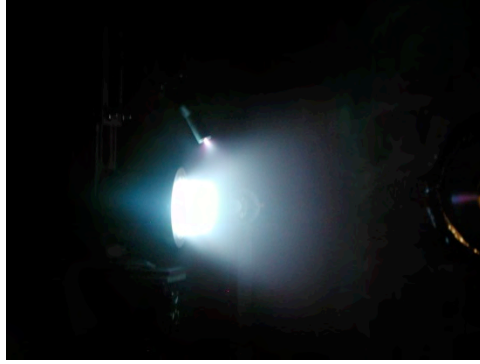


Figure 28: DCFT operating in high-current mode

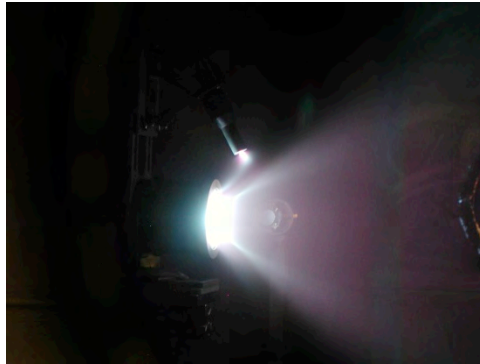


Figure 29: DCFT operating in low-current mode

Measurements of ion current densities and energies downstream of the thruster exit were attempted to study the plume structure, expanding upon preliminary measurements performed at MIT. Using a Faraday cup and an automated acquisition system, the current density in the high-current mode was obtained over a range of probe angles in 1° intervals, as shown in

Figure 0. The distribution of current shows a plume structure consistent with visual observations. The data show a hollow cone of plasma with the maximum current density located between 30 and 35 degrees. The current density on the centerline of the thruster is about a factor of 2 lower than in the densest regions. Note the logarithmic scale in

Figure 0.

The current density also begins to increase past $\Theta > 80^\circ$, before decreasing again at larger angles. This is most likely due to charge exchange collisions with neutral particles. Doubling the cathode keeper current from approximately 0.25 A to 0.50 A had a negligible effect on the observed distributions of ion current densities and energies in the plume.

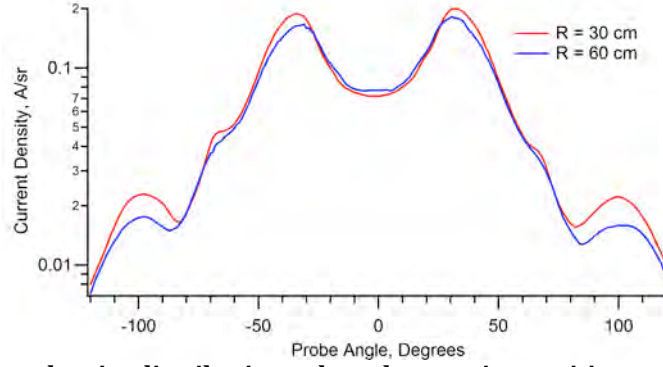


Figure 30: Ion current density distributions plotted at varying positions with respect to the DCFT exit plane. The thruster operated in the high-current mode, with an anode voltage of 450 V and a mass flow rate of 8.5 sccm.

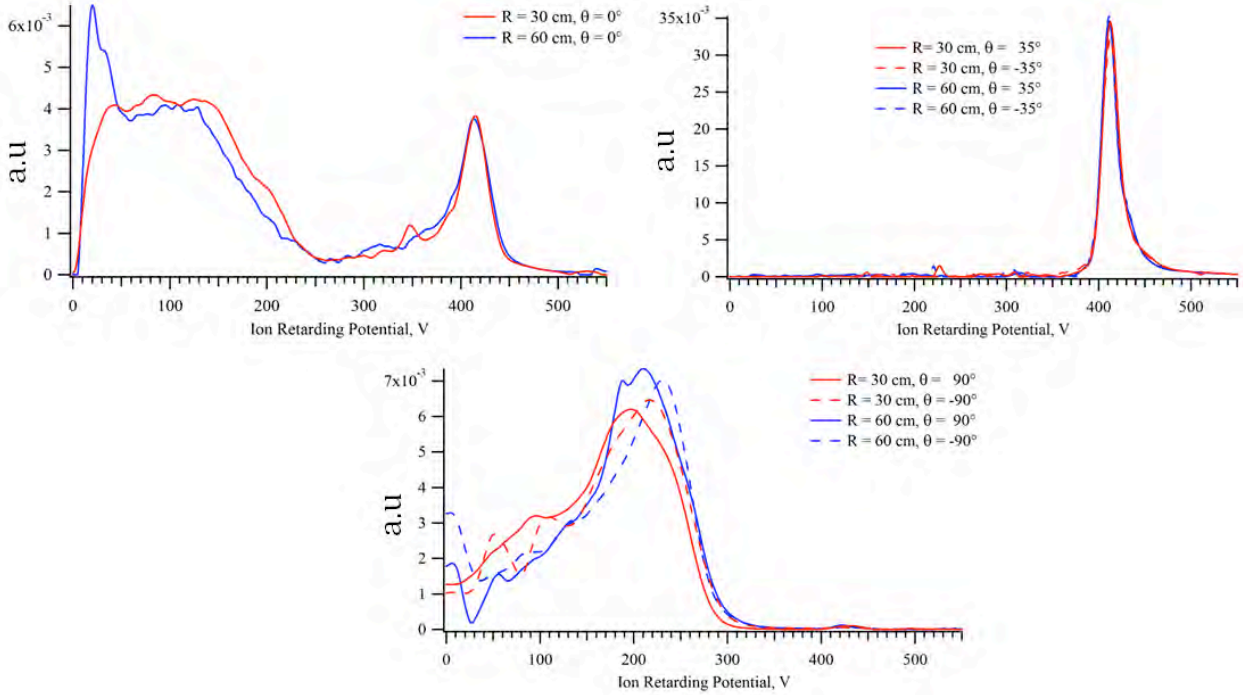


Figure 31: Ion energy flux distributions in the high-current mode. The operating condition is the same as in Fig. 30. The centerline plot is representative of data in the range $|\Theta| < 15^\circ$. The plot showing the distribution at 35° is representative of the data for $20^\circ < |\Theta| < 75^\circ$, and the plot at 90° is representative of the data in the range $85^\circ < |\Theta| < 120^\circ$. Each plot off of the centerline shows measurements at two different radii and on either side of the axis of symmetry.

Ion energy flux distributions were measured at a number of locations in the thruster plume at the same high-current operating conditions as the current density measurements. As shown in Figure 31, a mixture of high and low energy populations is present near the centerline of the thruster, while at intermediate angles there is a single population of ions, most of which have energies no-less than 50 eV of the anode voltage. For angles greater than 85° , ions are more energetically dispersed, with a peak in the distribution of no more than half the anode voltage. The presence of these ions at such

large angles from the centerline would present problems for satellite components located near the periphery of the plume. Although the current density at these high angles is an order of magnitude less than the maximum, the energies of ions measured at high angles in the DCFT are greater than those measured in Hall thrusters [Ref. 20].

The beam current was determined by integrating the measured ion current densities for $0 < \Theta < 90$, which also allows the ninety percent current half angle ($\Theta_{90\%}$) to be determined. The beam (η_b) and utilization (η_u) efficiencies, along with the values of $\Theta_{90\%}$ calculated at different operating conditions, are presented in Table . The beam efficiency is defined as the ratio of the beam and anode currents, while the utilization efficiency is the ratio of the beam and neutral currents. For the conditions examined, the high-current mode has a beam efficiency between 70-80% and a utilization efficiency between 60-70%. At chamber pressures 8-10 times greater than the measurements at AFRL, a preliminary, incomplete interrogation of the plume gave $\eta_b = 75\%$ and $\eta_u = 86\%$ in the high-current mode at the same 300 V, high-current mode condition shown in Table 2. In the same study, data in the low-current mode with $V_a = 450$ V and an anode flow rate of 8.5 sccm indicated that $\eta_b = 73\%$ and $\eta_u = 62\%$. In that case, the trends do not agree with those shown in Table 2, and seem to indicate no discernable difference in η_b between the two modes, and a less severe dip in η_u . As a result, our knowledge of the plume structure and related efficiencies in the low-current mode remains limited.

Table 2: Calculated efficiency and divergence parameters for the listed conditions. The mass flow rate in the high-current (HC) mode was 8.5 sccm, and 5.8 sccm in the low-current (LC) mode. The first value listed is integrated over a probe radius (R) of 30 cm. The second value corresponds to R=60 cm, and is listed where it differs significantly from the value at R=30 cm.

Mode	V_a [V]	I_k [A]	η_b [%]	η_u [%]	$\Theta_{90\%}$
HC	300	0.25	72, 81	62, 70	72°
HC	450	0.25	78, 69	73, 65	70°
HC	450	0.50	75, 70	75, 70	70°
LC	476	1.50	95	32	61°

Operation in the low-current mode at previously tested conditions could not be maintained long enough for complete datasets to be acquired. The inability to sustain the low-current mode under normal circumstances has, thus far, only occurred during tests in Chamber 1 at Edwards AFB. Preliminary low-current measurements at different conditions suggest a more monotonic ion energy distribution, significantly diminished

ion current densities along the thruster axis, and a lack of high-energy ions past an 80° probe angle compared to the high-current mode. However, additional studies will be necessary to discern the degree to which these effects are a consequence of the low-current mode, or the disparate operating conditions of the thruster and cathode.

8. PIC simulation results

Significant improvements in adapting the MIT PIC plasma thruster model to simulate the operation of the DCFT were made. The model is now able to recreate spatial variations in important plasma parameters such as plasma potential and ion current density. Detailed descriptions of the model are available in several reports [Refs. 21-24]. The newer results reported here are also described in Ref. [25]. The simulated operating condition matches the maximum efficiency condition identified previously, with an anode voltage of 550 V and a xenon mass flow rate of 8.5 sccm.

Ion current density in the near plume region is plotted on the left in Figure 32. Upon visual inspection, the concentration of the ion current into a hollow, divergent shell at the exit of the thruster is in qualitative agreement with the visual appearance of the plume in Figure 29. The simulated operating condition is different than any for which experimental measurements are available, but a qualitative comparison proves that the code is reproducing significant characteristics of DCF thruster operation. In Figure 32, the computed results shown on the right represent those shown on the left as they would be measured with a Faraday cup in the plume. Direct comparison of these simulated data with the measured ion current densities is not warranted due to the different operating conditions for the two sets of data. However, the overall shape of the simulated profile captures all the basic characteristics of the experimental data. The inclusion of charge exchange collisions in the model allows for the prediction of the high angle wings. The regions of peak current density are steeper, and drop off past the angle of peak current density sharper for the simulated data. This could be attributed the lack of a simulated finite background pressure, the increased voltage of the simulated operating condition, or a combination of both. The more important aspect of the simulation results is the demonstrated ability to predict significant aspects of the ion current density distribution in the thruster chamber and near plume region.

The simulated electrostatic potential distribution is shown on the left in Figure 33 as the anode-normalized plasma potential in the near plume region. Between the exit plane ($x \approx 5$ mm) and 5 mm downstream, an elevated potential shell surrounds the divergent plasma jet. The adjacent shell inside this radial potential hump is at a slightly depressed potential, recovering towards the thruster axis. The effects of imposed boundary conditions past $x=10$ mm and near the domain edges exterior to the plasma chamber are also apparent. The upper right corner of the domain is specified as the zero potential. Also on the left in Figure 33 is the strong potential gradient at the exit plane of the DCFT, as well as a drop in potential in the C3 cusp near the exit. A detailed look at the plasma potential profile along the axis of symmetry is given on the right in Figure 33. The potential drop is roughly centered about the exit plane and at $x = 4$ mm, only 0.95 mm upstream of the exit plane, the potential remains above 80% of the applied 550 V and then drops off steeply afterward. A similar, but even

stronger potential gradient for the SPPL cylindrical cusped-field thruster has been measured (Ref.[26]), also near the thruster exit plane. Those measurements show a drop from above 80% of the anode potential

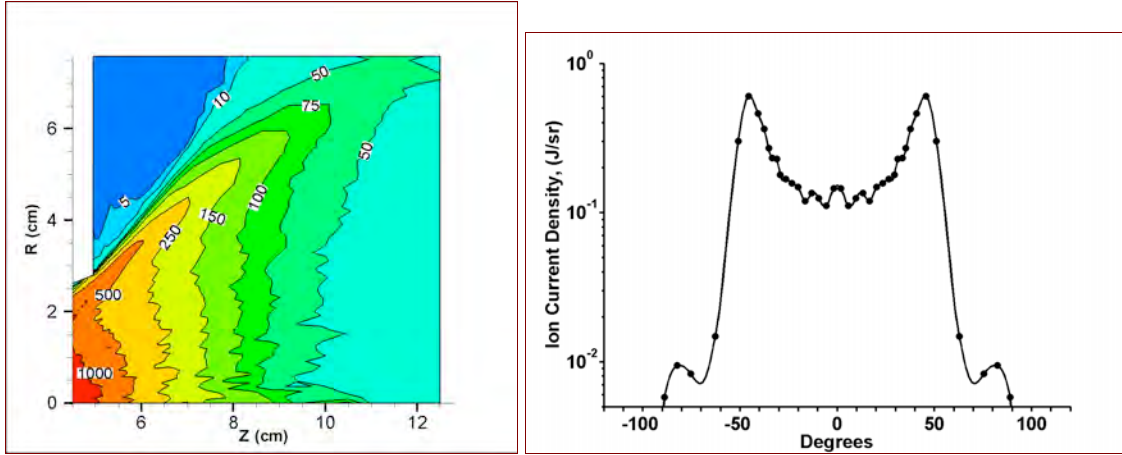


Figure 32: On the left, simulated ion current density distribution in the near plume region, plotted in R/Z . On the right, simulated ion current density profile extracted from the vector form of the data presented in the left-hand figure. The magnitude of the ion current per steradian is plotted corresponding to the angle formed between the velocity of the ion bulk and the z-axis unit vector. The resulting values are then reflected symmetrically about the zero angle to aid in a qualitative comparison to experimental profiles shown in

Figure 30.

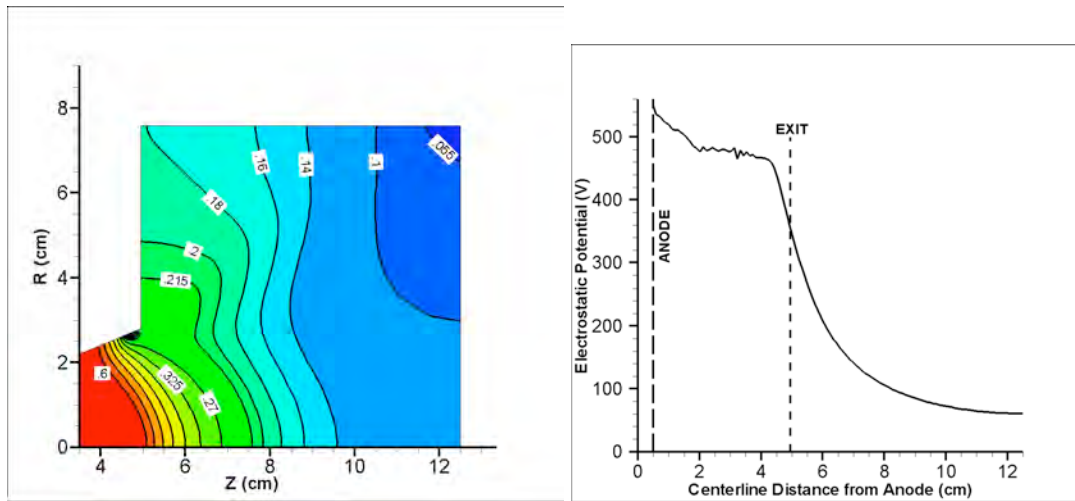


Figure 33: On the left, normalized potential distributions in the near plume. Potentials are normalized by V/V_a and unlabeled lines between 0.2 and 0.9 step down in increments of 0.1 . The coordinate of the exit plane in the simulated coordinate system is $Z=4.5$ cm. On the right, the simulated potential distribution along the axis of symmetry of the thrusters is shown.

to less than 20%, over a distance of less than 1 cm. The length over which the drop on the right in Figure occurs is about 5 cm. Plasma potential measurements with emissive probes in the Stanford and MIT thrusters indicate that the vast majority of acceleration occurs at the

exit. From these simulated data, the main drop in potential coincides with the location of the last downstream separatrix. Measurements of ion velocities at the exit using LIF confirm this conclusion [Ref. 27]. Kinetic simulations of the HEMP thruster also show a sharp drop in potential at the thruster exit, as well as a potential valley in magnetic cusps present in that design (Ref. [28]).

A detailed view of the potential in the region around the magnetic cusp located furthest upstream is shown in Figure 34. Along the wall, the potential descends from 495 V upstream of C1 to 480 V in the cusp. Downstream of C1, the potential rises back up to 495 V before continuing to drop as the distance from the anode increases. The simulated potential depression extends into the bulk of the plasma, and provides a clear picture of how the ion trajectories are coupled to the strongly magnetized electrons, even when the ions themselves are not magnetized.

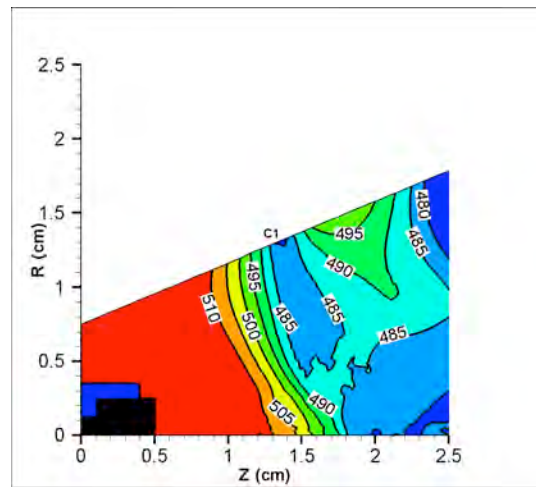


Figure 64: Simulated potential distribution (in Volts) around the upstream cusp, labeled C1. The anode is shown as solid black, surrounded by a (blue) boron nitride insulator. A distinct valley in potential is discernable, corresponding to the location and shape of the C1 magnetic cusp.

Potential profiles such as the one in Figure 64 have been postulated in a collisionless kinetic model of plasmas in magnetic cusps developed as an offshoot of studies on cusped-field thrusters [Ref. 14], and support arguments that cusped magnetic topologies offer significant shielding of thruster channel walls outside of cusps. However, the kinetic model of [14], also predicts that ion flux levels will be of the same order as cases without magnetic cusps over the small region in which the field lines intersect the channel walls. What will ultimately determine the effectiveness of cusped-field arrangements at providing improved lifetimes in miniature plasma thrusters is the energy with which the ions impinge upon chamber surfaces. Erosion measurements of the DCFT operating in the high-current mode were completed, with the details summarized in Section 11 of this document. Erosion was found to be localized to the immediate vicinity of each cusp, as well as downstream of the last cusp. The limiting erosion rate was determined to be lower than in Hall thrusters operating at similar anode powers, though of the same order of magnitude. Simulated ion loss widths to the walls in C1 and C2 are a factor of 3 larger than those estimated from erosion rate measurements in each cusp, while the loss widths based on probe measurements were larger than the erosion based estimates by a factor of 2-4. However, none of the operating conditions were identical between the three sets of estimates, so a direct quantitative comparison is not warranted.

With some further refinement, the MIT PIC plasma thruster model can be expected to provide the data necessary to gain further insight into the basics physics of cusped-field thrusters, and to aid in design decisions that will reduce plume divergence and plasma impingement on internal chamber surfaces.

9. Discussion of plasma structure. Role of the magnetic separatrix.

Given the initial lack of experience with or understanding of thrusters with the strong magnetic dominance characteristic of the DCFT, many of the data we have been discussing so far were taken in efforts to obtain at least a qualitative picture of the nature and distribution of the plasma in and about the DCF thruster. As a consequence of these efforts, both at MIT and at Stanford, a pattern began to emerge, at least for the Low-Current mode, and a conceptual framework has been constructed that ties together most of the observations and computations. We discuss this framework in this section. The more complex effects arising due to the unsteadiness of the High Current mode are still poorly understood, and a discussion of our current understanding of these effects is deferred to Sections 12 and 13 of this Report.

Visually, the bright plasma shell appears to be anchored near the exit plane on a ring with radius about one half that of the thruster there. We can also see a protruding luminous 'bulb', which can be identified with the rapid rise of potential as the exit plane is approached from downstream. Comparison to magnetic field simulations, such as those shown in Figure 44 (Section 10) makes it very likely that the downstream edge of this 'bulb' is just slightly beyond the separatrix line associated with the last cusp. Photographs, and especially visual observation from a 45° angle tend to support this localization of the discharge, as can be seen in Figure 35. This luminosity, and the fact that the strong potential drop starts at this location, indicate strong ionization activity on and very near this portion of the separatrix.

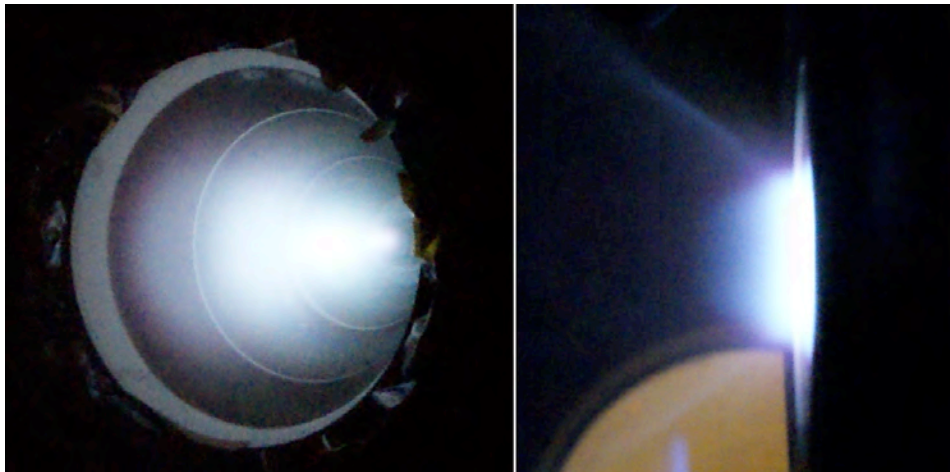


Figure 35. Images of the DCFT firing in LC mode looking into the discharge chamber (left) and across the exit (right)

A plausible explanation for this localization of the ionization activity is offered in what follows. Electrons from the cathode initially fill the cathode-connected B surface, and execute repeated back and forth passes between the cathode and the sheath edge on the ceramic wall, perhaps being forced back earlier through magnetic mirroring. Occasional collisions, most likely with the ceramic wall, aided by some weak turbulent scattering in the presence of the downstream directed E field, have the effect of gradually allowing these electrons to cross magnetic surfaces and approach the separatrix. Once this particular surface is crossed, the electrons switch to the next upstream magnetic cell and start to bounce back and forth between the two cusps. Notice that from the beginning of this new phase, these electrons reach the next upstream cusp not far from its separatrix, so it will not take many bounces to progress into a new upstream cell, and eventually into the anode. By contrast, the initial phase in which cathode electrons are electrostatically trapped between the vicinity of the downstream separatrix and some downstream point can be fairly long, depending on cathode location; since in each bounce the electrons will approach close to the outer edge of the separatrix, a region of intense ionization is to be expected there, as observed.

The mechanism just described serves to explain the 'hollow cone' structure of the plume and, to some extent, its angle. Ions originate, as explained, near the outer rim of the last separatrix, and ionization rate must fall steeply as one proceeds radially inwards on this surface; this is simply a reflection of electron continuity in the converging B field. The majority of ions will then start their acceleration roughly perpendicular to the separatrix, which, by reference to magnetic field simulations, is about the observed angle for the luminous streak seen visually.

Two additional observations can be made: magnetic lines near the last separatrix tend to come close to the axis at some point downstream of the exit. This 'bottleneck' is then a second region of statistical electron concentration, and, given the presence of some neutrals, will give rise to some secondary ionization. This is very likely the origin of the slight potential maximum near the axis that was described earlier (ions linger near their point of origin longer than electrons, giving rise to a characteristic potential bump in ionization regions). The second observation is that one does indeed expect some neutrals to be present near the axis, since chances of escape are greatest there. This is a weakness of the design, and explains the relatively low utilization fraction of the propellant, although the net efficiency is reasonably high because of high current and voltage efficiencies. Perhaps this can be taken as an indication that a smaller divergence angle of the thruster channel might improve performance.

Finally, the observation that electrons should have comparatively little trouble crossing the upstream separatrices implies that one should not expect much ionization to occur near the upstream cusps, and by an extension of the argument made to connect ionization to acceleration regions, that no strong axial potential drop is expected there either. Parenthetically, the claim made sometimes in connection with two-stage Hall thrusters and other devices that they can effect a separation of the ionization from the acceleration region, appears to be physically unsound. Any strong ionization layer must be followed by a strong potential drop, and conversely, a layer of strong potential drop cannot appear in mid-plasma without the occurrence of strong ionization at its entrance.

If the strong ionization is localized near the exit, the expectation, as in a Hall thruster, is that the plasma density should decrease gradually upstream, as required in order to establish a gradient capable of diffusing electrons towards the anode. Translated to erosion rates, one would predict that the maximum erosion should happen at the last cusp, with decreasing values (roughly in proportion to the decreasing densities) in the cusps nearer the anode. However, as will be shown in Section 11, our data indicate maximum erosion in the intermediate second cusp, and this has forced a re-thinking of the arguments presented so far. As Sections 12-13 will argue, the most plausible explanation for the discrepancy is presence of strong unsteadiness during the erosion tests.

10. Effects of magnetic reconfiguration on the plume

10.1 Modifications intended to reduce the external magnetic field

Initial consideration of the peculiar plume structure observed in the DCFT led to the suspicion that the strong magnetic field near the exit, external to the discharge chamber, was defocusing the ion beam by coercing electrons to travel on paths towards the periphery of the device. A permanent magnet version of Princeton's CHT was also seen to exhibit a hollow cone type plume at low anode voltages, while the electromagnet version maintained a centrally-spiked current profile (Ref. [29]). The main difference between the two CHT variants was noted to be the strong external magnetic field. Naturally, in our first attempts to reconfigure the magnet field we chose to weaken its magnitude external to the discharge chamber.

A variety of magnetic shield designs were simulated using Ansoft's Maxwell SV software, with the best results obtained using an 'L' shaped (cross section) piece of iron which would fit over the exit of the thruster. Due to ease of manufacturing and added flexibility in testing we sectionalized the design into a doughnut shaped bib which bolts into the exit face and a thick-walled tube (referred to here as the collar) which surrounds the thruster body. Only the collar was eventually tested, because these tests gave disappointing results, and the more promising avenue of re-shaping the separatrix came into focus as a consequence.

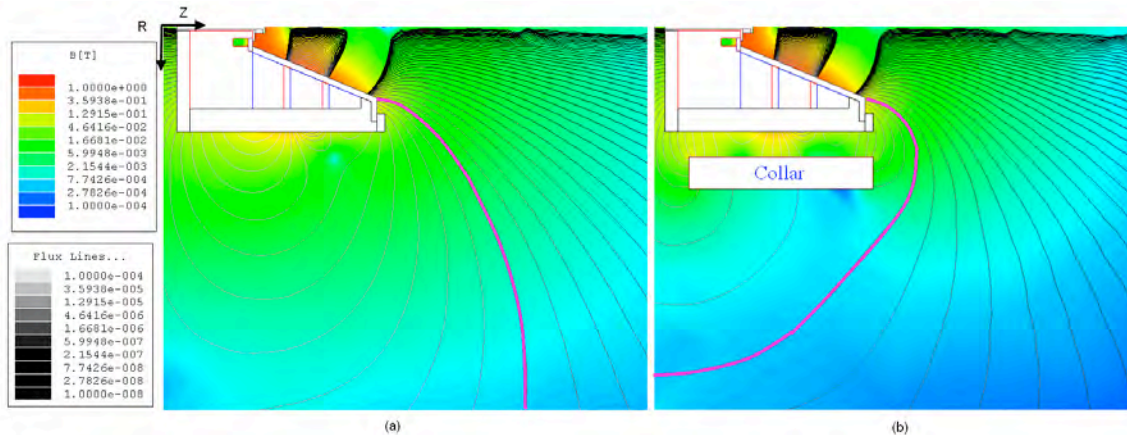


Figure 36. Maxwell SV simulation of DCFT magnetic field strength and flux lines for (a) the baseline configuration and (b) the collared configuration. The pink flux line is the rough location of the line which connects to the cathode plume.

Baseline testing was conducted at an anode potential of 400V and a Xe mass flow of 0.49 mg/s resulting in a 160 mA LC mode. Plasma potential measurements at this condition (Figure 37) reveal a triply peaked diametrical profile. A diverging conical beam of high plasma potential emanates at a half angle of around 30°, with a faster decaying peak running along the axis. The thruster began to exhibit erratic behavior as the emissive probes were brought within several centimeters of the exit plane, with large swings in anode current and brief changes in operational mode. The potential structure in the plume does not appear to coincide much with the applied magnetic field lines.

The addition of the iron collar impacted the ability to obtain stable LC modes over a wide range of conditions. Strong LC operation is achieved in the baseline thruster by lowering the anode flow rate or increasing either the anode voltage or keeper current. In the case of the collared thruster a low flow rate of 0.49 mg/s and a keeper current of 1.5 A were both necessary to remove any flickering between modes. Electric field vectors were found by numerical differentiation of the data and are somewhat rough due to the relative coarseness of the radial scans, but they demonstrate the substantial divergence of the accelerating fields acting on ions which do not exit along the thruster axis.

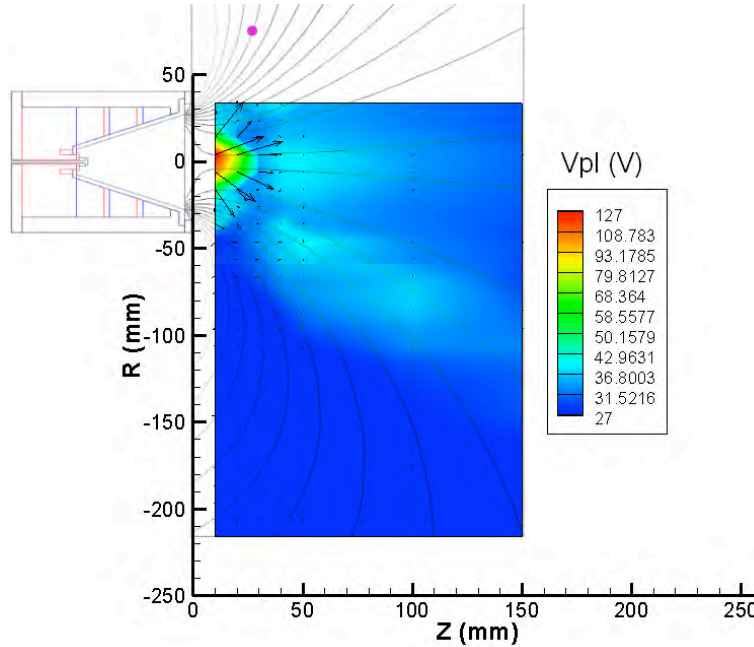


Figure 37. Plasma potential measured by emissive probe for baseline DCFT anode operating at 400V 160mA and 5sccm of Xe w/ 0.5A keeper current. Calculated electric field vectors are plotted with length relative to magnitude. Simulated B field lines are overlaid. Pink dot shows cathode position in B field.

The results in both magnetic configurations bear quite a few similarities with emissive probe measurements made on a cylindrical variant of the thruster by Stanford (Ref. [30]), including the appearance of a potential valley along the thruster axis, just downstream of the exit. In the collared case (Figure 38), the plasma potential drops from 160 V at 5 mm from the exit to 16 V at 3 cm, then rises toward 20 V at 5 cm before approaching 11 V further downstream. There is also a dip in the potential around 3 cm downstream following a 44° angle along the divergent plasma potential ridge.

The baseline case (Figure 37) is similar, dropping from 120V at $Z=1\text{cm}$ to a minimum at 3 cm of 35V, up to a maxima of 39V at 5cm then back down towards 31V at 15cm. The main differences between the two magnetic configurations are the overall lower plasma potential in the collared thruster plume, by a nearly constant 40%, and an increase in divergence of the potential hill by roughly 14° . The overall drop in potential in the collared case may be partially attributed to the 150% increase in keeper current needed to maintain stable operation, a possibility which can easily be tested by running the baseline case again at high keeper current.

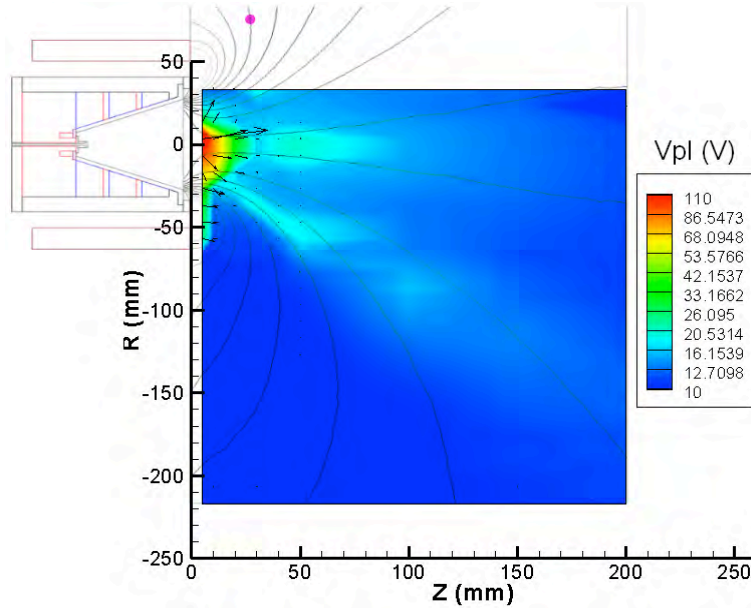


Figure 38. Plasma potential measured by emissive probe for collared DCFT anode operating at 400V 160mA and 5sccm of Xe w/ 1.5A keeper current. Calculated electric field vectors are plotted with length relative to magnitude. Simulated B field lines are overlaid. Pink dot shows cathode position in B field.

Potential measurements made with the collared thruster running in HC mode with 0.5 A running through the keeper, which are presented later, show far-field plume voltages of around 12 V as well, suggesting that the decrease in the potential on-axis is affected more by the change in magnetic field than the cathode properties. The addition of the collar also appears to shift the acceleration upstream by 1 cm, although baseline data were not obtainable less than 10 mm from the thruster exit.

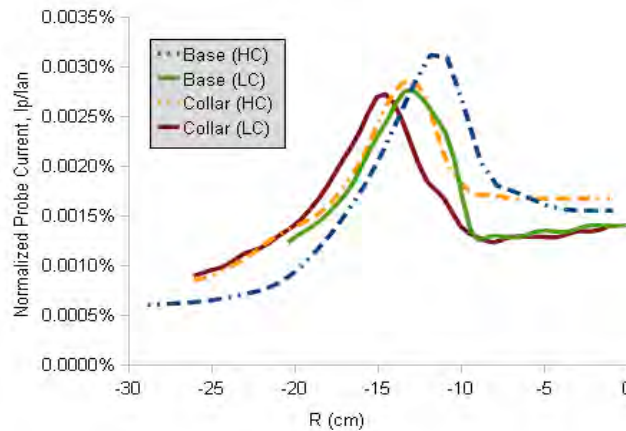


Figure 39. Axial ion current normalized by anode current vs radial distance 20 cm downstream of the exit for both baseline and collared operation in HC (dashed) and LC (solid) modes

Perhaps the clearest comparison between the two magnetic configurations comes from ion current measurements taken 20 cm from the exit face of the thruster. The data show

clearly that the peak in ion current shifts to a higher angle from the thruster axis when the iron collar is attached, changing from 29.7° in the HC baseline (0.73 mg/s of Xe for a 560 mA anode current) to 33.4° in the collared HC mode and from 33.4° to 36.3° in the base and collar LC modes respectively. Conversely, we measure a slight bump in beam efficiency when the collar is attached. The measured ion beam current integrated up to a radius of 25 cm is $150 \pm 3\%$ and $154 \pm 11\%$ of the anode current for the baseline thruster in high and low current modes respectively while it is $166 \pm 8\%$ (HC) and $159 \pm 11\%$ (LC) for the collared variant. The actual beam efficiencies are of course less than unity, with the discrepancy expected to be due mainly to sheath expansion effects and collection of charge exchange ions at large radial distances.

Two-dimensional maps of the axially projected ion current were measured by a Langmuir probe for the baseline and collared thrusters respectively. It is clear from both that the axial ion current exhibits a local minimum along the thruster axis in the same location of the plasma potential valley, 3 cm downstream of the exit, and that the plume has detached from the magnetic field. The peak ion current does not appear to emanate from the origin of our coordinate system in either configuration but instead from some region around 10 to 20 mm off-axis.

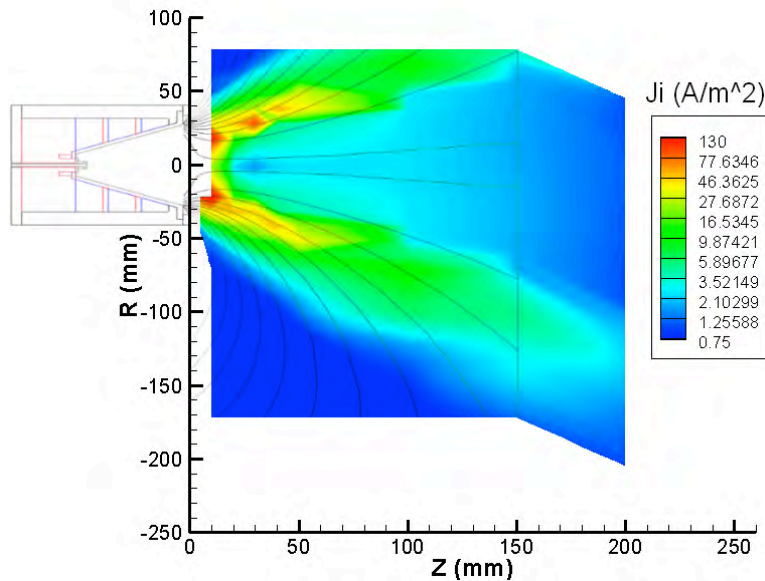


Figure 40. Axial ion current density measured in the baseline configuration operating at 400 V, 160 mA and 5 sccm of Xenon. Simulated flux lines overlaid.

A stable HC mode was obtained in the collared configuration by decreasing the keeper current from 1.5 A to the normal 0.5 A used in all baseline testing. The anode potential and flow rate were kept at the values used for LC mode characterization (400 V and 0.49 mg/s) but the anode current increased to 220 mA. The shape of the plume potential contrasts with that found in LC mode in the same manner as the two plumes compare visually: the HC mode is diffuse and looks the same everywhere up to a certain angle while the LC mode is sharply focused with easily discernible features. The

measured electric field is nearly perpendicular to the magnetic field lines only in the region near the thruster where the magnetic field lines turn upstream.

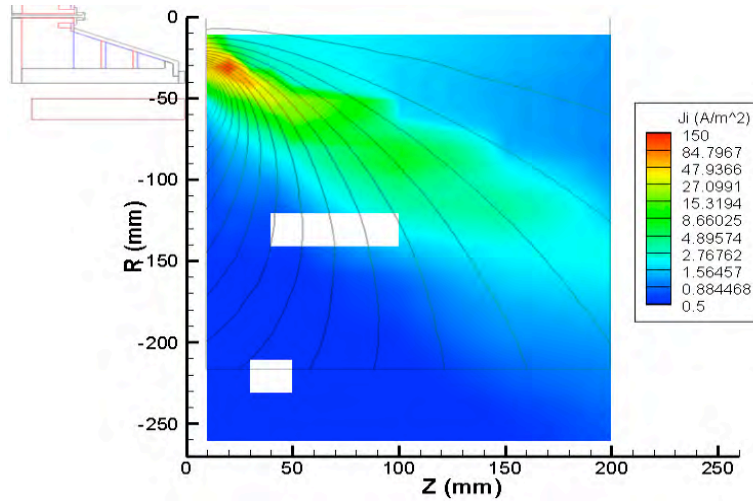


Figure 41. Axial ion current density measured in the collared configuration operating at 400 V, 160 mA and 5 sccm of Xenon. Simulated flux lines overlaid.

High spatial resolution scans were performed along the thruster axis in each of the two modes for further comparison and in an attempt to resolve the main acceleration layer of the thruster. For these scans the emissive probe was constantly heated by a 3.75A current to minimize probe dwell time in the plume. The plasma potential is taken as the maximum in the first derivative of the electron emitting I-V curves. Comparisons of this method with previously obtained measurements which find the intersection of hot and cold I-V traces showed discrepancies of usually less than 10V.

The two modes show very similar on-axis traits. Both retain roughly 72% of the applied voltage 5 mm downstream of the exit and reach a peak axial electric field between 10 and 12.5 mm past the exit. The main difference between modes is in the location and amplitude of the small potential valley near the exit. In HC mode the plasma reaches a local minimum of 41 V a distance of 22.5 mm from the exit before rising up to 56 V at 30 mm and heading back down towards 23 V. In LC mode that minimum occurs further downstream at around 34 mm and the voltages are much lower, going from a low of 14.5 V up to 15.2 V at 47.5 mm then down to less than 12 V. The fact that the main potential drop profile is the same in both modes, despite the drastically different time signature of the currents (nearly constant in the LC mode, violently oscillatory in the HC mode) is not understood at this time. The possibility has been considered of alternative ignition at two cusps, but one would then expect to see very different potential profiles (even when time-averaged) past the last ionization region. Perhaps these differences are not to be seen near the axis, and this should be further investigated.

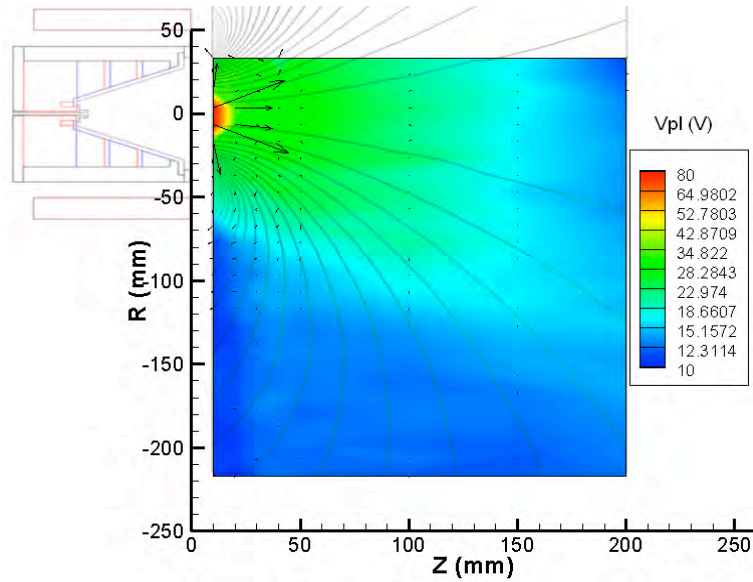


Figure 42. Plasma potential measured by emissive probe for collared DCFT anode operating at 400V 220mA and 5sccm of Xe w/ 0.5A keeper current. Calculated electric field vectors are plotted with length relative to magnitude. Simulated B field lines are overlaid.

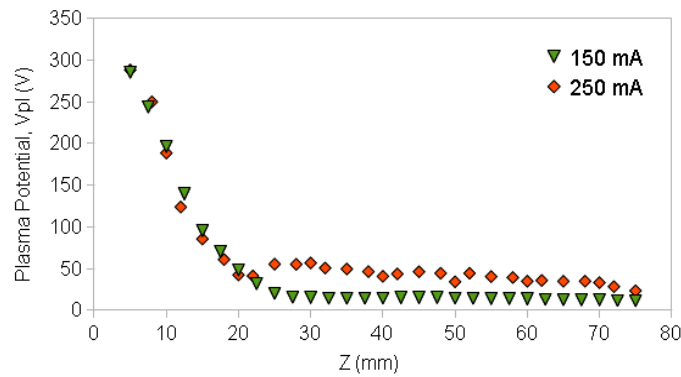


Figure 43. Plasma potential measured by floating emissive probe for collared DCFT anode operating at 400 V and 5 sccm of Xe w/ 0.5 A keeper current in HC (220 mA) and LC (150 mA) mode.

The measured electric fields exhibit large radial components near the thruster exit and in the wings of the plume where the diverging magnetic field has a stronger effect on the potential profile. The addition of an iron collar around the outside of the thruster served to reduce the magnetic field strength outside of the discharge chamber with the intent of lessening the radial electric fields set up there by diverging lines of magnetic flux. Contrarily, a slight increase in the ion beam divergence was observed. This may be due to the magnetic field lines peeling off from the axis closer to the thruster exit steering the electrons outward or from an increased radial electric field component at the acceleration region caused by the lower potentials found away from the axis. In

either case the effect of the magnetic collar on the thruster efficiency appears to be negligible.

10.2 Modifications intended to change the separatrix geometry

As discussed in Section 9, it is hypothesized that the separatrix formed by the radial and axial cusps closest to the cathode plays a larger role in determining the shape of the electric field than does the shape or strength of the magnetic field further from the exit. Electrons from the cathode congregate at the radial cusp near the thruster exit, where the majority of the ion acceleration occurs, and thus the line central to the cusp where electron density is a maximum is likely to play an important role in the development of the electric field. Subsequent experiments have since focused on alteration to the shape of this separating line.

An electromagnet was designed to alter the field at the thruster exit in order to test whether the shape of the magnetic field near the exit separatrix is a driving factor in plume dynamics. A positive choke magnet current was shown, both through simulations and Gauss probe measurements to bend the exit separatrix towards a more purely radial (less convex) shape. Faraday probe measurements in the plume showed that as a result a portion of the plume, normally peaked around 30° off axis, is now found at angles approaching 20° . The formation of two distinct peaks in the radial ion current profile is seen both through measurements and visual inspection of the plume, with the inner peak constricting towards the thruster axis as the choke magnet current is increased. This stratification of the plume is observed in both HC and LC modes.

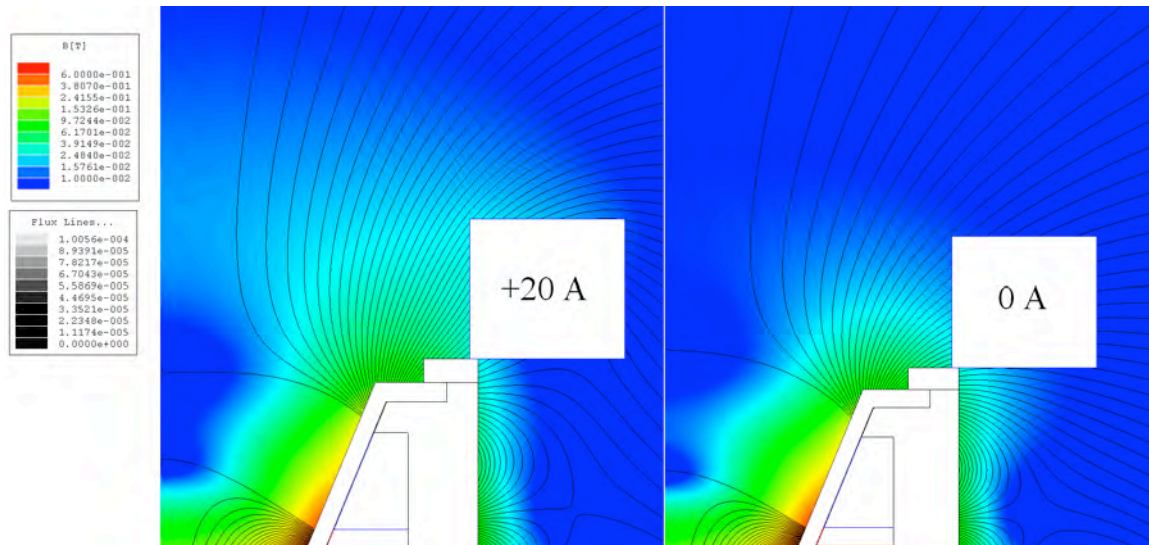


Figure 44. Simulated magnetic field of the DCFT with an external choke coil energized to 20 A (left) and 0 A (right) showing the change in field strength and flux line shape

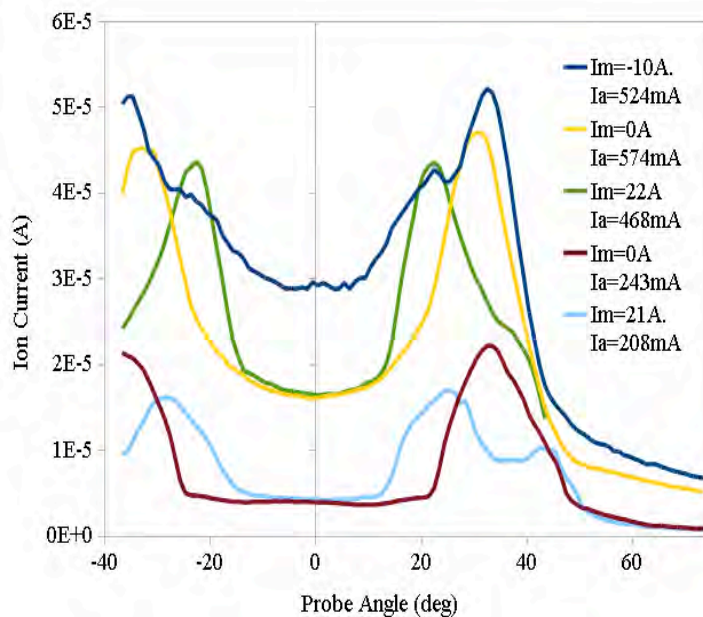


Figure 45. Ion saturation current vs probe angle wrt thruster axis 30 cm from exit for various choke magnet currents (I_m) and resulting anode currents (I_a). Thruster is operated at 300 V with either 7 sccm of Xe for HC mode ($I_a > 450\text{ mA}$) or 6 sccm for LC mode ($I_a < 250\text{ mA}$).

The external magnetic field strength is actually increased in order to flatten the exit separatrix which results in a decrease in the anode current with choke coil current. When the field becomes too strong the thruster begins to operate erratically and often jumps to much larger anode currents. The precise strength of this peak field (or peak choke coil current) has been seen to decrease as the anode voltage is raised. It is also noted that at low voltages the anode current decreases almost linearly with choke coil current, while at higher voltages the curve appears linear at low currents, with diminishing effects as the current increases past a certain point. The high degree of anode current throttling available with choke coil current underscores the importance of the exit field in impeding electron flow to the anode.

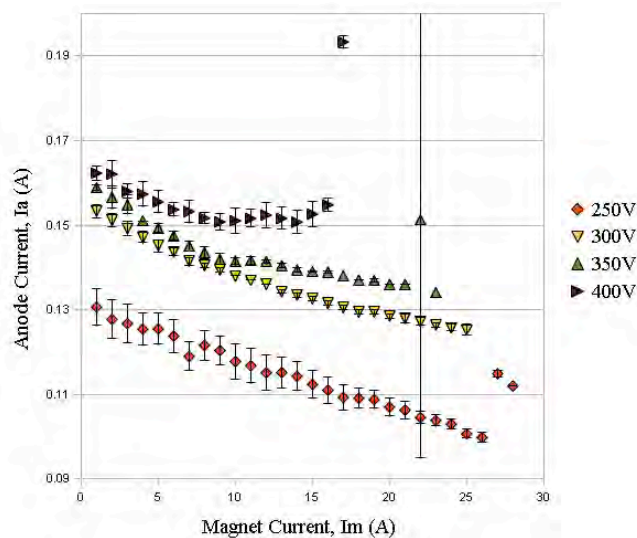


Figure 46. Thruster anode current vs choke coil current (i.e. exit field strength) at various values of anode voltage

Initial measurements made by a Retarding Potential Analyzer (RPA) have indicated that the reduction in plume divergence may come at the price of ion acceleration efficiency. Although a peak in ion energy per charge is still seen a few tens of volts below the applied potential, in the high choke coil current case, a much stronger peak develops at around half the anode voltage. Ion energy data exist for only one thruster condition at this time, however, and a further investigation of the conditions which favor this low energy mode is required before we can begin to draw any conclusions. A map of the near-field plasma potential evolution with the magnetic field is also planned, which should help shed some light on the interplay between the magnetic field shape and strength and the formation of a self-consistent electric field in the plasma.

11. Insulator erosion data

Erosion of the dielectric insulator during a 204 h test of the DCFT was measured and results will be reported in this section. A paper detailing these results is also in preparation at this time (Ref. 31]). The thruster operated at an anode power of 165 W. Unlike most Hall thrusters, the lifetime was not found to be limited by erosion near the exit plane, due the positioning of the permanent magnets. Additionally, the maximum erosion rate is found to be lower than rates measured in the BHT-200 by at least a factor of two. The lifetime for this laboratory prototype is estimated to be 1220 h, based on the time needed to erode through the insulator in one of the ring-cusps. This suggests that future designs could easily be made more durable by fortifying the cusps with additional insulating material.

Performance measurements during the test indicated decreased thrust and anode efficiency compared to previous measurements. A concurrent analysis of deposition within the thruster shows the accumulation of conductive and ferromagnetic elements between cusps, probably originating from the stainless steel frit that was used as the injector surrounding the anode. This deposition is identified as a possible cause of performance degradation over time, though additional measurements will be necessary to confirm this hypothesis.

These tests were conducted in Chamber 1 at the Edwards AFB AFRL Space Propulsion Branch. The anode voltage and xenon flow rate were 300 V and 8.5 sccm. This operating condition was selected because the anode power is thought to be low enough to avoid excessive heating of the permanent magnets. Ion velocity and performance data at this condition are also available. Operation in the low-current mode was attempted, but could not be maintained, consistent with previous testing in Chamber 1 to measure ion current densities and energies in the plume. The cathode potential floated with respect to ground, and was positioned identical to previous studies. Throughout testing, the chamber pressure was 2-3 μ Torr. Anode current values remained between 0.53-0.56 A from hour 5.5 until the end of testing. Over the same interval, the floating cathode

potential, relative to chamber ground, began at -16 V and slowly increased to -12 V. The cathode keeper voltage remained between 11-13 V with the aid of a constant 3 A heater current.

The profile of the insulating HP BN cone was measured before and after the long duration test. An overview of the measurements is given in Figure 77, showing the locations of maximum erosion relative to the permanent magnets and insulator. Erosion is limited to the immediate vicinity of the cusp locations in C1 and C2. Closer to the exit plane, erosion begins near C3 and continues toward the exit plane. From these two profiles, the average erosion rate was calculated based on the distance perpendicular to the cone surface. The results are shown in Figure 48. For this plot, the erosion rate is plotted at the radial coordinate of the "before" scan. The slope of erosion data between cusps is due to a misalignment of 0.25° , very close to the precision of the level used to position the thruster for measurements.

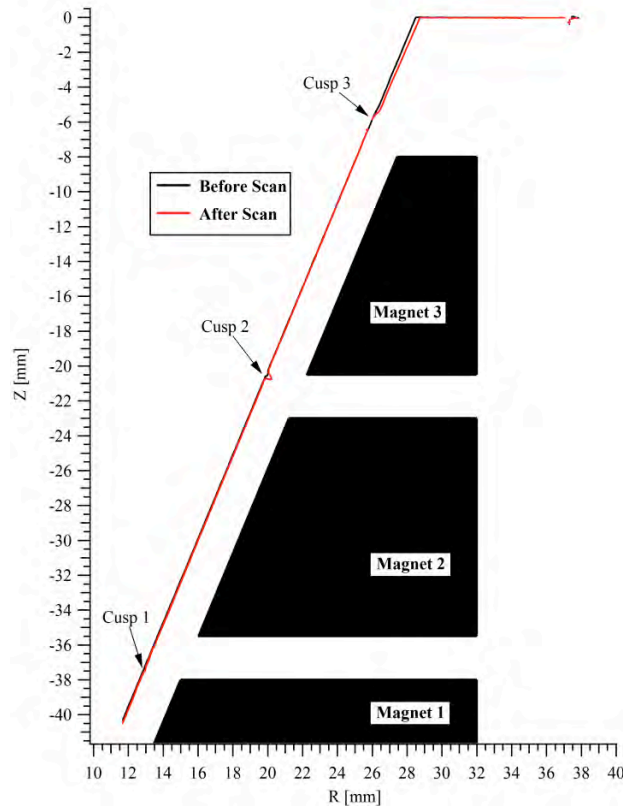


Figure 77: Profilometry measurements before and after 204 h of operation. Magnets are numbered in their order downstream of the anode. The exit plane of the thruster corresponds to $z = 0$. Measurements were limited to just upstream of C1, due to the angle of the incident beam of light and more specular reflection of incident light closer to the anode.

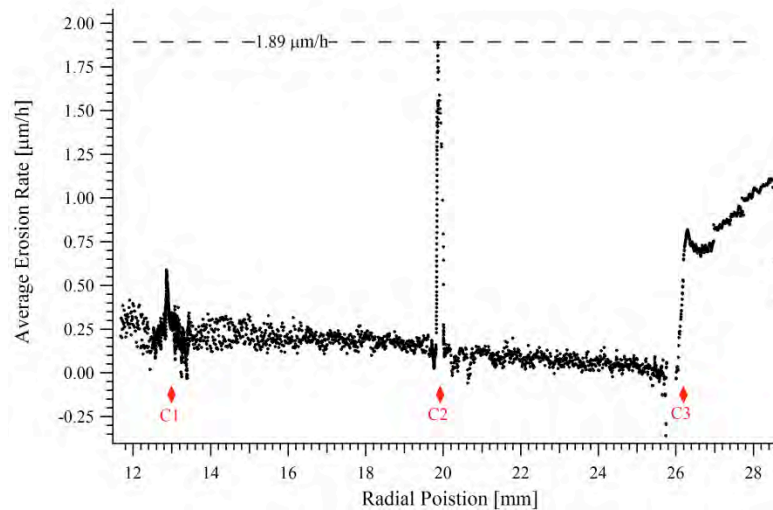


Figure 48: Average erosion rate during the 204 hours of operation. The locations of the cusps along the wall are indicated by the red diamonds.

The peak erosion rate is in C2, rather than at the exit plane as observed in Hall thrusters, with a maximum average value of $1.9 \mu\text{m/h}$. The first and second ring-cusps coincide with regions of increased erosion, while C3 is roughly where erosion at the exit begins in the downstream direction along the thruster wall. Erosion rates increase toward the exit, but never exceed the erosion rate measured in the second cusp. The initial thickness of the insulating cone is 2.5 mm in the radial direction, allowing for an effective insulation lifetime of 1220 h. This lifetime is calculated assuming a constant erosion rate in the second cusp. Many Hall thrusters continue to operate after the insulating ceramic is unable to completely shield the magnetic circuit. This is appropriately referred to as a "soft failure" [Ref. 32] in situations where a satellite and thruster can continue to function within specifications after the insulator has been compromised.

A comparison of beginning-of-life (BOL) erosion rates and thruster lifetimes determined from measurements in low power Hall thrusters is provided in Table 3. A distinction is made between the predicted lifetime of a thruster, and the time at which soft failure is reported or predicted to occur. No erosion measurements in cylindrical Hall thrusters are available for comparison.

Table 3: Survey of low-power Hall thrusters for which lifetime and performance data were found in the literature. The listed soft failure time indicates the point during testing the insulating ceramic failed, or was predicted to fail. The predicted lifetime is the reported or demonstrated operational lifetime of the thruster. The references for this survey will be provided in the paper these results will be published in.

Thruster Designation	Anode Power	Max. "BOL" Erosion Rate	Insulator Material	Soft Failure	Predicted Lifetime	Operational Chamber Pressure
----------------------	-------------	-------------------------	--------------------	--------------	--------------------	------------------------------

	[W]	[$\mu\text{m}/\text{h}$]		[h]	[h]	[μTorr]
SPT-50	320	-	borosil	>2,500x	-	50-100
KM-45	310	4.1	-	3,500-4,000	-	10-20
KM-32	200	5.2	HP BN	2,000-3,000*	3,000	23, 12
BHT-200	200	3.8	HBC BN	1,287-1,519	>1,700	2.2
HT-100	175	9	60/40:BN/SiO ₂	300	1,500**	7.5
MIT DCFT	165	1.9	HP BN	1,220	>1,220	2-3
SPT-30	150	-	borosil	600 x	-	-
SPT-20M	<100	-	alumina w/ additive	594-910	4,000	24

x Details of lifetime test or methodology not found in reviewed literature

* Center pole is measurably eroded before hour 500 of testing

** Predicted lifetime is at 100 W, rather than the tested 175 W condition

- Indicates data not found in reviewed literature

Deposition on the cone surface during operation was also significant. The middle and right photos in Figure 49 show photographs of different areas of the cone surface after the test was completed. These photos should be compared to the photo on the left in Figure 49 to observe the difference in the appearance before and after the long duration test. The coloring of the deposition is lightest near the porous 316 stainless steel diffuser behind the anode up until the first ring cusp. Downstream of C1, the deposition is mostly darker, with the exceptions of some areas that are lighter grey or white in between cusps. The direct source of these previously unseen patterns is not known, but they exhibit rough symmetry with respect to the cathode location. A sample of the deposition was scrapped off and analyzed using energy dispersive x-ray spectroscopy. Localized samples were not taken, preventing the examination of compositional

variations between different areas of the chamber. A sample of deposited materials on an external surface was also analyzed. The composition of the internal deposition contained copper, constituents of 316 stainless steel and additives commonly used to lower the work function of tungsten in hollow cathode emitters. The exterior sample was composed entirely of copper, tin and other components common to copper alloys. The thrust stand the thruster was mounted on is likely the source of copper identified in both deposition samples. The large amount of iron on the interior is likely sputtered from the annular porous stainless steel disc located behind the anode. The diffuser disc is visible in all photos in Figure 49. It is recommended that, before future tests of the thruster using the 316 SS diffuser, the surface of the insulator be lightly sanded to remove the dark deposition throughout the interior of the chamber.

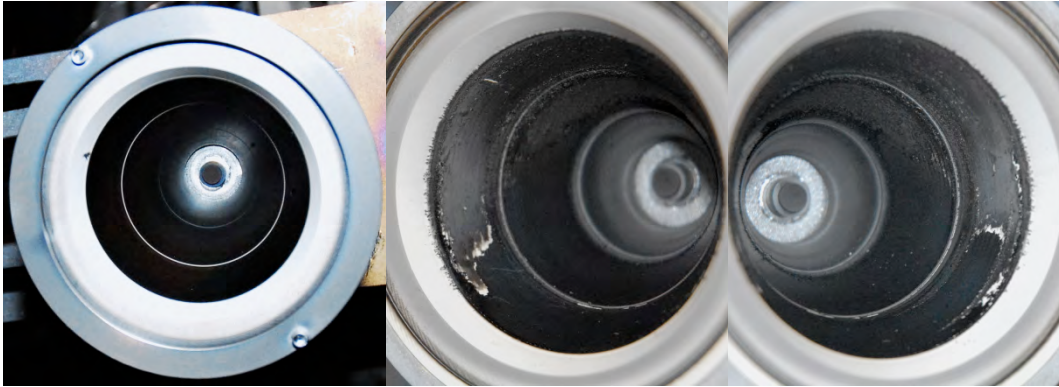


Figure 49: Left: The thruster after 65-70 h of operation, but before the start of the long duration test. The photos in the middle and on the right show the DCFT after the long test. Regions with erosion are evident as bright white rings. The uneven, but somewhat symmetrical pattern of deposition is also visible. The cathode was located above the thruster in these pictures, and to the left of the thruster in the left-hand photo.

The width of the erosion features in each cusp can be characterized by the full width at half maximum (FWHM) of the eroded distance during testing. The FWHM of plasma escaping (δ_ϕ) confinement provide by magnetic cusps has been found to scale as $\propto R^{1/4}$ experimentally and theoretically, corresponding to the hybrid Larmor radius (see Ref. [12,13], plus Refs. [33,34]). The ion current density loss width (δ_j) can be approximated as δ_ϕ because the ions are electrostatically confined by the electric field that arises due to the stronger confinement of electrons in the magnetic field.

The erosion rate (ξ) is equal to the product of the ion current density at the wall (j_{iw}) and a volumetric erosion coefficient (S_ξ) that depends on the angle of incidence and ion energy. Neglecting the angular variation of ion impacts, the distribution of S_ξ within cusps near the wall is a composite function of the spatial variation of ion energies and the dependence of the yield on the ion energy. The peak energy of ions impacting the walls can be calculated for a given near-wall electron temperature from the sheath potential drop ($\Delta\Phi_s$), because the pre-sheath structure along a separatrix is very similar to the standard case in the absence of a magnetic cusp [Ref. 14]. Scaling these energies as a Gaussian distribution centered about the separatrix, with the same FWHM as j_{iw} , allows the FWHM of S_ξ (δ_ξ) to be calculated. The maximum erosion rate and width of the

erosion feature are measured quantities, so this model allows for the near wall electron temperature to be solved iteratively, as well as the peak value of j_{iw} in the cusp. Using the energy dependence of S_{ξ} provided by Yim [Ref. 35] for the low energy sputtering of BN by Xe ions, some of the estimated plasma parameters based on this method are shown in Table 4. This model explains why the erosion features in the cusps are much narrower than the extent of the cusp at the wall or the ion Larmor radius.

Table 4: Estimates of ion current density and electron temperature near the wall, based on measured widths of erosion features in each cusp.

		C1	C2	C3
δ_{ξ}	[mm]	.15	.25	.61
B	[G]	4560	4420	1590
T_e	[eV]	6.7	24	21
$\Delta\Phi_s$	[V]	29	29	25
S_{ξ}		2.3	4.6	3.1
j_{iw}		71	115	74
δ_{ϕ}	[mm]	.35	.50	1.3

Surprisingly, the largest erosion rate is measured upstream of the ring cusp near the thruster exit plane. The thruster was operated in high-current mode, meaning that the estimates shown in Table 4 must be interpreted as time averages. High-speed digital videos show that the instability inherent in the high-current mode is accompanied by a marked increase in luminosity from the plasma upstream of the exit. One possible interpretation of these observations is that an ionization avalanche is quickly initiated throughout the thruster, ionizing a large portion of the neutrals. This argument is in agreement with another observation - that the utilization efficiency of the MIT DCFT is closer to unity in the high-current mode than the low-current mode, contrary to intuition. Ions born during this burst of ionization are more easily lost to the second cusp than ions created near the exit because of the potential valley present in the second ring-cusp. This particular cusp occupies the largest volume in the interior of the

thruster chamber. The current understanding of the oscillatory mode is further discussed in Section 13 of this Report.

12. Oscillations and fast photography data

12.1 Anode Current Waveform Measurements

In the first investigation of these thrusters, two distinct modes of operation were identified. At lower anode voltages, the plume is seen to have a diffuse appearance. For a fixed flow rate, increasing the anode voltage above a threshold value is accompanied by a sharp drop in anode current (I_a) and changes to the visual appearance of the plume. This second mode is therefore referred to as the low-current mode. The mode with the more diffuse plume is referred to as the high-current mode, due to its larger average anode current. Later, during tests to measure plume properties at the Edwards AFB AFRL, discharge oscillations with magnitudes several times larger than the average current were discovered to be present in the high-current mode [Ref. 14]. Transitions to the low-current mode reduced the oscillation magnitude by an order of magnitude or more. Furthermore, the intermittent onset of large-amplitude spikes in I_a during low-current operation was observed prior to transitions into the high-current mode. A more detailed examination of these modes was carried out at the MIT Space Propulsion Laboratory by recording time resolved, AC-coupled anode current waveforms, and high-speed digital videos of the thruster operating in both modes, and was reported in Ref. [36].

The sensitivities of oscillation characteristics to operating conditions were examined by varying one variable, such as anode voltage (V_a), while keeping others fixed. Aside from the average values of I_a , the frequency, magnitude and rise/fall times of anode current oscillations were also recorded, where applicable. Three parametric sweeps examined the effects on these quantities: the anode mass-flow rate (\dot{m}_a), V_a , and chamber pressure were varied as shown in Table . Throughout these scans, the cathode conditions were left unchanged. The cathode mass-flow rate was 1.5 sccm, the keeper current was 0.5 A, and the keeper voltage ranged from 14.7-15.9 V. Sweeps of the cathode mass-flow rate did not significantly alter either the average I_a values, or the oscillation characteristics. In some instances, increasing the keeper current (I_k) causes the thruster to switch from high-current to low-current mode. However, the currents required to do so are large enough to inhibit extensive testing of this sort, out of concern for maintaining the cathode in an operational state.

Table 5: Operating conditions for the three scans completed for the purpose of examining effects on anode current oscillations. The standard deviation of a value is provided if greater than 1% of the mean

value. The duration of the scans were between 130-200 min to allow the thruster to warm up as anode power increased. Temperature trends were monitored using an un-calibrated thermocouple positioned between the insulating cone and the permanent magnet between the first and second cusps.

Scan Type →		Anode Flow	Anode Voltage		Chamber Pressure	
Anode Voltage	[V]	250	250-450		250	200
Anode Flow, Xe	[sccm]	3.5-10.0	6.5	8.5	4.0	5.0
Chamber Pressure	[μ Torr]	13.6-34.1	21.0	27.7 ± 0.5	18.4-41.7	

The clearest trend in the oscillation frequency comes from the variation of the anode flow rate, shown in Figure . A possible explanation of the observed increase in the high-current oscillation frequency is that the neutral refill timescale decreases as the anode flow, and hence anode current, increases. An increase in anode power leads to greater heat loss to the thruster, and hence a larger thermal speed for the injected xenon as the neutral temperature increases. Neutral speed estimates were made by subtracting the doubling and halving times, shown in Ref. [36] (also in Figure 53) from the measured oscillation period, and equating the difference to the neutral fill time (τ_{fill}). A characteristic length of 5 cm was assumed, which is approximately equal to the distance from the neutral injector to the thruster exit. Based on this argument, the injected neutral speed (V_n) would vary from 140 m/s at a flow of 4.5 sccm up to 230 m/s at a flow of 10 sccm. Taking these speeds as the neutral thermal speeds suggests that the injected neutral temperature increases by about 550 K from the beginning of the scan to the end (or a factor of 2.7). The anode power was approximately 40 W and 250 W, respectively, at these two flow rates. Although V_n increases with \dot{Q}_a , the neutral density still rises as the anode flow goes up. These points are further discussed in Section 13.

When examined in detail, the so-called High-Current mode turns out to take different forms, depending on the flow rate for a fixed voltage. All the points with flow rates of 8.5 sccm or greater have strongly peaked current traces like the one shown in Figure (a). Then in going from 8.5 down to 8 sccm, the waveform takes intermediate shapes, with a mixture of strong peaks and progressively more stunted peaks. When the flow reaches 7 sccm, the current trace finally takes the form of Figure (b). Interpreting the data requires attention to how the frequency for each point was determined. The selected frequency corresponds to the peak magnitude in the discrete Fourier transform (DFT) of the anode current waveform. This method is vulnerable to misleading data when the zero frequency of the DFT dominates, or if a lower frequency develops in the signal with a slowly varying magnitude. It was decided to plot the frequency with the largest value in frequency space, but this does not mean that that frequency is the fundamental harmonic of the signal. This can make it appear that the

dominant frequency of the signal has been halved or doubled, when really the difference between the two situations is similar to the differences between the current traces in (a) and (b) of Figure .

The mixing of the peak shapes brings about the lower fundamental frequency due to the fact that every other peak is no longer spiking as strongly. With this lower harmonic emphasized in the DFT, it is possible for the plotted value to suddenly decrease by factor of two, which is the case of the outlier point in the anode flow scan at 6.5 sccm in Figure . A peak in the DFT remains near 3 kHz, but a new frequency overcomes it by a slim margin. It is necessary to realize that the dominant frequency component can be halved without a dramatic or particularly noticeable change in the current trace.

Though not plotted here, the pressure scan indicates that the oscillation frequency is not strongly dependent on chamber pressure over the range of pressures tested here. Cases for which no clear frequency was dominant or could be discerned were not assigned a frequency value. This most often occurs when the thruster is in the LC mode. Within each mode, the frequencies do not change significantly with anode voltage, similar to the expected behavior of large amplitude oscillations in Hall thrusters [Ref. 37].

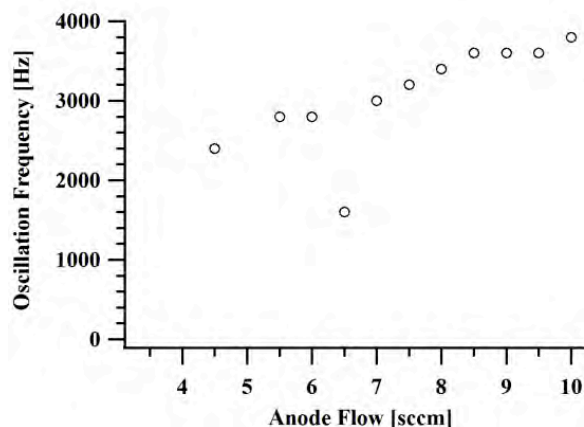


Figure 50: The oscillation frequency increases with anode flow rate. The plotted frequency corresponds to the peak magnitude of the DFT of the current waveform.

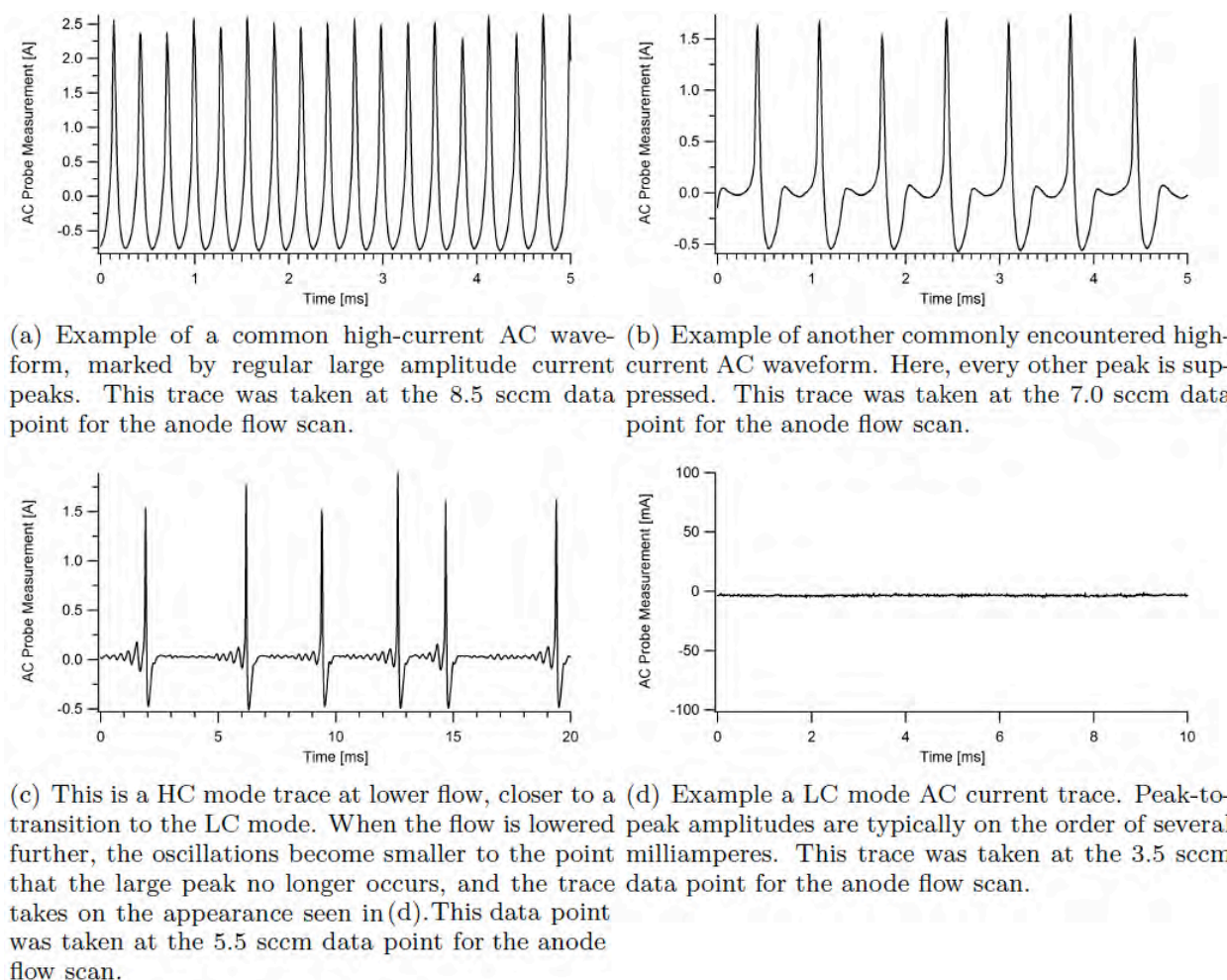


Figure 51: Different AC waveforms encountered during the anode flow scan.

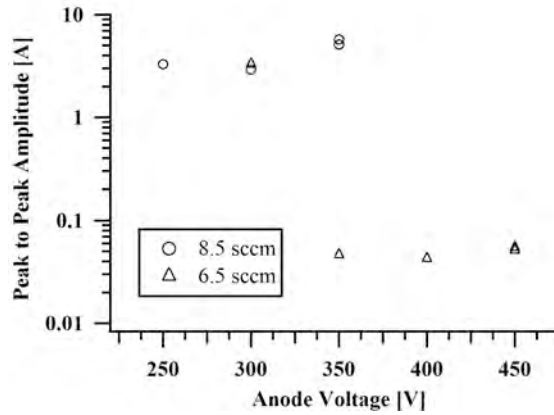


Figure 52: Dependence of discharge oscillation peak-to-peak magnitude on anode voltage.

Data from the parametric scans show that the peak-to-peak oscillation amplitude varies weakly with thruster operating condition in a single mode and confirms that it differs dramatically between modes. In Figure 52, the amplitude decreases by a factor of approximately 100 when going from HC to LC mode. A similar *increase* in magnitude was observed during the anode flow scan when \dot{Q} increases from 3.5 to 4.5 sccm, switching modes in the opposite sense.

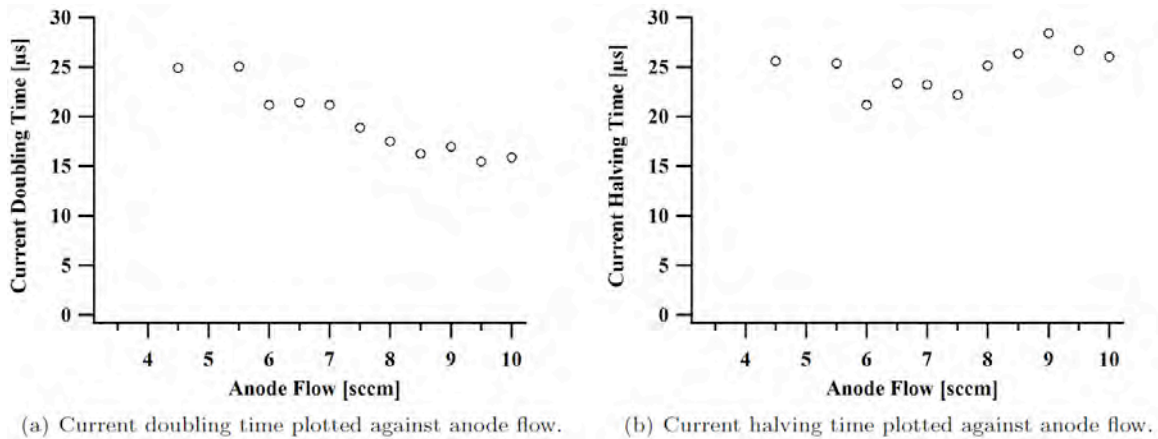


Figure 8: The doubling time decreases with anode flow, while the halving time exhibits no clear trend.

Figure 53 is representative of the anode flow and voltage scans, in that they both have shorter rise (doubling) times than fall (halving) times. Increasing the anode flow decreases the rise time in a seemingly linear fashion, while the fall time remains effectively constant. The doubling and halving times have nearly identical values in measurements made during the pressure scan in the HC mode. However, in the UHC mode, (at very high chamber pressures, see below) the doubling and halving rates both increased during the pressure scan. No definitive trend between these times and anode voltage were discernable.

Chamber pressure scan data show no discernable frequency trend within modes. However, excessive chamber pressures caused the thruster to switch into a third mode. This mode is accompanied by a visual change in the plume, from the typical blue-green color, to a tint of red. The oscillation amplitude drops similar to when the thruster enters the LC mode, though the average value of I_a does not always decrease, and even increases above the values

observed in HC mode. For this reason, the mode has been called the ultra-high-current (UHC) mode. The thruster is typically unstable in this mode, jumping between the HC, LC and UHC modes. The results of the pressure scan suggest that the UHC mode should be taken as an indication that facility effects are playing a dominant role in the operation of the thruster. The threshold for this situation appears to be in the 25-30 μ Torr range, though this appears to depend somewhat on the anode flow rate.

Repeating these measurements in a chamber capable of operating at lower pressures could determine if any changes between the HC and LC modes can be initiated in repeatable manner, and also shed more light on the influence of the facility on the mode of thruster operation. Magnet temperature recordings indicate that operating at lower than 200 W is a good indicator that the magnet temperature is likely to be less than the manufacturer quoted maximum operating temperature of 300 °C.

12.2 High-Speed Digital Video of DCFT Operation

High-speed digital videos were recorded using a Phantom SA5 camera. The Phantom SA5 records black and white images, so to increase visual contrast between regions, the color of each pixel was changed to represent its intensity. In some instances, the plasma is bright enough to saturate the image, so any real variations of intensity within these regions do not carry over to the recorded image. Also, the scale on which pixel intensity is expressed can change from one recording to the next, based on camera settings, lens aperture, and other factors.

A small sample of frames showing the DCFT operating in the HC mode is shown in Figure. The first frame shows the end of a previous luminosity burst, the second frame shows the plasma during the peak in anode current, and the third frame represents the end of the luminosity burst visible in the second frame. At the start of an oscillation, when the images are the dimmest, the luminosity is localized near the anode and the first magnetic cusp. As this region brightens and eventually peaks in intensity, an annulus of luminosity becomes visible in C2. This distribution of luminosity is in agreement with the appearance of the thruster in real time when operating in HC mode. The average visual appearance of the plasma is brightest near the anode with bulges of plasma luminosity centered about the thruster axis of symmetry apparent in C1 and C2. The luminosity in C2 has an annular shape. It is important to keep in mind that the luminosity has strong contributions from ions and neutral atoms. Spectroscopic measurements show that neutral emission is greater than ion emission in the both modes [Ref. 19]. The intensity profile of pixels in time has a similar shape to a commonly observed anode current oscillation in time, an example of which is in Figure (a).

Videos were also recorded with the intent of examining luminosity dynamics at the exit of the thruster during HC mode operation. During the peak in luminosity, an interesting feature is visible in the frames shown in Figure 9. A bright cloud is seen forming at the thruster exit, and then moving downstream out of view. To further examine this traveling luminous object, the time varying intensities of three pixels in the plane of the thruster axis were sampled and are shown in Figure 10. A conspicuous peak in intensity is revealed when the observed

intensity scale is narrowed, showing a distinct shape moving downstream almost too quickly for the 100 kHz frame rate to resolve. By estimating the distance traveled perpendicular to the viewing axis of the camera, as well as bounding the angle at which the wave front is traveling with respect to the thruster axis between 0° and 30° , the wave peak progresses away from the thruster at about 5-10 km/s. These values are better classified as an order of magnitude estimate, due to the large uncertainty in the distance traveled between pixels, and the fact that the intensity of a given pixel depends on the line integral of emission along its viewing path. This luminosity wave occurs at the end of a HC mode spike in anode current, and may therefore be a manifestation of low energy ions leaving the thruster at the Bohm speed. The time scale for ions at these speeds to exit the thruster is 5-10 μs , which is of the same order as the fall time observed in time-resolved measurements of the anode current waveform, shown in Figure 8.

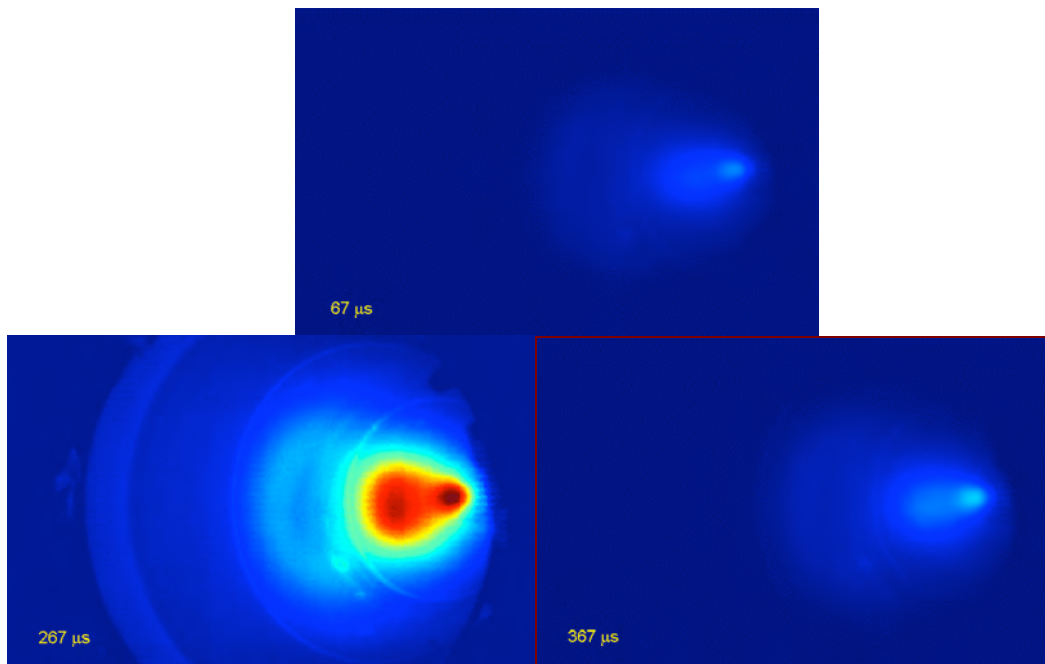


Figure 54: Selected frames from a high speed video of the DCFT operating in the HC mode. The anode voltage is 180 V with a xenon flow rate of 7 sccm. The frame rate is 30 kHz. The number on each frame is the time stamp of the image. This view puts the viewing axis nearly parallel with the thruster wall, which is at an angle of 22.5° from the thruster axis.

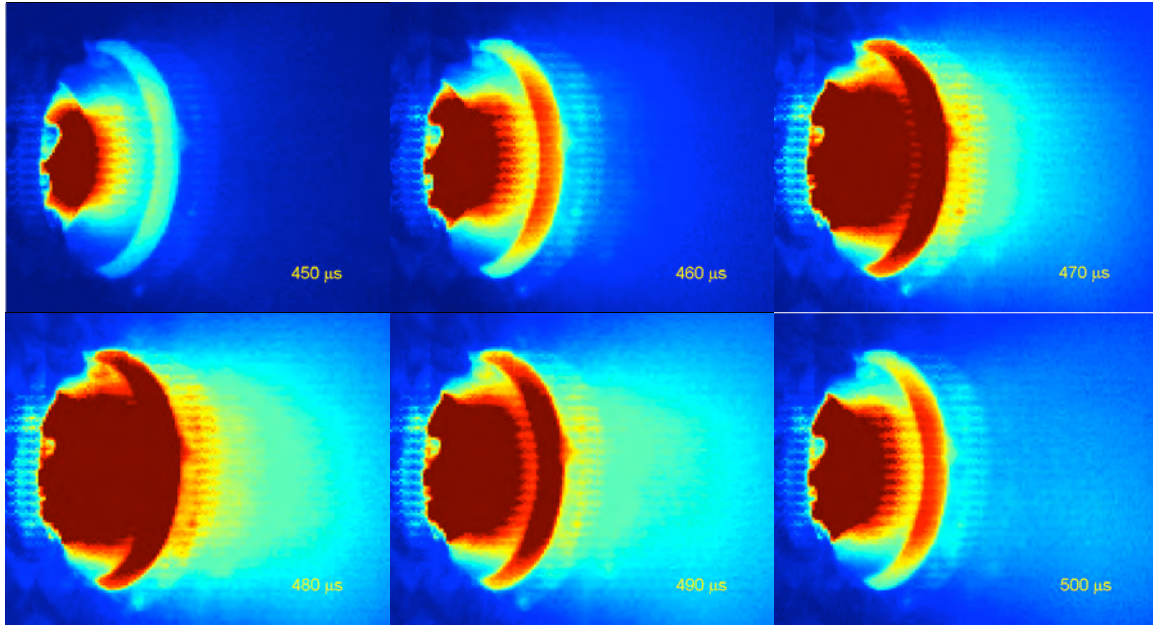


Figure 9: The sampling and video frame rate is 100 kHz. These frames capture a luminosity wave exiting the thruster during operation in the HC mode. The thruster operating condition was set to a 300 V anode voltage with an anode flow rate of 7.5 sccm xenon. This view is perpendicular to the view in Figure, and shows the luminosity at the exit of the thruster.

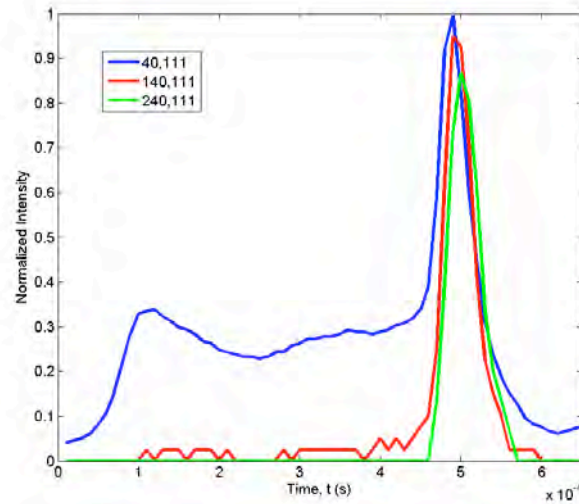


Figure 10: Selected pixel intensity, showing a traveling wave of luminosity leaving the thruster.

Videos of the thruster operating in the HC mode showed no discernable azimuthal luminosity variations. The oblique viewing angle shown in Figure 54 is not ideal for examining azimuthal features, though it is worth noting that the plasma was visually uniform in the azimuthal direction at frequencies as high as 525 kHz. A different camera, constrained to record at lower frequencies, was used to record time resolved images with the viewing axis coincident with the thruster axis. These images, recorded near a frequency of 6.6 kHz, show axi-symmetric intensity contours centered about the thruster anode, shown in Figure.

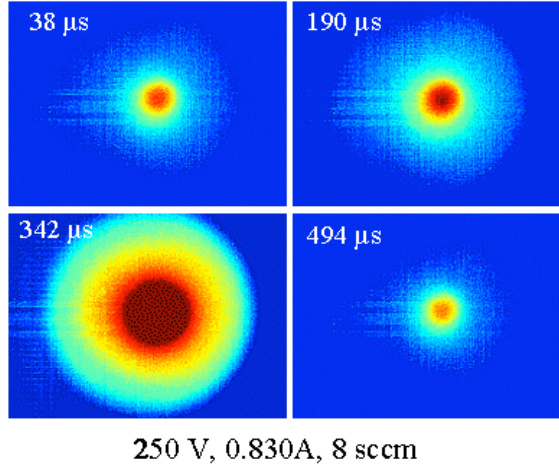


Figure 57: The anode voltage, current, and flow rate are given at the bottom of the figure.

12.3 Time Resolved Internal Probing

The work reported here is unpublished at this time. Attempts were made to use the internal probes in our custom-machined BN cone to measure time resolved ion fluxes and plasma potentials at the walls. Initial measurements were of the floating potential taken simultaneously from all the wall-flush probes. Unfortunately, the data suffer from a data acquisition phenomenon known as ghosting due to the high input impedance and high sample rates. A subsequent experiment measured the temporally-resolved ion saturation current from probes by connecting them individually to a simple biasing and measuring circuit comprised of batteries and a resistor. The data are interesting but do not seem to be indicative of the normal thruster conditions due to the visually obvious distortion of plasma-wall interactions caused by the probes. It is currently suspected that the deposition over time of a thin, conductive layer of steel on the BN cone as well, as the exposure of the thinly insulated probe lead wires to plasma downstream of the exit, may combine to distort the characteristics of several, if not all of the probes. Future use of the wall-probe instrumented cone will require sanding off of the conductive film from the channel walls along with a more robust form of insulation for the probe leads where they exit the cone.

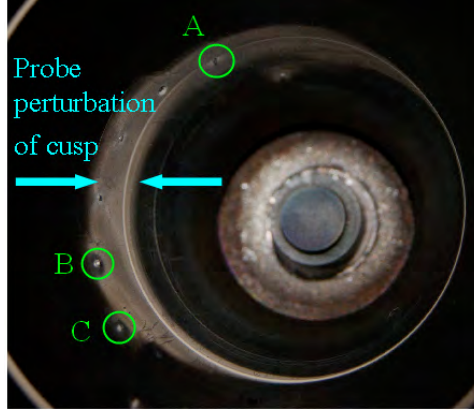


Figure 11: Close-up image of the discharge chamber and anode. The normally white BN cone is covered in black deposition except in the regions of high ion impingement. Probes A, B, and C are labeled for reference.

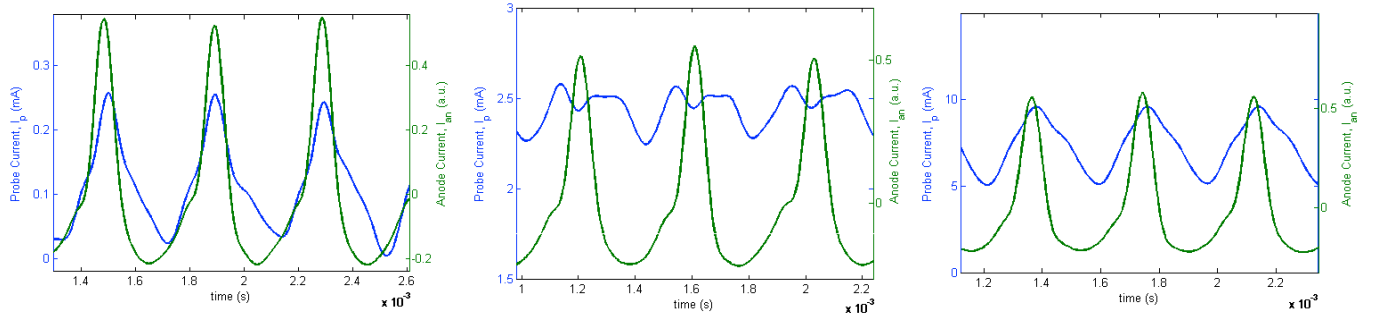


Figure 12: Anode current and wall probe ion current waveforms for probes A (left), B (middle), and C (right).

13. Discussion of oscillatory mode

Given our incomplete data set, we can only draw some plausible inferences about the complex physics occurring during the deep oscillations in the high-current mode. Data such as those in Figure 51 provide some significant evidence, and will be interpreted first. In Figure 51(a), the repeated high-current spikes are spaced by 0.27 ms. The distance from the gas injector to the center of the last separatrix is 50 mm, and if the time interval is interpreted as a convective time, the implied speed is 185 m/s, which is about the speed of sound in Xenon at 320 K. This makes it likely that this time interval can be viewed as the neutral re-fill time of the chamber after near-total ionization during the previous pulse. The implication is then that no significant ionization takes place until the last separatrix vicinity is again populated by both, electrons (which continue to arrive from the cathode), and neutrals. Once this condition is met, either ionization is resumed at a steady rate, and we have a period of operation resembling that of the Low-Current mode, or the ionization rate runs away as an avalanche that quickly consumes most of the neutrals in the part of the volume that is magnetically available to electrons. What exactly determines which of these outcomes happens is not currently understood. The pattern shown in Figure 51(a) is an example of the avalanche type, as one new pulse occurs regularly after one re-fill time. The pattern in Figure 51(b) indicates a situation where after one re-fill time ionization resumes at a rate only slightly higher than that necessary for steady operation; the slight excess appears to partially deplete the neutrals, and after a second re-fill time, conditions are somehow favorable for an avalanche. It may be that the difference between conditions after the first and the second refill times has to do with the gradual arrival at the separatrix area of neutrals from the inter-cusp annular regions not available to electrons, that were left behind after the previous ionization avalanche. At the even lower flow rates of Figure 51(c), nearly steady ionization prevails for several refill times, but eventually an avalanche is still triggered. Even lower flows, as in Figure 51(d), preserve the steady conditions indefinitely.

The issue of how and when the avalanche is triggered is still unclear. A simple argument based on the need to reach a critical value of the “reduced field” E/n would indicate that lower flow rates (and hence lower densities) would favor avalanche triggering, which is the opposite of what is observed. On the other hand, a known effect of increasing the gas density is to increase the electron scattering rate across B-lines, and it is plausible that at some density enough electrons from the downstream ionization area can flow upstream and start a rapid ionization cascade near the anode, that in almost zero time consumes all neutrals in the spindle-shaped accessible region. These two effects may not be mutually exclusive, and in fact, the triggering condition may involve satisfying both criteria: (a) A sufficiently high reduced field, and (b) A sufficiently high cross-field scattering rate. This may help explain the observation that the Stanford cylindrical design, in which the exit density is several times higher than in the MIT DCF, operates in the steady Low-Current mode only.

When an avalanche does occur and the central portion of the thruster is largely depleted of neutrals and filled with a highly ionized plasma, the newly produced electrons start draining into the anode, and this is in fact the observed current pulses seen in Figure 51. It is likely that the rate of electron collection by the anode is actually paced by the comparatively slow rate of ion emission into the plume, since neutrality conditions must prevail throughout. As plasma is thus eliminated in times much shorter than the neutral refill time, one might expect that a purely Coulombic potential distribution would eventually prevail inside the thruster; this is unlikely, however, because a sheath thickness of the order of 1 cm implies extremely low plasma densities, (of the order of 10^{12} - 10^{13} m⁻³), which are not realized. Thus, a more likely scenario is an in-situ reduction of plasma density, with a more-or-less constant geometrical distribution. This appears to be what is indicated by the photographic evidence in Section 12.2, although it is not easy to separate the effects of varying intensity and varying geometry in these pictures.

The time profile of the current pulses is another complex issue with several aspects involved. As noted, neutrality must be maintained, and so, of the two processes, ion emission and electron collection, the slowest one must actually be the pacing effect. The anode-directed electron velocity is zero at some location downstream of the ionization layer, becomes comparable to the ion Bohm velocity in the middle of this layer, and exceeds the ion velocity near the anode. Thus, capturing the electrons that are initially near the anode must be paced by the ion emission rate, i.e., the Bohm velocity times the instantaneous density in the separatrix area; on the other hand, capturing the electrons that start out near the separatrix may actually be slow enough to pace the latter portion of the current pulse. If the ion Bohm velocity (of the order of 4,000 m/s) were the single pacing item, we would expect a pulse width of only 0.013 ms., which is shorter than observed (closer to 0.1 ms); electron capture delay may supply the difference, or perhaps the ionization of left-behind neutrals may have the effect of stretching the pulse time.

Finally, the question arises whether the erosion rate and pattern is influenced by the operating mode (LC or HC). Unfortunately, our erosion data are currently confined the HC mode only. The surprising result that the second cusp is eroded faster than the third cusp and the region beyond it would seem to imply that there is indeed an influence. If operation had been in the steady LC mode, where the plasma is densest near C3, it would be difficult to envision this concentration near C2. In the HC mode, according to our discussion above, dense plasma must be filling the central region of the thruster for the duration of the high current pulse, and so, even if the temperature were the same as in LC mode, and the same net amount of plasma were processed in each case, one would expect a relative intensification of the ion bombardment at C2, a region with lower plasma density in LC mode. In addition, the ionization pulse must imply an actually higher electron temperature than in the LC mode, and hence sheath strength, during the pulses, although we have no direct evidence for this effect. Thus, a reasonable expectation is that a lower erosion rate, at least in the vicinity of C2 will be measured when data can be obtained in LC mode. This remains therefore a strong priority for further research, both experimental and theoretical.

14. Preliminary PIC results in oscillatory mode

The work reported here is unpublished at this time. Modeling DCFT operation in the HC mode presents even greater computational challenges than modeling the steady LC mode. Using the MIT PIC plasma model described in Section 8 of this report, the greatest difficulties have come from working through the start-up transient in the code. This is likely due to initial conditions that do not resemble the actual state of the thruster. However, recent simulation results have been able to continue past the start-up transients, and were run for over 2 million iterations with an average time step of about 18 ps. The total wall time for these simulations was about 10 days, and were completed in intervals of 500 or 750 thousand iterations to avoid excessively large file sizes.

Figure shows the simulated anode current. The apparent discontinuity in the data is artificial, and has to do with an error writing and reading certain data points from data files - not with the dynamics of the simulation. The period between the start-up transient and the current peak is approximately 32 μs , while the period of the current burst is approximately 0.5 μs . To bring the dynamics of heavy particles on to a timescale more similar to electrons, their mass is reduced by a factor of 1000 in these simulations, meaning that time periods based on ion and neutral speeds should be scaled up by a factor of $1000 \approx 31.6$. As such, the simulated time periods should be interpreted as predicting a delay between current spikes of 1 ms, while the predicted pulse duration is 16 μs . The period between current spikes is almost certainly still affected by the initialization of the simulation, but the observed oscillation period is of the same order, about 0.3 ms. Measured pulse durations are longer than predicted here, typically by a factor of 2-4. Nonetheless, these results are a preliminary sign that modeling the HC mode will be feasible, contrary to our initial assessment.

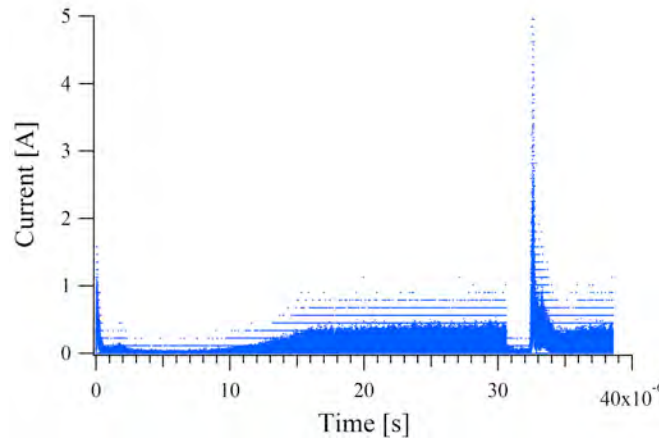
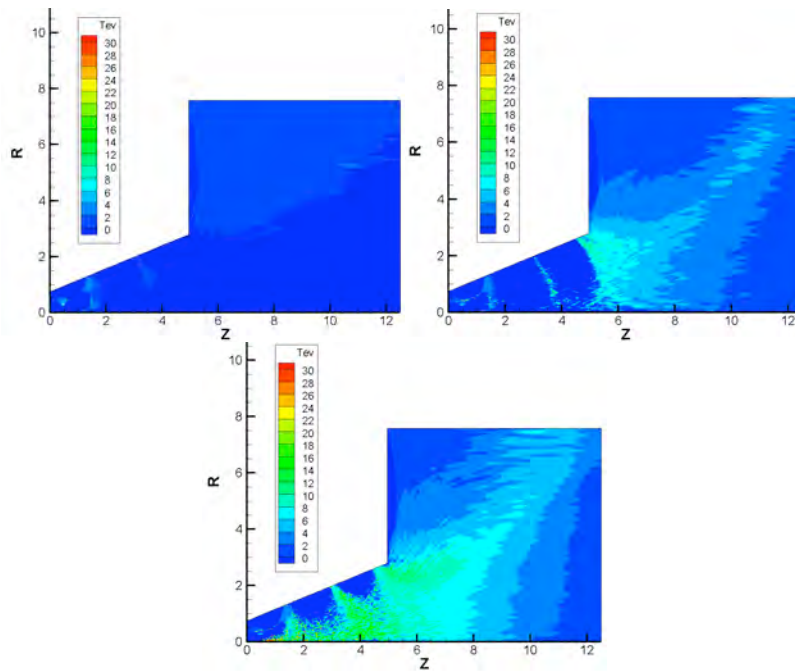


Figure 60: Simulated anode current as a function of simulated time. The anode current at the start of the simulation is due to the initialization transient, while the second peak in current may represent the successful recreation of the spikes in anode current observed to accompany HC mode operation. The transient characteristics of the anode current are described more thoroughly in other sections of this report.

Predicted distributions of electron temperature in the chamber and near plume are shown in Figure . Again, these results are preliminary, though they show the electron temperature increasing first at the third cusp, near the exit. Then, at a time scale faster than the sampling rate for these figures, the high-temperature region penetrates the last separatrix and fills each upstream cusp. As the intensity of the current pulse wanes, the regions of high electron temperature move in different directions. Upstream of C3, the high temperature region moves toward the anode as electrons are absorbed there. Past the last cusp, the high temperature region disperses out into the plume. Presumably, the highest temperature regions coincide with ionization regions, since electron density is also peaked in the cusps.

These simulation results will be expanded upon by recording the spatial variations in plasma density and temperature at a greater frequency during the spikes in anode current. This should allow us to observe the dynamics of the HC mode. Also, these fully developed simulations will be used to start simulations at different operating conditions, bypassing the start-up transient in most cases. Simulation of the LC mode will enable predicted erosion rates, allowing us to assess any lifetimes benefits associated with either operational mode.



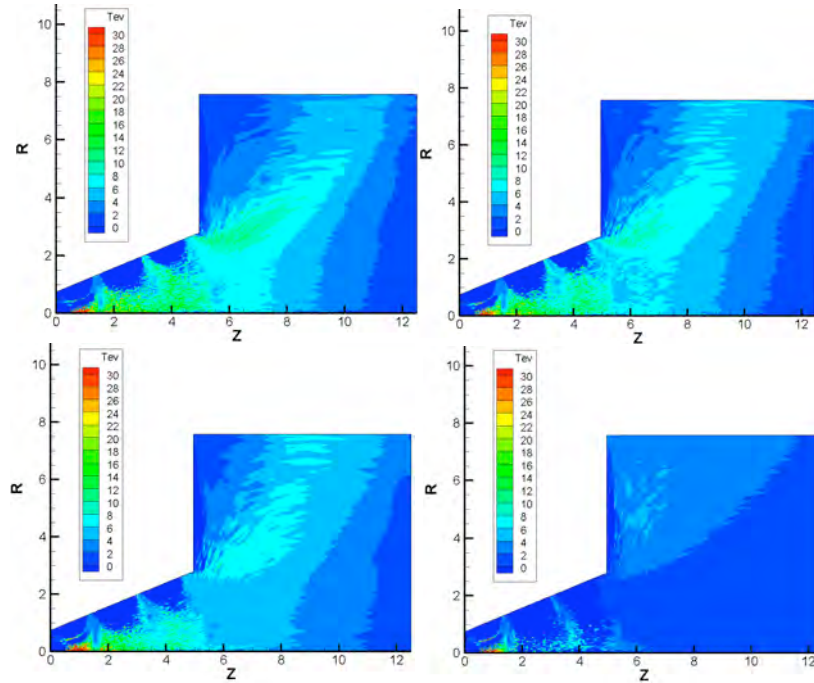


Figure 61: Electron temperature is plotted every 10,000 iterations for the first six pictures, which are in sequential order from left to right, top to bottom. The last figure shows the distribution of electron temperature several tens of thousands of iterations later, to demonstrate that the plasma temperature decreases as the current pulse passes.

15. Conclusions and recommendations

Through the work reported here, with the close cooperation of the teams at Stanford and at the AFRL (Edwards), significant progress has been made in the understanding of the plasma physics involved in the operation of a thruster with strong magnetic cusps used for wall protection and electron throttling. Some of the most important conclusions that have been reached are:

- Unlike the cylindrical cusped thruster tested at Stanford, the MIT divergent model operates in one of two modes, of which one is steady, with relatively low current (LC mode) and the other shows strong periodic current pulses, and has higher current (HC mode).
- Experiments and simulation indicate that the LC mode is characterized by an ionization layer that occupies the outer portion of the last magnetic separatrix surface.
- The hollow nature of the plume and its divergence angle are well explained by this localization of the ionization layer. This is confirmed by tests in which the plume angle

did respond as expected to modifications of the last separatrix (induced by an auxiliary coil).

- Kinetic theory and surface probing show that ions can only reach the wall over a narrow ring at each of the three cusps. This ion confinement is electrostatic, although it is mediated by the strong magnetization of the electrons. The ion flux over the accessible areas is similar to that through non-magnetized pre-sheaths.

- Consistent with the above, insulator erosion is limited to narrow bands around the cusps, and the erosion rate is of the same order, but smaller than that in Hall thrusters of similar power.

- Erosion data, taken in HC mode only, show highest rate at the intermediate C2 cusp, rather than at the expected C3 cusp. This has been tentatively associated with the strong oscillations occurring in HC mode.

- Detailed experimental characterization of the oscillations in HC mode has shown that the current pulsing frequency is determined by the neutral re-filling time after near depletion by the previous pulse. As flow rate is reduced, the thruster becomes able to operate in LC mode for one or more re-fill times before the next pulse is triggered, and at low enough flow, the pulses are not triggered any more.

- Although relatively small emphasis was put on thruster performance, it was observed that metallic deposits on the insulating shell were reducing efficiency and generating unpredictable mode changes and surface probe difficulties. The sources of the metal appear to be the cathode and especially the stainless steel injector frit.

Based on the above, we can make a few recommendations for future research on these thrusters:

- All the knowledge accumulated through this program should be put to use in the design of a second generation thruster with superior erosion and performance characteristics.

- Erosion data should be taken on a thruster that operates in the LC mode. This could be the current Stanford model, or perhaps a new-design model that can be reliably kept in LC mode.

- Even though the HC mode is unlikely to be the preferred one, its study should continue intensively, using both simulation and experiments, so as to clarify the transient physics and lay the basis for future design targeting the best operating mode.

- The role of surface materials and surface condition should be investigated more thoroughly. This should include ceramic type, with various metal film deposits, and with varying properties, particularly secondary electron emission.

16. References

1. D. G. Courtney and Manuel Martinez-Sanchez, "Diverging Cusped Field (DCF) Hall Thruster", IEPC-2007-39, 31st. International Electric Propulsion Conference, Florence, Italy, Sep. 2007.
2. D. G. Courtney, P. Lozano and Manuel Martinez-Sanchez, "Continued investigation of Diverging Cusped Field thruster". AIAA Paper 2008-4631, 44th Joint Propulsion Conference, Hartford, CT, 2008.
3. E. Ahedo and M. Merino, Two-dimensional supersonic plasma acceleration in a magnetic nozzle". *Phys. Plasmas* **17**, 073501 (2010).
4. E. Ahedo and M. Merino, "On plasma detachment in propulsive magnetic nozzles", *Phys. Plasmas* **18**, 000000 (2011).
5. Courtney, D. G., "Development and Characterization of a Diverging Cusped Field Thruster and a Lanthanum Hexaboride Hollow Cathode," S.M. Thesis, Massachusetts Institute of Technology, Cambridge, MA, June 2008.
6. T. Matlock, R. Daspit, O. Batishchev, P. Lozano and M. Martinez-Sanchez, "Spectroscopic and electrostatic investigation of the DCF thruster". Paper AIAA-2009-4813, 45th Joint Propulsion Conference, Denver, CO, 2009.
7. T. Matlock, P. Lozano and M. Martinez-Sanchez, "Discharge chamber wall flux measurements in a DCF thruster", presented at the ESA 2010 Space Propulsion Conference, S. Sebastian, Spain, May 2010.
8. P.C. Stangeby, *J. Appl. Phys.* **15**, 1007-1029 (1982)
- 9 J.A. Tagle, P.C. Stangeby, S.K. Erents, *Plasma Phys. and Controlled Fusion* **29**, 297-301 (1987)
10. V.I. Demidov, S.V. Ratynskaia, R.J. Armstrong, K. Rypdal, *Phys. of Plasmas* **6**, 350-358 (1999)
11. M. Stanojević, M. Čerček, T. Gyergyek, N. Jelić, *Contrib. Plasma Phys.* **34**, 607-644 (1994)
12. . K. N. Leung, N. Heshkowitz and K.R., McKenzie, *Phys. Fl.* **19**, 1045 (1976).
13. A.A Hubble, J.E. Foster. 44th AIAA/ASME/SAE/ASEE JPC (2008).
14. M. Martinez-Sanchez and E. Ahedo, "Magnetic mirror effects on a collision-less plasma in a convergent geometry", *Phys. Plasmas* **18**, 1 (2011). Also presented at the ESA 2010 Space Propulsion Conference, S. Sebastian, Spain, May 2010.
15. G. F. Chew, M.L. Goldberger and F.E. Low, *Proc. R. Soc. London*, **74**, 145 (1959).
16. Miller, J.S., Pullins, S.H., Levandier, D.J., Chiu, Y., Dressler, R.A. , *J. Appl. Phys.* **91**, 984 (2002)
17. J.E. Ekholm, W.A. Hargus Jr., AIAA-2005-4405
18. Karabadzhak, G.F., Chiu, Y., Dressler, R.A., *J. Appl. Phys.* **99**, 113305 (2006)
19. Gildea, S.R., Martinez-Sanchez, M., Nakles, M.R., and Hargus Jr., W. A. "Experimentally Characterizing the Plume of a Divergent Cusped-Field Thruster". 31st International Electric Propulsion Conference, Ann Arbor, MI. September 2009. IEPC-2009-259.
20. Y. Azziz, Experimental and Theoretical Characterization of a Hall Thruster Plume, Ph. D. Thesis, MIT, May 2007.
21. J. J. Szabo, Fully kinetic numerical modeling of a plasma thruster, PhD Thesis, MIT, Jan.

2000.

22. V. Blateau, "PIC simulation of a ceramic-lined Hall effect thruster". MS Thesis, MIT, Aero/Astro, May 2002.
23. J. Fox, Advances in Fully-Kinetic PIC Simulations of a Near-Vacuum Hall Thruster and Other Plasma Systems, PhD thesis, MIT, June 2007.
24. S. R. Gildea, "Fully Kinetic Modeling of a Divergent Cusped-Field Thruster", MS Thesis, Sep. 2009.
25. Gildea, S.R., Martinez-Sanchez, M. "Improvements in Divergent Cusped-Field Thruster Modeling". ESA/A3F Space Propulsion Conference, San Sebastian, ES, May 2010.
26. Young, C.V., Smith, A.W., Cappelli, M.A., "Preliminary Characterization of a Diverging Cusped Field (DCF) Thruster," 31st International Electric Propulsion Conference, Ann Arbor, MI, September 2009. IEPC-2009-166.
27. N. A. McDonald, M. A. Cappelli, E. R. Gildea, M. Martinez-Sanchez and W. A. Hargus, "Laser-Induced Fluorescence velocity measurements of Divergent Cusped Field Thruster", to appear in the J. Phys. D, 2011.
28. Schneider, R., Matyash, K., Kalentev, O., Taccogna, F., Koch, N., and Schirra, M. "Particle-in-Cell Simulations for Ion Thrusters" Contrib. Plasma Phys. 49, No. 9, 655-661 (2009)
29. Raitses, Y., Merino, E., Fisch, N.J., Journ Appl Phys 108(093307), 2010.
30. Young, C., Smith, A., Cappelli, M., 31st IEPC, 2009.
31. Gildea, S.R., Matlock, T.S., Martinez-Sanchez, M., and Hargus Jr., W.A. "Erosion Measurements in a Low-Power Cusped-Field Plasma Thruster". In preparation.
32. Hofer, R.R., Mikellides, I.G., Katz, I., and Goebel, D.M. "BPT-4000 Hall Thruster Discharge Chamber Erosion Model Comparison with Qualification Life Test Data," 30th International Electric Propulsion Conference, Florence, IT, September 2007, IEPC-2007-267.
33. Christensen et al. IEEE Trans. Plasma Sc., Vol. PS-5, No. 1, 1977.
34. Knorr and Willis, Zeitschrift Naturforschung Teil A, Vol. 37, 1982.
35. Yim, J.T. "Computational Modeling of Hall Thruster Channel Wall Erosion," Ph.D. Thesis, The University of Michigan, Ann Arbor, MI, 2008.
36. Gildea, S.R., Matlock, T.S., Lozano, P., and Martinez-Sanchez, M., "Low Frequency Oscillations in the Diverging Cusped-Field Thruster". 46th Joint Propulsion Conference & Exhibit, Nashville, TN. July 2010. AIAA-2010-7014.
37. Barral, S. and Ahedo, E. "Low-frequency model of breathing oscillations in Hall discharges," Physical Review E, Vol. 79, 046401 (2009)

Detailed Report on Tasks PT1 to PT4

1 PT1: Current Sheet Formation in a Conical Theta Pinch FARAD (COP-FARAD)

1.1 Introduction

Pulsed inductive thrusters [6] are a specific class of electrodeless thrusters under development for use in space propulsion applications. Electrodeless thrusters are attractive because of their avoidance of the lifetime-limiting issues associated with electrode erosion. In addition, they can process propellants such as CO_2 and H_2O that are incompatible with metallic electrodes.

These thrusters operate by discharging a short, high-current pulse through an inductive coil, producing a time-changing magnetic field that induces an electric field in accordance with Faraday's law. The propellant breaks down (ionizes) near the inductive coil, where the induced fields are sufficiently strong, and a current sheet forms with current flowing in the opposite direction to that of the current in the inductive coil. When the opposing current loops are close to each other they can be seen as a transformer, coupling the plasma to the driving circuit. The high magnetic pressure that exists between the plasma current sheet and the inductive coil can potentially accelerate the current sheet and any entrained propellant away from the coil to produce thrust, as long as the relevant scaling parameters are kept within the optimum range of values [7]. If the thruster design does not ensure the proper values for these parameters, the current sheet may remain coupled to the driving circuit, or never form at all. Optimizing current sheet formation can therefore greatly improve the performance of this type of thruster.

The Conical Theta Pinch FARAD (COP-FARAD) is a permutation of the original FARAD concept we introduced in Ref.[2] with the single difference that a conical inductive coil is used instead of a flat coil. Figure 1 shows,

in the left panel, a schematic of the original FARAD design with the flat acceleration inductive coil.

In the present work, the flat coil is replaced by the conical coil shown in the right panel of the same figure. This geometry allows for a non-cusp applied magnetic field that more closely follows the coil's face and that should be more effective at guiding the pre-ionized propellant to the coil. Because of this conformity to the natural path of plasma diffusion, current sheets are possible in CØP-FARAD even with no applied magnetic field. Moreover, the CØP-FARAD cone is expected to produce an additional thrust component derived from electromagnetic pinching of the plasma.

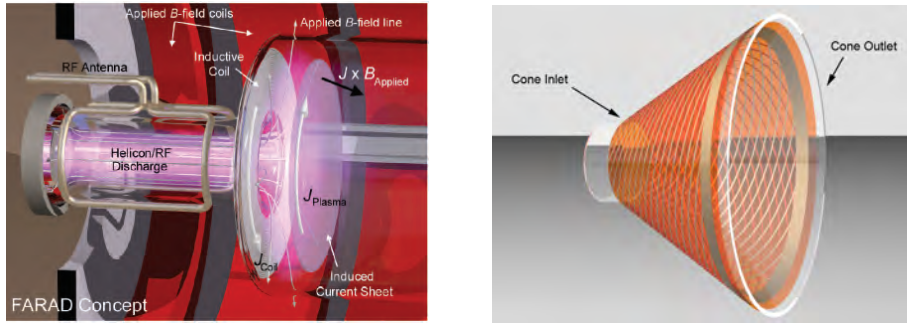


Figure 1: Left: Schematic of original FARAD set-up with flat Inductive coil. Right: Schematic of replacement conical coil.

The propulsive efficacy of the current sheet depends on a number of factors (e.g., sheet strength, extent, decoupling distance from the coil, propellant leakage, pinching, stability, etc.). Only two of these, namely strength and extent, are the focus of the present study. Specifically, the thruster should ideally induce a strong (high current-density) current sheet that uniformly extends over the entire coil surface in order to maximize the amount of work done on the plasma. An understanding of the mechanisms and conditions controlling the intensity and extent of the current sheet would be useful in providing guidance for future designs and in choosing operating conditions that most enhance these two sheet performance indices with respect to propulsive efficiency.

The goal of the study reported here is to provide the first clues on the underlying mechanisms and conditions behind the formation, intensity and extent of current sheets in CØP-FARAD. Ultimately, for a given physical configuration, we need to know how to maximize the thruster's performance

as a function of the controllable operating parameters (mass flow rate, propellant type, RF power, and applied magnetic field topology and strength). In the present study we start with our attempts at elucidating the underlying physical mechanisms by focusing on the most basic dependencies of sheet formation, namely the role of background density. While in a real thruster the background density, for a given configuration and RF power, is controlled by the mass flow rate through the thruster, in this basic study we chose to control the background density by varying the uniform back-fill gas pressure, while holding all controllable parameters fixed and applying no magnetic field. This removes the complications of the flow and expansion of the pre-ionized gas from the picture and allows for a clearer isolation of the basic mechanisms controlling current sheet formation, strength and extent.

Furthermore, before carrying out detailed studies using Langmuir probes, B-dot probes, and more analytical optical diagnostics, we limited our initial investigation to a single diagnostic: time-integrated photography. This was motivated by the visually rich character of the distinguishable visible-light emission associated with the sheet.

The rest of the paper is organized into successive sections in which we describe the experiment, document the new conical coil design, describe the photographic data collection, report the observed trends and attempt to extract physical insight into some of the basic mechanisms underlying sheet formation, strength and extent.

1.2 Experimental Setup

1.2.1 Vacuum Chamber

All experiments were performed in a vacuum chamber consisting of two pyrex cylinders joined together by a fiberglass plate on which the CTP is mounted, extending 12 cm into the larger cylinder. The smaller cylinder has an inner diameter of 6 cm and is 37 cm long and the larger cylinder has an inner diameter of 20 cm and is 46 cm long. While the experiment can be operated with mass injection through the endplate of the smaller cylinder, for the present study the chamber is back-filled to various pressures from a port on the opposite end of the experiment. The pressure is monitored using a Granville Phillips 275 mini-convectron pressure gauge. Plasma is created in the smaller, pre-ionization chamber and diffuses through a 6 cm inner diameter concentric hole in the fiberglass plate into the region bounded by

the CTP before eventually migrating into the remaining volume of the larger cylinder. A 150 l/s turbomolecular pump backed by a roughing pump is attached to the larger cylinder at the endplate opposite the CTP inductive coil; the same endplate where gas is fed into the vacuum vessel.

1.2.2 Plasma Source

A Boswell-type saddle antenna is wrapped around the smaller cylinder, creating the pre-ionization chamber. The saddle is composed of quarter-inch copper tubing attached to a water cooling line. An ENI 13.56 MHz 1.2 kW power supply is coupled to the antenna through a tuner consisting of two Jennings 1000 pF 3kV variable vacuum capacitors located immediately next to the antenna and used to minimize reflected power. A Faraday cage surrounds the entire experiment to shield from radiated RF fields.

1.2.3 Conical Theta Pinch

The conical theta pinch is composed of a flexible circuit board wrapped around a pyrex funnel with a wall thickness of 4 mm and providing structural support to the circuit board. The neck of the funnel, with a 6 cm inner diameter and 2 cm length, fits into the concentric hole in the fiberglass plate holding the funnel's axis parallel to the horizontal plane. The conical coil used for the present study has a half-angle of 30 degrees. The design of the circuit board, shown in Fig. 2, is based on the design of the flat inductive coil found in the current PIT[1] and the original FARAD experiment. The circuit traces follow an Archimedes spiral with current flowing down one surface from the bus at the major radius to plated through holes at the minor radius. This current then proceeds up the back side of the circuit board (shown as lighter-colored traces in Fig. 2), providing cancellation of the radial component of current with the traces from the front side. In this way, the circuit produces a purely azimuthal current that is uniform across the coil face. The traces that form this azimuthal current end 4 cm before the downstream end of the cone, and all normalization made with respect to a particular distance from the cone inlet is made with respect to the downstream end of the cone (not the edge of the inductive coil).

Current is fed to the coil through strip-lines, one between a 39.2 μ F capacitor and the vacuum vessel and another from the interior wall of the vacuum vessel fiberglass plate to the circuit-board bus (shown in Fig. 2). The circuit

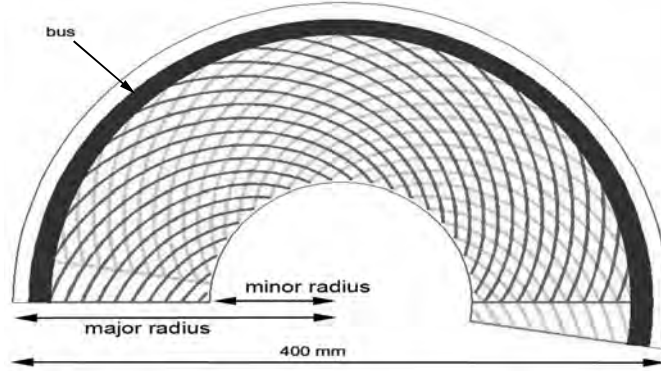


Figure 2: The CTP inductive coil shown as it is a print on a circuit board, with twenty spirals per side printed onto a .002 inch-thick Kapton substrate to maintain flexibility. Current is fed to the circuit through the bus, flows down the darker-colored traces on the front side of the circuit board, through plated through holes at the minor radius, and then up the lighter-colored traces on the back side. The ends of the board are brought together to form the conical theta pinch.

penetrates the vacuum vessel through metal standoffs, which connect the two striplines. The current pulse is initiated (as in the FARAD) using a “hammer” switch. When a current pulse is thus fed into the coil, a time changing radial and axial magnetic field and an azimuthal electric field are induced in the volume contained by the coil. If pre-ionized propellant is present within the decoupling distance of the coil, a current sheet will be induced in this propellant during the first half-cycle of the pulse at voltages an order of magnitude lower than those required for operation of the PIT [2]. This current sheet will form such that, inside of the sheet, its own induced field cancels out the magnetic field from the coil and, between the current sheet and coil, the two induced fields add. This build-up of magnetic pressure acts to accelerate the current sheet away from the coil normal to the coil surface for a uniform induced magnetic field profile.

Since the force is normal to the coil surface, the CTP inductive coil provides a radial force density on the plasma current sheet as well as an axial one. The axial component of the force density contributes to the total thrust by imparting axial directed kinetic energy to the current sheet and any entrained propellant. The radial force density component takes advantage of a portion of the pre-ionized propellant that is not involved in current sheet formation

by pinching the current sheet, and can provide an additional contribution to thrust as well as reduction in the divergence of the exiting plasma. Schematics showing the idealized stages of sheet formation and pinching are shown in Fig. 3.

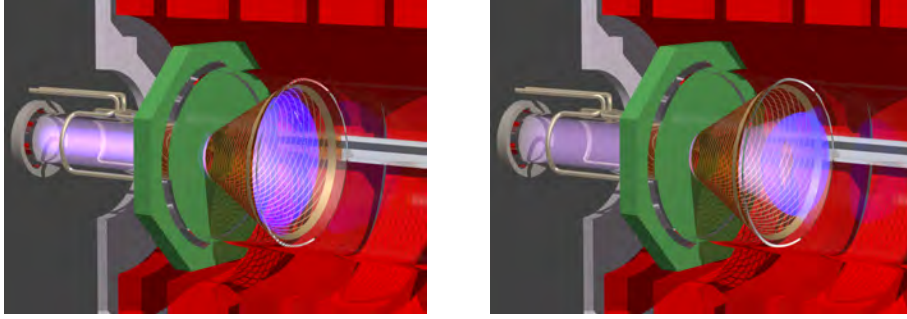


Figure 3: Idealized schematics showing current sheet formation (left panel) and pinching (right panel) in the C \ddot{O} P-FARAD.

1.2.4 Time-integrated Photography

A Nikon D50 digital SLR camera with a 50 mm focal length lens was used to capture time-integrated images of the luminous pattern associated with the current sheet. All automatic compensation for light intensity, gamma, and color balance were defeated in the acquisition of these data. Each picture was taken with a half second exposure time, an ISO of 400, and a preset whitebalance of uniform gray. The camera was mounted for a top view of the cone at a distance of roughly 60 cm from the cone exit. Due to physical constraints of the experimental setup, the camera is unable to view the cone surface at an angle where the “film plane” of the camera is parallel to the plane subtending the bottom edge of the cone. All photographs were obtained with an angle of 30 degrees between these two planes.

The picture frame includes the lower half of the inside cone surface, allowing determination of the intensity and extent of the luminous structure from the cone’s inlet to its outlet. The aperture is remotely opened, the switch is then activated sending the current pulse through the coil, and the aperture closes automatically after one half second.

1.3 Experimental Results

1.3.1 Interpretation of the Images

While the steady-state argon discharge from the RF source fills the cone with a gas radiating pink light, this distinct luminosity is greatly overpowered by an azimuthally-symmetric bright blue discharge that emanates from inside of the cone when the switch is closed. We make the assumption that the intensity, location and extent of this latter luminous structure along the wall of the cone are highly related to those of the current sheet. However, previous study of current sheets between plane electrodes[3] using high-speed imaging and B-dot probes showed high correlation between the current carrying structures and their luminous signatures. In our study, the use of time-integrated photography implies a loss of some of this correlation since the luminous structure is more a representation of both the regions where the current has passed at some time during the pulse and those containing radiating gas that does not carry current. Moreover, since the current sheet presumably moves away from the cone's inner surface during the pulse, there is a parallax error associated with determining its location along the cone's surface from time-integrated photographs obtained with a camera whose film plane is not parallel to the cone's axis of symmetry.

Due to these limitations we take the measured intensity, location and extent of the luminous structure that appears during the pulse as rough representations of the corresponding features of the current sheet and limit our conclusions to only relative changes in these measured quantities.

1.3.2 Image Processing

All image processing is performed in MatLab. The images are filtered for blue light to increase the signal to noise ratio. To further increase the signal to noise ratio, a first photo that includes a current sheet is taken directly before a second photo with no current pulse (but with the background RF plasma on), and this second image is subtracted from the first to eliminate a large fraction of the background light associated with the steady-state RF discharge. This procedure is repeated five times for a given condition and the intensity values are averaged. Intensity values on a line along the cone surface are plotted with respect to distance from the cone inlet. When distance from the cone inlet is normalized, it is normalized to the cone outlet, which occurs at 13.5 cm from the cone inlet. The edge of the inductive coil occurs at 9.5

cm from the cone inlet, and corresponds to a normalized distance of .7. The resulting axial profiles are also integrated and normalized to their peak values to provide a measure of the intensity and extent of the luminous structure.

1.3.3 Measured Profiles and Pressure Dependencies

The RF power source was held constant at 200W forward power and 1% reflected power. No applied magnetic field was employed and the voltage on the capacitor was maintained at 1.25 kV for each pulse. The argon back-fill pressure in the CTP vacuum vessel was varied from 4 mT up to 48 mT.

Figure 4 shows intensity profiles along the cone's wall with the inlet located at 0 cm and the exit at 13.5 cm. Representative profiles from eight back-fill pressure levels spanning the range of varied pressure are shown. The small peak at the latter location is due to light reflection from the downstream edge of the cone.

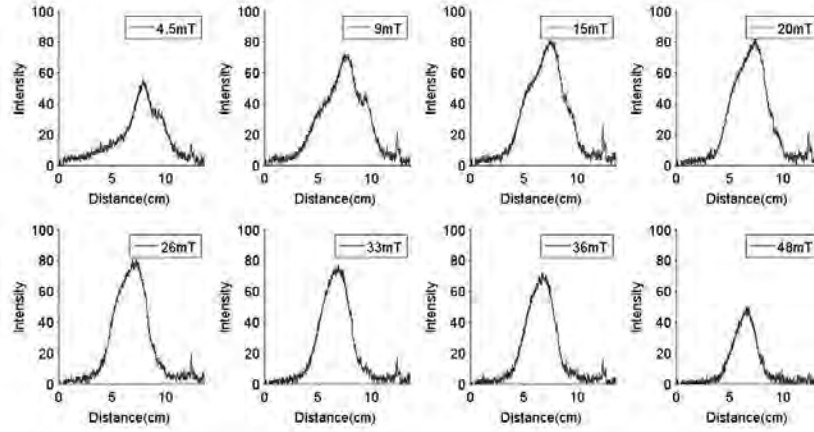


Figure 4: Profiles of intensity (in arbitrary units) versus distance from inlet along the cone's wall for eight back-fill pressure levels spanning the back-fill pressure range

Figure 5 shows the effective intensity of the current sheet plotted as a function of pressure. Effective intensity for a given pressure is calculated by integrating the curve of intensity versus position and normalizing it with respect to the maximum value for that integral attained over the pressure range.

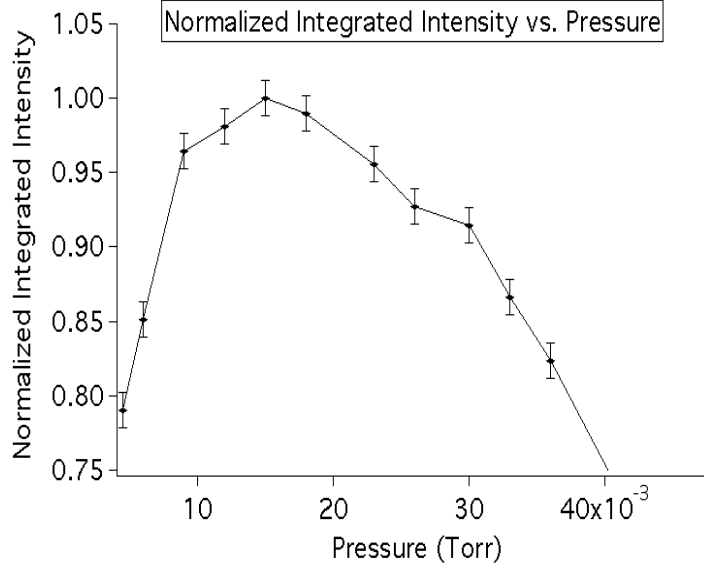


Figure 5: Effective intensity of the current sheet as a function of back-fill pressure

Figure 6 shows a plot of effective current sheet extent versus pressure. Effective current sheet extent along the wall (in the axial direction) for a given pressure is calculated as the integral of the curve of intensity versus position divided by the peak intensity for that pressure and normalized to the maximum current sheet extent attained over the pressure range.

The effective location is determined by calculating the centroid for each curve of intensity versus distance from the cone inlet. The centroid locations are normalized by the distance between the cone inlet and exit (13.5 cm), with the cone inlet and beginning of the inductive coil at 0, the inductive coil ending at .7, and the exit at 1, and plotted versus back-fill pressure in Fig. 7.

1.3.4 Observations

From the experiments and the plots of Figs. 4-7, we make the following observations:

1. Current sheets of varying intensity, extent and location were observed to form at each of the back-fill pressure levels in the investigated range

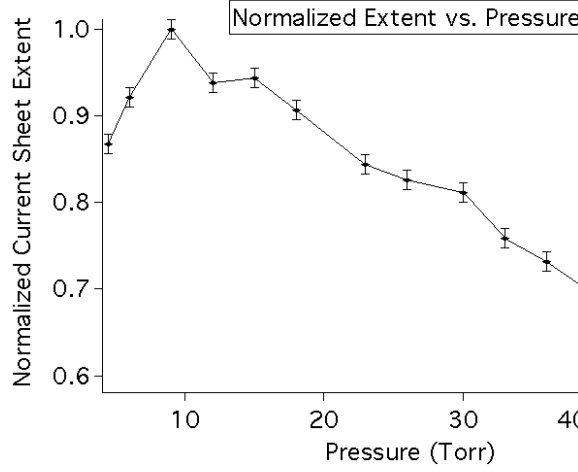


Figure 6: Effective axial extent (along the wall) of the current sheet as a function of back-fill pressure. The values of the extent are normalized by the largest value.

(4 to 48 mTorr).

2. There is an optimal back-fill pressure, P^* (between 10 and 15 mTorr for the particular conditions of this experiment), for which both the effective intensity and extent of the current sheet are largest (Figs. 5 and 6).
3. The rate of change in effective intensity (and extent) with pressure differs on either side of this optimal pressure. Specifically, the growth rate of intensity (and extent) with increasing pressure below P^* is significantly higher than its decay rate with increasing pressure above P^* .
4. For pressure levels below P^* , the current sheet intensity profiles are not symmetric and are relatively more extended towards the cone exit. Above P^* they become more symmetric with respect to cone inlet and cone outlet (Fig. 4), but at all pressures the current sheet favors the downstream end of the inductive coil.
5. For all pressure levels in the investigate range, current sheet formation occurs around the middle section of the cone but strongly favors the downstream half of the inductive coil. As can be seen in Fig 7, current

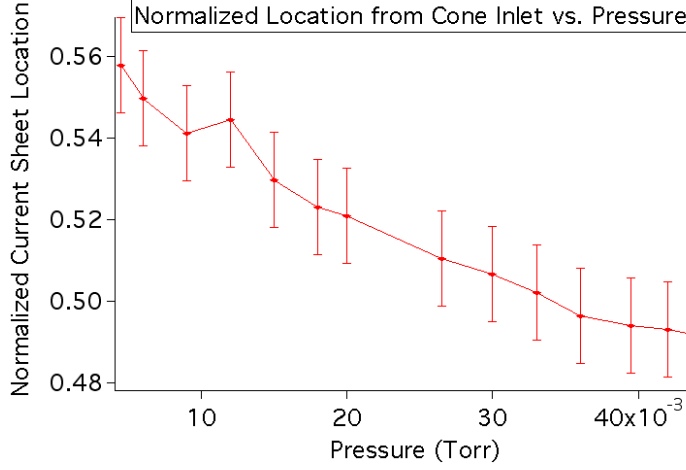


Figure 7: Effective location (along the wall) of the current sheet as a function of back-fill pressure. The locations are normalized so that the cone inlet and beginning of the inductive coil are at 0, the end of the inductive coil is at .7, and the cone exit is at 1.

sheet formation occurs at normalized distances of 0.5 to 0.56 from the inlet, while the end of the coil occurs at .7.

6. As the pressure rises the effective location of current sheet formation moves slightly, but definitely and monotonically, towards the inlet (Fig. 7).

We proceed by using these qualitative observations to glean some basic aspects of the mechanisms underlying current sheet formation in such a device.

2 Discussion and Interpretation of the Observations

The existence of an optimal pressure (Observation 2) is indicative of a Townsend-like breakdown. On the lower-pressure side of P^* , due to the relatively lower neutral density, the electrons involved in current sheet breakdown undergo fewer ionizing collisions with the background neutrals, while on the higher pressure side of that optimum they gain less energy from the electric field between collisions because their mean free path between collisions with neutrals is smaller.

Unlike in the classic Townsend breakdown, however, there is a finite steady-state background electron density from the steady-state RF discharge in FARAD without which breakdown would require far larger pulse energies. Measurements of a similar RF argon discharge at fixed RF input power of 200 W were reported by Chang et al.[4] and are reproduced in Fig. 8. These data show that the electron density increases with pressure over the pressure range of our experiment. (Of course this increase cannot go indefinitely at constant power as the energy input per unit mass decreases with increasing pressure.)

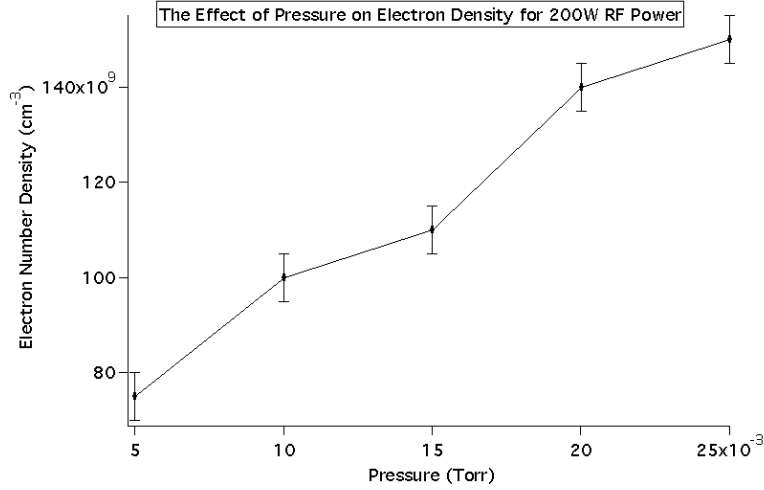


Figure 8: The effect of pressure on electron number density in a 13.56 MHz RF inductive discharge.[4]

The reported increase of electron density with back-fill pressure implies that the decrease in ion production rate due the lower average electron energy on the high-pressure side of P^* is, to some extent, counterbalanced by the increase in the number of background electrons. This would explain the lower rate of decrease in the current sheet's intensity and extent vs pressure at that side of the optimum relative to their increase rate on the lower-pressure side (Observation 3).

It is well known in pulsed plasma thruster research that the current sheet tends to form in such a way that the inductance presented to the circuit is minimized[5]. For the conical theta pinch, this implies a current sheet forming at a location that serves to exclude as much coil-generated magnetic

flux from the interior volume of the coil. A current sheet forming at the downstream end of the coil circumscribes a larger area circle than a current sheet forming further upstream. This may explain why the current sheet favors the downstream location.

In addition, a current sheet forming at the downstream edge of the inductive coil will tend to affect magnetic flux lines further upstream, forcing them to stay close to the walls of the theta-pinch to maintain $\nabla \cdot \mathbf{B} = 0$. A current sheet forming near the upstream end, consisting of a smaller ring current, will not have nearly the same effect on the magnetic field lines in the rest of the theta pinch's interior. Consequently, the point of lowest inductance, and the point where the sheet is predisposed to form, is at or near the downstream end of the inductive coil. This may explain why the current sheet has an asymmetric extent favoring the exit end of the coil (Observation 4) and why current sheet formation (at all the investigated pressure levels) is biased (to a varying degree) towards the downstream end of the inductive coil (Observation 5). Because the circuit board traces end 4 cm before the cone outlet, current sheet formation is less dramatically biased toward the exit half of the cone as it is biased towards the downstream edge of the inductive coil.

The remaining observation (Observation 6) that current sheet formation has a tendency to move upstream with increasing pressure may be explained through a consideration of the inductive circuit shown in Fig. 9.

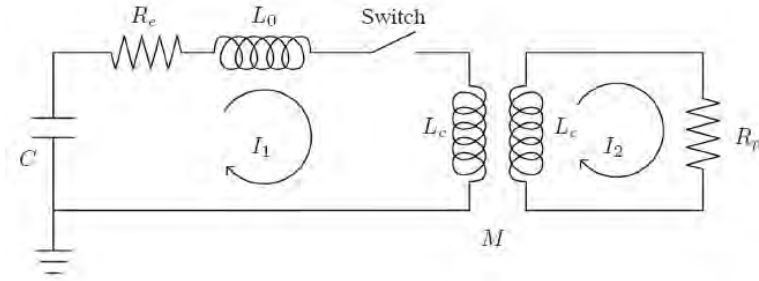


Figure 9: Schematic of the inductive circuit used to explain Observation 6

The resistivity of a weakly ionized plasma, such as the background RF-produced plasma in CØP-FARAD, is dominated by electron-neutral collisions. As the pressure increases, the frequency of these collisions increases, increasing the resistivity in the preionized plasma. During the inductive pulse, the plasma has a resistance R_p that is equal to the resistivity inte-

grated around the circumference of the coil. This value increases for a given axial location as a function of pressure and for a given pressure it decreases as we move axially towards the inlet. From a circuit point-of-view, we recognize that the voltage drop across the transformer must be equal to the voltage drop owing to the plasma resistance. This would require the current sheet to initially form further upstream in the theta-pinch coil as the pressure and R_p increase at a given axial location. Consequently, in a pulsed inductive discharge the sheet may be forced to form at a location other than the point of minimum overall circuit inductance.

2.1 Summary and Concluding Remarks

A photographic study of the effects of back-fill pressure on the intensity, extent and location of current sheets in a conical theta pinch FARAD thruster provide some basic insights into the mechanisms regulating current sheet formation. The existence of an optimal pressure for maximum sheet intensity and strength and the difference in the rates of change in these quantities with changing pressure on either side of this optimum were explained as the behavior of a Townsend-like breakdown modulated by a background electron density that increases with pressure. The effective axial location (along the wall) around which the sheet tends to form, and its dependence on pressure, are thought to be related to a dynamic balance between the resistive elements (depending on plasma resistivity and, thus, pressure) and inductive elements (depending on the axial location inside the conical coil) of an equivalent inductive circuit.

Future work will aim at verifying and consolidating these insights with more analytical diagnostics and models, with the ultimate goal of deriving prescriptions for optimizing current sheet formation and evolution as a function of controllable operating parameters, including the mass flow rate through the device, applied magnetic field and RF power.

3 PT2: Effects of Inductive Coil Geometry in C Θ P-FARAD

3.1 Introduction

The current rise rate in the plasma of the C Θ P-FARAD is a critical parameter because the faster the current rises in the current sheet, the smaller is the separation between driving coil and current sheet when the current sheet is fully-formed and the better is the inductive coupling between the two.

One way to hasten current sheet formation is through the use of a preionized propellant [8], which will also significantly reduce the required capacitor voltage and pulsed energy for forming and accelerating the sheet. Choueiri and Polzin [9] introduced the Faraday Accelerator with Radio-frequency Assisted Discharge (FARAD) to demonstrate the concept of preionization-assisted low discharge energy inductive current sheet formation. They have performed proof-of-concept experiments, developed design criteria [7], and identified potential advantages a FARAD thruster might enjoy over the current state-of-the-art Pulsed Inductive Thruster (PIT) [6, 10, 11], which relies on injecting a neutral gas onto the coil from a valve positioned downstream inside the plasma jet. Although the use of preionization adds complexity to the system, it can also help to eliminate complexity elsewhere, yielding a system that is, on balance, simpler and more compact. The proof-of-concept experiments were successful in demonstrating preionization-assisted current sheet formation at significantly lower capacitor voltages and pulse energies than those found in the PIT (1.5 kV and 44J versus 30kV and 4kJ).

In previous FARAD experiments, propellant reached the flat inductive coil surface from a preionization chamber located upstream of the coil. This required the use of a strongly cusped magnetic field to impose an almost ninety degree turn on the preionized propellant stream. Turning the propellant at such high angles was a difficult process, which motivated the design of an inductive coil that more naturally follows the diffusive path of the preionized gas, resulting in the Conical Theta Pinch FARAD (C Θ P-FARAD)[12], shown in Fig. 10. The C Θ P coil geometry is the sole difference between C Θ P-FARAD and the original FARAD used in previous proof-of-concept experiments.

Coil geometry affects current sheet formation through the mutual inductance (M) between the driving coil and the current sheet. Mutual inductance

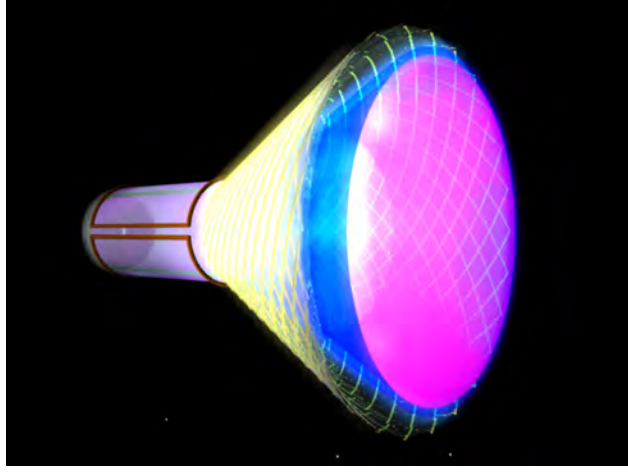


Figure 10: Conical Theta Pinch FARAD with preionization chamber to the left and current sheet shown in blue.

between two coils is defined as the amount of magnetic flux flowing through the second coil divided by the current flowing through the first, multiplied by the number of turns in the first:

$$M_{21} = \frac{n\phi_{21}}{I_1}, \quad (1)$$

and since ϕ_{21} scales linearly with I_1 , the mutual inductance is purely a function of the geometry and not the current.

The further the current sheet forms from the inductive coil, the lower the initial mutual inductance will be, causing a larger initial inductance to be presented to the driving circuit due to the current sheet's inability to shield out the field from the driving coil. The initial inductance presented to the circuit affects the efficiency of pulsed inductive-type thrusters according to the Lovberg criterion, which states that the efficiency is limited by the ratio of the total change in inductance to the initial inductance [13]:

$$\eta \leq \frac{\Delta L}{L_0} \quad (2)$$

Therefore, to achieve the most efficient operation, initial shielding of the inductive coil's magnetic field by the current sheet must be maximized in order to allow for the maximum possible change in inductance as the current

sheet moves away from the driving coil. This translates into an initially high mutual inductance between the driving coil and the plasma current sheet, however, if the mutual inductance remains high as the current sheet progresses away from the driving coil, the current sheet may remain coupled to the driving circuit at the time when the driving current reverses direction and begins removing energy from the current sheet. A balance must be reached with respect to the decrease in mutual inductance as a function of current sheet and driving coil separation such that the current sheet remains coupled until fully-formed, and then rapidly decouples before the driving current reverses direction.

In order to investigate this dependence, and more explicitly, the effects of coil geometry on mutual inductance, we constructed six inductive coils of differing half-cone angle and length and experimentally determined the mutual inductance between each coil and a current sheet replica as a function of the axial separation of the two. The “current sheets” were made of aluminum and with the same geometry as the driving coil.

We then obtained curve fits to the experimentally-determined mutual inductance versus position dependence, $M(z)$, for each of the six coil geometries, and used those fits as an input to the well-known model of the PIT[14, 13] in lieu of the previously used expression for $M(z)$ that was obtained empirically for the case of a 90 ° half-cone angle (i.e. the flat coil of the PIT). This allowed us to use calculations obtained from the model to draw conclusions about how the inductive coil geometry affects the performance, which in the context of this paper is defined as the final current sheet velocity.

The remainder of this paper is organized into successive sections in which we describe the experiment, report mutual inductance measurements, discuss the observed trends and, with the use of a model, extract physical insight into some of the basic influences of coil geometry on thruster performance.

3.2 Experimental Setup

3.2.1 Driving Circuit and Current Sheet Construction

We constructed models of the inductive coil with half-cone angles of 10°, 20° and 30°, and produced inductive coils of two different lengths for each angle (5 and 10 cm). All coils had a minor radius of 3 cm. A photograph of the coil of 10° half-cone angle and 5 cm length and its associated current sheet

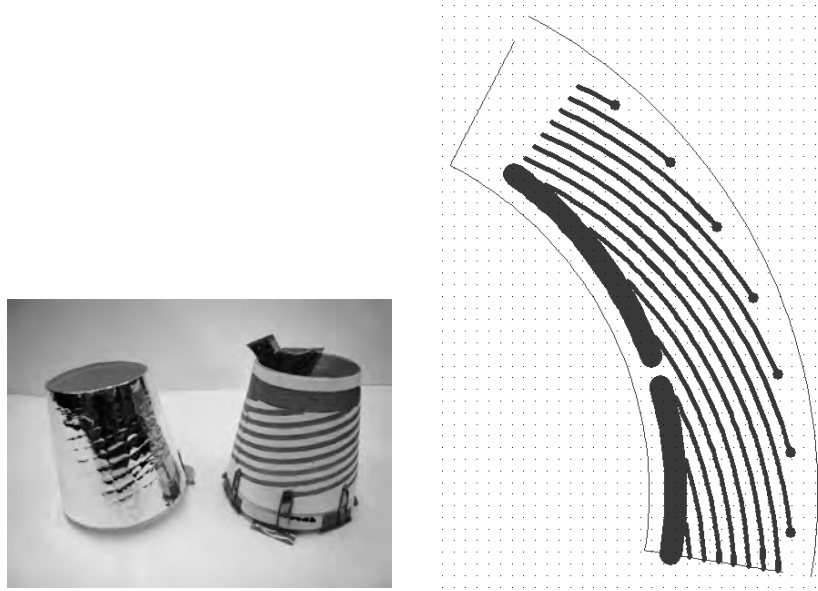


Figure 11: Left: Photograph showing a current sheet analog on the left and a driving coil with 10° half-cone angle, a length of 5 cm, and a minor radius of 3 cm to the right. and Right: An example of a computer-generated image from a gerber file.

analog (made out of aluminum foil as described in the next subsection) is shown in the left side of Fig. 11. Since mutual inductance is purely a function of geometry, and does not depend on the amount of current, the models were constructed at full-size but for low-energy operation only, allowing fast and inexpensive construction.

Gerber files, used for printing circuit boards, were written to produce the exact patterns that will be used in the full-scale construction of higher-energy driving coils. The right side of Fig. 11 shows an example of the image produced by a program that reads the Gerber files. These patterns, which are calculated to create a purely azimuthal current density along the surface of the inductive coil[13], are printed on two sides of printer paper and the traces filled in with conductive ink. The wide trace that extends nearly the entire length of the coil is where current is fed to the circuit, and the circles at the edge of the circuit are the locations where current transfers from one side of the circuit to the other.

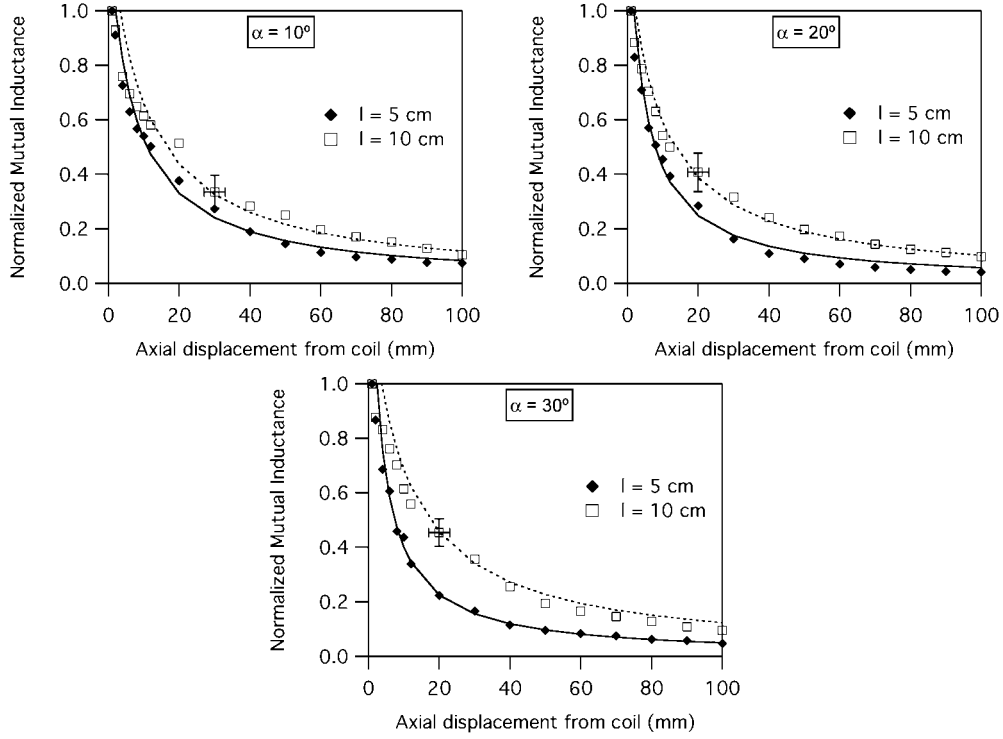


Figure 12: Mutual inductance between the inductive coils of 5 and 10 cm long and (from left to right, top to bottom) 10, 20 and 30 degree half-cone angle and their associated current sheets as a function of axial separation distance, normalized to the value at the smallest separation distance. Markers indicate experimental data, lines represent a fit to the data.

3.2.2 Position-dependent Mutual Inductance Measurements

A function generator provided current to the driving circuit in the form of a sine wave, whose frequency was set to the expected frequency of the full-scale circuit (50 kHz). The inductance shown to the driving circuit changes as a function of time due to the motion of the current sheet away from the driving coil. In order to simulate this effect, aluminum foil was wrapped around a supporting structure identical to that supporting the driving coil. The aluminum foil does not completely circumnavigate the supporting cone, leaving a space across which induced voltage may be measured. This induced voltage is a measure of the mutual inductance of the primary coil to the

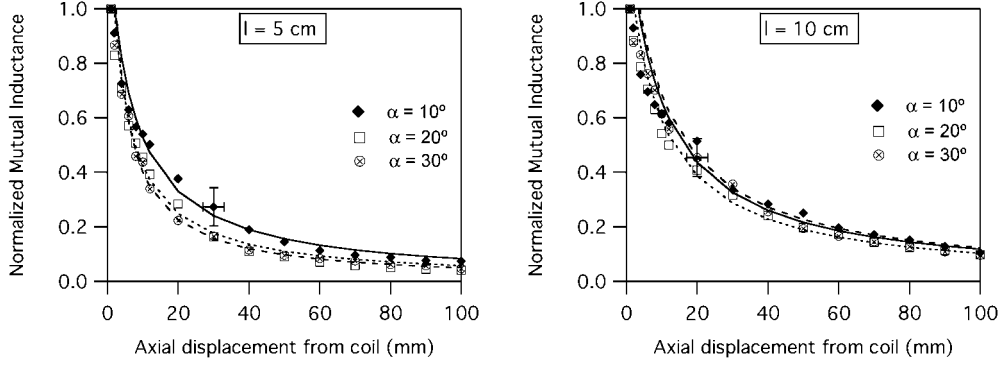


Figure 13: Mutual inductance between the inductive coils of 10, 20 and 30 degree half-cone angle and (left to right) 5 and 10 cm cone length and their associated current sheets as a function of axial separation distance, normalized to the value at the smallest separation distance. Markers indicate experimental data.

current sheet replica, and decreases as the current sheet replica moves further away from the driving coil. It is this decoupling that affects the inductance presented to the driving circuit. In the most efficient case, the current sheet will completely shield the field of the driving coil (a coupling coefficient of 1). When the current sheet moves away from the driving coil, the mutual inductance should reduce in such a way that the current sheet decouples from the driving coil before the time derivative of the current reverses sign in the driving circuit (at a quarter period) but after significant energy has been transferred from the driving coil to the current sheet.

3.3 Experimental Results

In this section we present plots, shown in Fig. 13, of the measured mutual inductance between the driving coils and current sheet replicas for different geometries. The mutual inductances are normalized to their value at the smallest separation distance between the driving coil and the current sheet replica.

A function of the form

$$M^* = \frac{l}{Az + Bl} \quad (3)$$

was found to provide a good fit to the data where different values of A and B correspond to different geometries, M^* is the non-dimensional mutual inductance (normalized to the initial value), l is the length, and z is the axial displacement of the current sheet away from the driving coil. This fit, which has an R^2 value of greater than 99.90% for all data, is shown as lines in Fig. 13. Values for A and B for the different geometries are given in Table 1.

Table 1: Fit Coefficients to the Experimental Data for the Various Geometries Studied

l (cm)	α (degrees)	A	B
5 cm	10°	6.7	0.52
5 cm	20°	8.3	0.69
5 cm	30°	9.8	0.54
10 cm	10°	7.7	0.75
10 cm	20°	8.9	0.80
10 cm	30°	7.4	0.72

It can be seen from these plots that for all three half-cone angles, the mutual inductance decreases more rapidly for shorter cone lengths. In addition, the difference between the curves for the two lengths increases, on average, as the half-cone angle increases. For 10°, the average difference in normalized mutual inductance is 0.07 ± 0.007 , for 20° it is 0.09 ± 0.009 and for 30° it is 0.16 ± 0.015 . When the data for $M(z)$ are plotted for all half-cone angles for a given length on the same plot, we see that there is no noticeable difference, within the error bars, between the $M(z)$ dependences for the three half-cone angles with longer coils (right panel of Fig. 13, but such a difference is noticeable for the shorter coils (left panel of the same figure) where $M(z)$ appears to drop off more rapidly with z for higher cone angles. However, results of a Student t-test performed on the coefficients of the fit indicate that any variation between them cannot be statistically discriminated from the noise associated with the measurements with a certainty greater than 90%. Therefore, we restrict our conclusions on the effect of half-cone angle on $M(z)$ to the relative difference in $M(z)$ for the two cone lengths as mentioned above.

In order to understand the effects of inductive coil geometry on the final current sheet velocity, the data fits for the experimentally-measured $M(z)$ relations are used as the mutual inductance input to the analytical model of inductive current sheet acceleration described in the next section.

3.4 Model

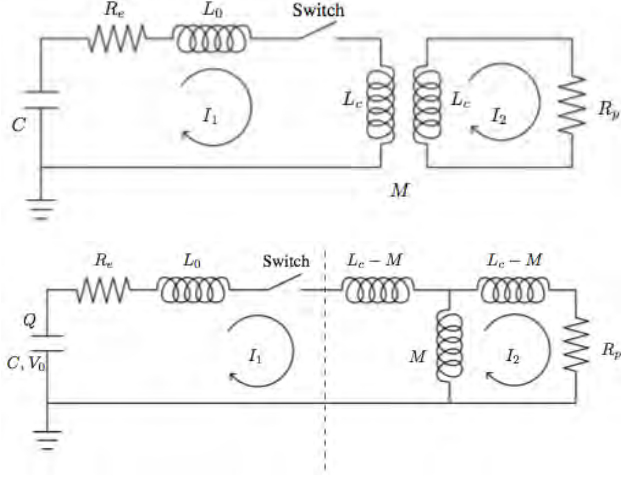


Figure 14: Lumped circuit diagrams representing the driving circuit coupled to the plasma.

The model discussed in this section has been described[7, 14, 13] in detail and used to model the two predecessors to this thruster. It is a circuit analog model of pulsed inductive acceleration. In this paper we use the model to link the experimental data of mutual inductance as a function of driving coil-current sheet separation distance to thruster performance, defined here as final current sheet velocity, in order to be able to arrive at conclusions about the effects of geometry on current sheet acceleration.

The driving circuit, inductive coil, and current sheet can be modeled as two coupled lumped-element circuits (shown in Fig. 14), with the inductive coil and current sheet acting as a transformer.

3.4.1 Governing Equations

The following equations can be written from these circuits:

$$\frac{dI_1}{dt} = \frac{\frac{L_C}{V} - L_C R_e I_1 - M R_p I_2 + (L_C I_2 + M I_1) \frac{dM}{dt}}{L_C (L_0 + L_C) - M^2} \quad (4)$$

$$\frac{dI_2}{dt} = \frac{M \frac{dI_1}{dt} + I_1 \frac{dM}{dt} - R_p I_2}{L_C} \quad (5)$$

$$\frac{dV}{dt} = -I_1/C \quad (6)$$

where I_1 is the current flowing in the driving circuit, I_2 is the current flowing in the plasma current sheet, C is the capacitance of the capacitor, M is the mutual inductance between the driving coil and the current sheet, L_0 is the initial inductance in the driving circuit, L_C is the coil inductance, R_p is the resistance of the plasma, and V is the voltage on the capacitor.

With the use of the circuit diagrams, the coil inductance can be written as:

$$L_{term} = L_C - \frac{M^2}{L_C}. \quad (7)$$

It can be seen from this equation that the coil inductance changes as a function of time due to the time changing mutual inductance, which changes due to the time changing nature of the position of the current sheet. An expression for the mutual inductance as a function of current sheet axial position has been empirically determined for a half-cone angle of 90° [14, 13] (i.e. flat coil):

$$L_{tot}(z) = L_0 + L_C (1 - \exp(-z/z_0)) = L_0 + L_{term} \quad (8)$$

where z is the axial displacement of the current sheet from the driving coil, and z_0 is the decoupling distance. This expression is set equal to the previous expression for total inductance, and solved to produce an equation for the mutual inductance that is a function of driving coil and current sheet separation distance and of which the time derivative can easily be taken:

$$M = L_C \exp(-z/2z_0) \quad (9)$$

This empirical relation, derived for a half-cone angle of 90° , is replaced by Eq. 3 in order to use the model presented here to predict how the geometries from the experiment described above will affect current sheet dynamics.

The equation of motion for the current sheet can be written taking into account the force acting on the current sheet due to the magnetic pressure between the driving coil and the current sheet as well as the accumulation of propellant mass according to a snowplough model.

$$\frac{dv_z}{dt} = \frac{1}{m(z)} \left[\frac{L_0 I_1^2}{2z_0} \exp\left(-\frac{z}{z_0}\right) - \rho_A(z) v_z^2 \right] \quad (10)$$

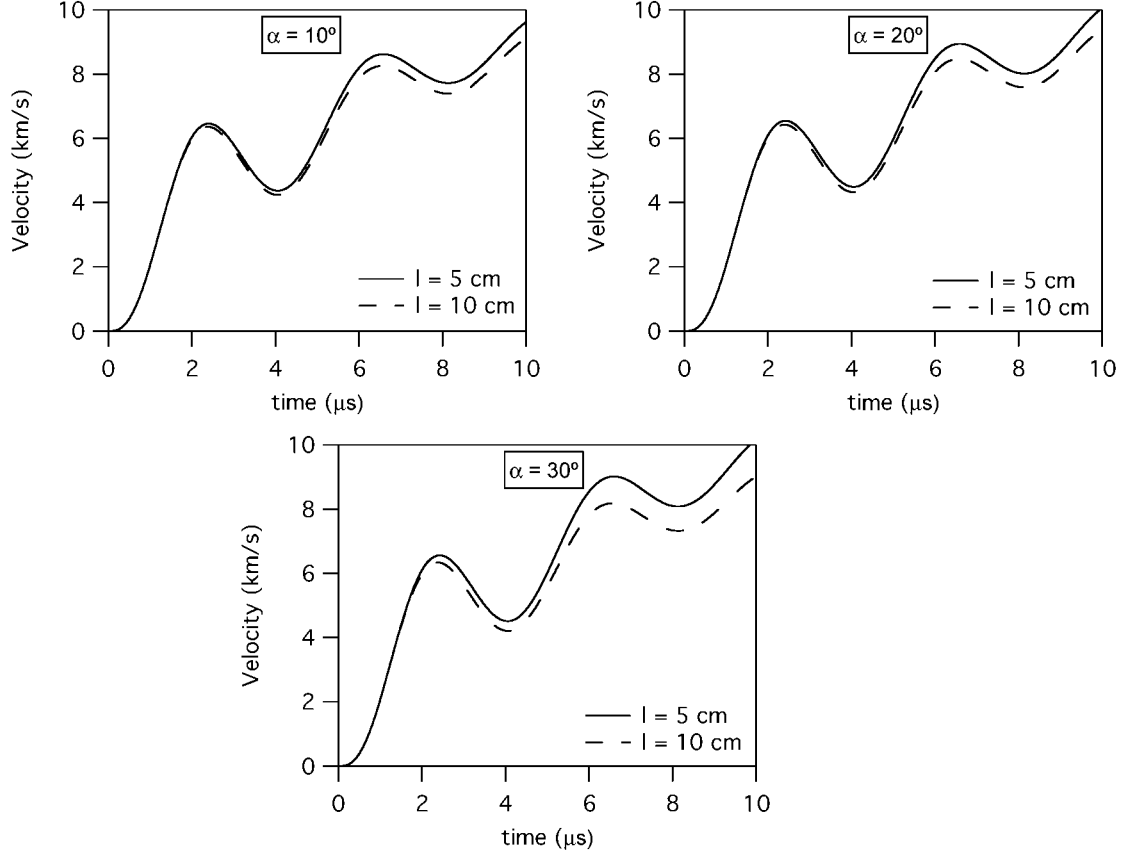


Figure 15: Results from the model for the six different geometries studied.

where ρ_A is the linear mass density distribution and v_z is the axial current sheet velocity. A simple velocity definition closes this set:

$$\frac{dz}{dt} = v_z \quad (11)$$

For this study, the pressure was modeled as a constant backfill at a value that is within the range of efficient operation as described in a previous study of the effect of pressure and pulse energy on current sheet formation [15]. The coil inductance was varied over an order of magnitude (from $\mathcal{O} \sim 100$ nH to $\mathcal{O} \sim 1000$ nH) with no noticeable change in the resulting trend in mutual inductance, current sheet velocity or position.

3.4.2 Solutions

In this section we present in Fig. 15 solutions of the model described in the previous section. These results correspond to the six different geometries studied, where Eq. 9 was replaced by Eq. 3 with the corresponding coefficients for the particular geometry.

These plots show that, for the parameter space studied, the thruster can accelerate the current sheet to a higher velocity for geometries that cause the mutual inductance to drop most rapidly as a function of the current sheet's axial displacement from the driving coil. The results also show that the difference in final velocity for the two different lengths is greater for larger cone angles than for smaller ones. This is consistent with the trends in $M(z)$ seen in the experimental data.

3.5 Discussion

Combining the results of the experiments and the results of the model we conclude that shorter inductive coils will cause the mutual inductance to decrease faster as a function of driving coil and current sheet separation, and will in turn accelerate the current sheet to a higher velocity within the same period of time.

An explanation for the more gradual decrease in mutual inductance as the current sheet moves axially away from the driving coil can be seen by referring to the simulated magnetic field patterns associated with the two different coil lengths (shown in Fig. 16) for a driving current amplitude of 20,000 Amps. These simulations were obtained using the program Maxwell SV by Ansoft to simulate a current flowing through a conical conductor made of copper having the same geometry as the inductive coils studied here.

If we assume that magnetic flux is conserved through the interior of the driving coil, then the field for longer coils will be more solenoidal, or constant, within the volume of the coil, and transitions to a $B \sim 1/z^3$ dependency will occur at larger values of z . This is consistent with a more-quickly decreasing flux within the current sheet due to the driving coil as the current sheet progresses axially away from the driving coil.

The effect of half-cone angle on the results of the model are limited to causing a greater disparity in velocity for different cone lengths as the half-cone angle is increased. The fact that the length has a greater effect on $M(z)$ can be explained by comparing how the magnetic field profile within the

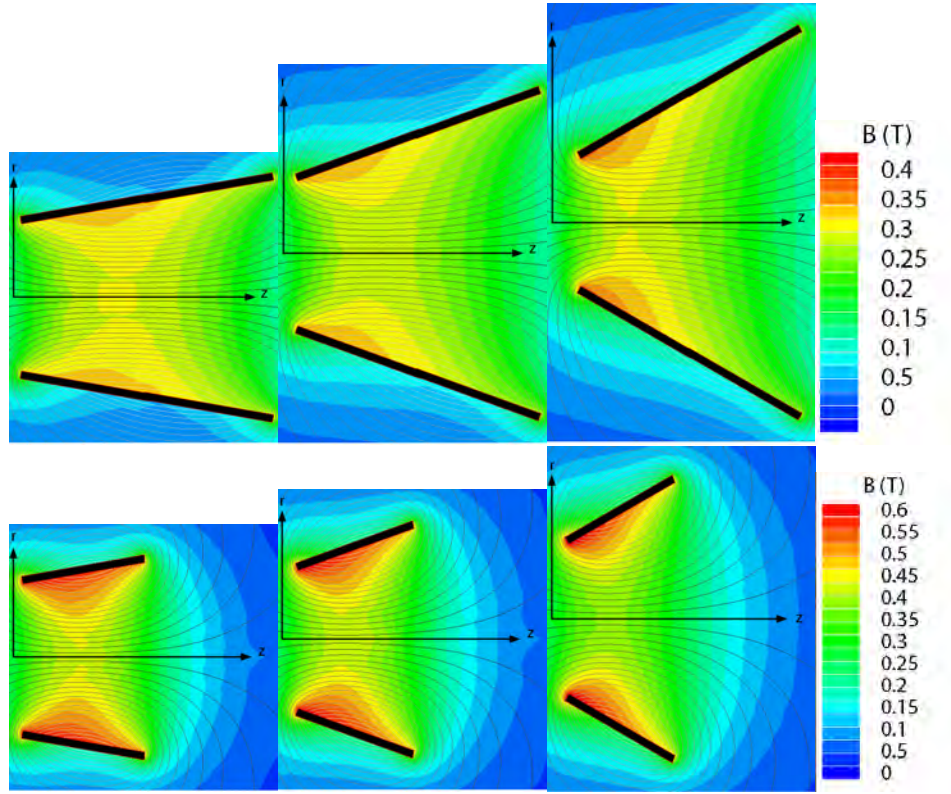


Figure 16: Simulations of the magnetic field (performed in Ansoft Maxwell SV) (left to right) 10°, 20°, and 30° half-cone angle, for Top Row: a length of 10 cm and Bottom Row: a length of 5 cm.

volume of the cone changes with cone angle and how the profile changes with length. In Fig. 16, the magnetic field changes more dramatically between shorter and longer coils than for coils of differing half-cone angle. It should be noted that the field profile does change with cone angle, but over the parameter space studied here, the effect is too small to be observed in our experiment.

3.6 Conclusions

Experimentally determined relations for the mutual inductance between driving coils of varying geometries and associated current sheet analogs reveal that the length of the driving coil affects the dependence between mutual

inductance and axial separation distance between the two coils. Longer coils will cause the mutual inductance to drop off less rapidly with separation distance, which can be understood considering the magnetic field patterns associated with these two geometries. For longer coils, the more-uniform section of the field will be extended through the interior of the coil, and the gradient in magnetic field strength within the volume of a current sheet translating axially away from the driving coil will be reduced over that of a shorter driving coil. As the half-cone angle is increased, the disparity in the magnetic field profile within the volume of the current sheet for differing lengths is greater, causing the difference in $M(z)$ for the two cone lengths to be larger for larger half-cone angles, but conclusions on the influence of half-cone angle on $M(z)$ are limited to this relative effect as half-cone angle has a less dramatic impact on the magnetic field profile than coil length.

We conclude that, within the parameter space investigated and the assumptions of the model, shorter driving coils, and to a lesser extent larger half-cone angles (whose effects are less pronounced for longer coils), are more favorable for higher current sheet acceleration.

Both the experiment and the model do not take into account the radial compression of the current sheet that occurs due to the pinching effect of a real thruster. The extent to which that pinching may alter the above conclusions should be the subject of a future investigation.

References

- [1] R. H. Lovberg C. L. Dailey. The PIT MkV pulsed inductive thruster. Technical report, Lewis Research Center, 1993.
- [2] E. Y. Choueiri and K. A. Polzin. Faraday acceleration with radio-frequency assisted discharge. *Journal of Propulsion and Power*, 22(4):701–710, 2006.
- [3] T.E. Markusic and J. W. Berkery E. Y. Choueiri. Visualization of current sheet evolution in a pulsed plasma accelerator. *IEEE Transactions of Plasma Science*, 33(2):528–529, April 2005.
- [4] C. Chang, K. Leou, and C. Lin. Real-time control of ion density and ion energy in chlorine inductively coupled plasma etch processing. *Journal of vacuum Science and Technology*, 21(4):1183–1187, July 2003.

- [5] R.G. Jahn. Physics of Electric Propulsion. McGraw-Hill Book Company, 1968.
- [6] R.H. Lovberg C.L.Dailey. Large diameter inductive plasma thrusters. Number AIAA 79-2093, oct 1979.
- [7] K. A. Polzin and E. Y. Choueiri. Performance optimization criteria for pulsed inductive plasma acceleration. IEEE Transactions on Plasma Science, 34(3):945–953, 2006.
- [8] R. G. Jahn. Physics of Electric Propulsion. McGraw-Hill Book Company, 1968.
- [9] E. Y. Choueiri and K. A. Polzin. Faraday acceleration with radio-frequency assisted discharge. Journal of Propulsion and Power, 22(3):611–619, May-June 2006.
- [10] C.L. Dailey and R.H. Lovberg. Current sheet structure in an inductive-impulsive plasma accelerator. AIAA Journal, 10(2):125–192, Feb. 1972.
- [11] R.H.Lovberg C.L.Dailey. Pit mark v design. Number AIAA 91-3571, 1991.
- [12] A. K. Hallock and E. Y. Choueiri. Current Sheet Formation in a Conical Theta Pinch Faraday Accelerator with Radio-frequency Assisted Discharge. Number IEPC-2007-165, September 2007.
- [13] R.H. Lovberg and C.L. Dailey. A PIT primer. Technical Report 005, RLD Associates, Encino, CA, 1994.
- [14] C.L. Dailey and R.H. Lovberg. The PIT MkV Pulsed Inductive Thruster. Technical Report 191155, Lewis Research Center, Redondo Beach, CA, July 1993.
- [15] Hallock, A. K. Choueiri, E. Y. and Polzin, K. A. . Current sheet formation in a conical theta pinch faraday accelerator with radio frequency assisted discharge. Number AIAA-2008-5201, July 2008.